ChemComm

FEATURE ARTICLE

View Article Online
View Journal | View Issue

Cite this: *Chem. Commun.*, 2016, 52, 8972

Modelling spin Hamiltonian parameters of molecular nanomagnets

Tulika Gupta and Gopalan Rajaraman*

Received 9th February 2016,
Accepted 16th June 2016

DOI: 10.1039/c6cc01251e

www.rsc.org/chemcomm

Molecular nanomagnets encompass a wide range of coordination complexes possessing several potential applications. A formidable challenge in realizing these potential applications lies in controlling the magnetic properties of these clusters. Microscopic spin Hamiltonian (SH) parameters describe the magnetic properties of these clusters, and viable ways to control these SH parameters are highly desirable. Computational tools play a proactive role in this area, where SH parameters such as isotropic exchange interaction (J), anisotropic exchange interaction (J_x, J_y, J_z), double exchange interaction (B), zero-field splitting parameters (D, E) and $\boldsymbol{g}$-tensors can be computed reliably using X-ray structures. In this feature article, we have attempted to provide a holistic view of the modelling of these SH parameters of molecular magnets. The determination of J includes various class of molecules, from di- and polynuclear Mn complexes to the {3d-Gd}, {Gd–Gd} and {Gd-2p} class of complexes. The estimation of anisotropic exchange coupling includes the exchange between an isotropic metal ion and an orbitally degenerate 3d/4d/5d metal ion. The double-exchange section contains some illustrative examples of mixed valance systems, and the section on the estimation of zfs parameters covers some mononuclear transition metal complexes possessing very large axial zfs parameters. The section on the computation of $\boldsymbol{g}$-anisotropy exclusively covers studies on mononuclear Dy^{III} and Er^{III} single-ion magnets. The examples depicted in this article clearly illustrate that computational tools not only aid in interpreting and rationalizing the observed magnetic properties but possess the potential to predict new generation MNMs.

1. Introduction

Molecular nanomagnets (MNMs)[1] have intrigued scientists from various research fields, including physicists, chemists and theoreticians, for more than two decades.[2] This is essentially due to the fact that these molecules possess several potential applications.[1^5] In addition to these technological applications, MNMs also exhibit interesting physics, such as quantum tunnelling of magnetization (QTM), quantum phase interference (QPI), *etc.*[1c,3] The term MNMs covers a wide range of molecules exhibiting interesting magnetic behaviours, such as monometallic complexes exhibiting single ion magnetic behaviour (SIMs),[4] multinuclear clusters exhibiting single molecule magnet behaviour (SMMs),[1a,5] one-dimensional coordination polymers exhibiting single chain magnets (SCMs),[6] and molecular wheels[7] showcasing QPI phenomena. MNMs straddle the interface between the classical and quantum mechanical worlds. SMMs/SIMs show magnetic bistability,[8] which allows their magnetic moments to be positive or negative[9] and ensures their stability for prolonged periods of time in a zero external magnetic field. This leads to their potential applications in high-density magnetic storage devices, q-bits, molecule spintronics, molecular refrigeration and quantum computing devices. This is essentially due to their intrinsic magnetic properties, *i.e.* large spin ground state (S) and negative magneto-crystalline anisotropy (zero-field splitting parameter; D) leading to spin-reversal barrier height (U_{eff}) for reorientation as well as slow relaxation of magnetization. However, the distinctive properties of SMMs are detected only at liquid helium temperatures. In order to employ SMMs in information storage devices, the operating magnetic blocking temperature (T_B), at which hysteresis is observed, must be significantly enhanced. However, such excessive conditions are not required for some applications, such as quantum computing.[209b]

Apart from the S and D parameters, the magnetic exchange interaction (J)[5a,10,212] is found to be an essential ingredient in the synthesis of SMMs, as weak exchange results in the suppression of SMM characteristics by expediting magnetic relaxation *via* close-lying excited states. Additionally, the sign of the exchange interaction essentially controls the value of the spin ground state S and, thus, is a key component in controlling SMM characteristics. Beyond SMMs, the exchange interaction also plays a pivotal role in controlling the change in magnetic entropy (ΔS_m) and the corresponding magnetocaloric effect values. This underlines the importance of understanding the mechanism of coupling for future success in the area of

Department of Chemistry, IIT Powai, Mumbai-400076, India.
E-mail: rajaraman@chem.iitb.ac.in

molecular refrigeration. However, extracting quantitative data pertaining to such large, low symmetry cluster complexes often remains a challenge. Hence, meticulous analysis of the type of bridging ligand as well as several structural parameters, such as the metal–metal distances, the bond angles between the two metal ions through the bridging ligand, the dihedral angle formed between the coordination planes possessing metal ions, and the metal ion stereochemistries, must be analysed in detail to ascertain the factors dictating the exchange parameters.

In order to obtain large U_{eff} and T_{B} in SMMs, a large magnetic moment and high Ising magnetic anisotropy (large negative zero-field splitting; D)[11] are required. These parameters stabilize energy levels with large z-components of the magnetic moment. The D parameter is particularly associated with spin–orbit coupling (SOC), spin–spin coupling (SSC) and structural distortion[12] observed in the coordination sphere (such as Jahn–Teller distortion, J–T). If these parameters are controlled, one can achieve a desirably large negative D value. The alignment of the magnetic axis pertinent to the single-ion zfs interaction represents the location of the ligand atoms. Hence, the co-ordination number, symmetry, geometry, position of the ligands, metal–ligand bond direction, distortion around the metal ion coordination, nature of the ligand donor strength, and covalency of the in-plane and axial metal–ligand interactions can aid in fine tuning the magnitude, sign and direction of the zfs parameters. Detailed analysis of the zfs parameters and their variation with changing geometry as well as their electronic structure are of key interest in the design of novel SMMs. Recent studies have proved that a larger spin does not proportionally increase U_{eff} and T_{B}.[209a] Theoretical calculations suggest that $U_{\text{eff}} = DS^2$ is independent of S as D is proportional to $1/S^2$.[5b] This invokes D to be a more influential parameter than S in enhancing U_{eff} and T_{B}.

The unpaired electrons in lanthanide[13] ions are deeply buried and do not significantly interact with the ligand donor atoms. This preserves the degeneracy and confers significant magnetic anisotropy on these ions. The lanthanide ions inherit large spin–orbit (SO) coupling and a large unquenched orbital angular moment. Due to this large SO coupling, the ground spin–orbital manifolds of lanthanides are described using the combined spin and orbital quantum number M_J (microstates due to crystal field splitting). The quantum number M_J in fact plays the role of the spin ground state S in lanthanide chemistry, while the crystal field splitting (CFS) of the M_J levels can be compared to the axial zero-field splitting parameter in transition metal clusters. This entails the use of lanthanides in molecular magnetism,[14] as the size of the ground state can be fixed to the $(2M_J + 1)$ term {multiplicity of the ground M_J level}; by fabricating the CFS around the metal ion, we can obtain very large magnetic anisotropy for reorientation of the magnetization. The pitfall in lanthanide chemistry is the significant quantum tunnelling of magnetization between the M_J levels and the weak exchange interactions observed on polynuclear complexes. These factors pave the way for relaxation at lower temperatures. The gyromagnetic (Lande factor, g) tensor of lanthanides and the CFS parameters offer insight into the origin of magnetization relaxation. Notably, QTM is directly proportional to the intrinsic tunnel splitting (Δ_{tun}) present in the absence of any magnetic field. A highly symmetric environment facilitates a smaller Δ_{tun} value and improved SMM characteristics. In this context, the highly symmetric environment around the lanthanide ions offers strong axiality (large g_z or $g_{\parallel}$), while the lower symmetry induces transverse components (large g_x/g_y or $g_{\perp}$) and QTM behaviour. Hence, meticulous analysis of the $\boldsymbol{g}$-tensors is extremely crucial for controlling the QTM and CFS parameters.

Tulika Gupta

Tulika Gupta was born in Titagarh (Kolkata), India and received a BSc in Chemistry from Jadavpur University, Kolkata in 2009. She obtained her MSc from IIT Guwahati in 2011 and received UGC-NET and GATE scholarships to undertake a PhD under the supervision of Prof. Gopalan Rajaraman at IIT Bombay, India. Her research interests focus on the modelling of molecular nanomagnets, with special emphasis on computing the magnetic anisotropy of lanthanide systems and estimating the zero-field splitting parameters of transition metal complexes using DFT and state-of-the-art ab initio calculations.

Gopalan Rajaraman

Gopalan Rajaraman (born in Thanjavur, India) received his PhD at the University of Manchester, UK under the supervision of Prof. R. E. P. Winpenny and Dr E. J. L. McInnes in 2004. He then undertook postdoctoral stays at the University of Heidelberg, Germany (2005–2007) in the group of Prof. P. Comba and the University of Florence, Italy in the group of Prof. D. Gatteschi (2007–2009). In December 2009, he joined IIT Bombay, India as an assistant professor and became an associate professor in 2014. His research focuses on employing electronic structure methods to understand the structure, properties and reactivity of molecules possessing unpaired electrons (open-shell systems). In addition to modelling molecular magnets, his group also actively pursue research in the area of modelling bio-mimic reactions catalysed by high-valent metal-oxo/imido complexes.

It is worth noting that the crystal field environment, coordination number, and local point group symmetry (prolate/oblate shape of the electron cloud) must be manipulated simultaneously to achieve larger U_{eff}/T_B values.

Thus, the synthesis of new generation MNMs requires a thorough understanding and control of the microscopic spin Hamiltonian[16] parameters, such as J, D, E, and g. Experimentally, numerous characterization techniques, such as magnetic susceptibility measurements, EPR, NMR and inelastic neutron scattering (INS) techniques, are employed to extract these parameters. However, these techniques have their own limitations; for example, (i) extracting the multiple J values present in a polynuclear cluster is extremely challenging, (ii) extracting the sign and magnitude of D values exceeding ~ 20 cm^{-1} requires facilities which are scarce, (iii) extracting the g-tensors and CFS parameters of lanthanides is also an exigent task. In this regard, computational tools are indispensable; due to tremendous developments in computing hardware, DFT[17,18] and *ab initio*[19] calculations can now be performed even for very large molecules. Extensive efforts been undertaken to compute various spin Hamiltonian parameters of molecular magnets, and these data not only offer rationalizations for experimental observations but have also often been used to predict these properties for *in silico* designed molecules. In this feature article, we aim to review recent developments in the computation of various spin Hamiltonian parameters of MNMs.

2. Relevant spin Hamiltonian parameters

Model Hamiltonians are used to depict results in the research of molecular magnets by theoreticians, experimental physicists or chemists. This enables discussion of numerous parameters derived from experiments and first-principle calculations employing these models. Hence, it is necessary to construct the quantum mechanical Hamiltonian which denotes the energy spectrum of the system. Furthermore, the representation of results through these models allows us to validate theoretically predicted results through modeling of experimental observations. A model spin Hamiltonian always considers model parameters by neglecting chemical bonding and averaging out the possible interactions. The parameters should be selected carefully, as they dictate the accuracy of the quantitative predictions. Spin angular momentum operators and their interactions with each other and with an external magnetic field are taken into account during the construction of the spin Hamiltonian. The spin Hamiltonian depends on the spin contributions and spin properties of the system and enumerates the orbital momentum contributions required to define the system.

Accounting for the exchange coupling and magnetic anisotropy, the Heisenberg Hamiltonian model can be represented as:

$$\hat{H} = \mu_B \sum_i \hat{S}_i \cdot g_i \cdot \hat{B} - \sum_{ij} J_{ij} \cdot \hat{S}_i \cdot \hat{S}_j + \sum_i \hat{S}_i \cdot D_i \cdot \hat{S}_i \quad (1)$$

In the above equation, the first term corresponds to the Zeeman interaction, which increases the degeneracy of the $|\pm m_s\rangle$ state in the presence of an external magnetic field $\hat{B}$; μ_B is the Bohr magneton, while g represents the Lande gyromagnetic tensor. The second term implies isotropic exchange interaction (J) between the spin vectors, where the summation indicating each pair of spins (S_i, S_j) has been counted only once. Considering the relative orientation of both the spins, the interaction can be considered as isotropic. The second term forms the spin energy spectrum but does not contribute to the magnetic anisotropy. The third term in the above equation represents the zero-field splitting parameter (D tensor).

3. Modelling spin Hamiltonian parameters

3.1 Magnetic exchange interaction (J)

Experimentally, the magnetic exchange interaction J is evaluated by fitting the temperature dependent magnetic susceptibility data.[20] For dinuclear complexes, extracting the J values is rather straightforward; however, for polynuclear complexes with multiple J values, two issues mainly arise: (i) employing several J values for polynuclear complexes is likely to lead to over-parameterization in the fitting procedure, where featureless susceptibility data are often employed to fit a number of variables. At the same time, if fewer than the minimum required number of parameters are employed, this can lead to an over-simplified Hamiltonian (note that next-nearest-neighbour interactions are often ignored, and similar J parameters for interactions not equivalent by symmetry are assumed). (ii) For very large molecules possessing large numbers of unpaired electrons, a problem arises during diagonalization of the Hamiltonian that is directly proportional to the number of spins and magnitude of the ground state S. To circumvent this issue, approximate methods such as classical/quantum Monte-Carlo methods are employed, and a fitting procedure employing the Lancoz algorithm[21] has been now developed for relatively large systems. Both these methods often require a good starting point to simulate the magnetic data.

In this regard, DFT calculations[18] have emerged as a powerful tool; if a suitable exchange–correlation functional and basis set are employed, a good numerical estimate of exchange coupling constants can be obtained, even for a very large cluster possessing several J values. In addition to computing the Js, calculations also offer insights into the sign and nature of J values. As the J values in this case are derived directly from the X-ray structure, these calculations do not have over-parameterization problems and offer guidance for fitting the experimental data with the right set of parameters. For the estimation of magnetic coupling using the Hartree–Fock or DFT methods, the broken symmetry (BS) model developed by Noodleman has been employed.[22] There are essentially three equations available to compute the J values:

$$J = \frac{(E_{BS} - E_{HS})}{2S_1S_2 + S_2} \quad (2)$$

$$J = \frac{2(E_{BS} - E_{HS})}{S_{HS}(S_{HS} + 1)} \quad (3)$$

$$J = \frac{(E_{BS} - E_{HS})}{\langle S^2\rangle_{HS} - \langle S^2\rangle_{BS}} \quad (4)$$

Eqn (2) is proposed by Noodleman *et al.*, while Ruiz *et al.*[23] proposed eqn (3) and Yamaguchi *et al.*[24] proposed an equation based on spin projection (eqn (4)). An extension to polynuclear transition metal complexes was made by introducing the pairwise interaction model. It has been proposed that[191] to calculate exchange coupling constants in a polynuclear complex with '*n*' different *J* values, one should estimate energies of '*n* + 1' single determinants corresponding to different spin distributions. These energies are related to the Eigenvalues of the Ising Hamiltonian and can thus be used to obtain a system of '*n*' equations with '*n*' unknowns. However, it has often been stressed that more than '*n* + 1' solutions must be determined to estimate the possible errors in the *J* values.[10]

It should be noted here that although eqn (2) and (3) yield strikingly different *J* values for systems such as dinuclear Cu^{II} complexes, the differences are particularly small when the *S* values of the interacting pairs are larger. Although for dinuclear complexes, all three equations are employed by different groups to compute *J* values, the majority of polynuclear examples studied employ the Ruiz equation to extract the *J* values. Using this methodology, more than 100 polynuclear clusters have been studied;[18,25] often, the calculated magnetic susceptibilities are in good agreement with experiments. Over the past decade, numerous papers have been published regarding the computational implication of isotropic exchange interactions in transition metal clusters. As we intend to provide an overview of the estimation of various spin Hamiltonian parameters in the area of MNMs using computational techniques, we have limited the examples in transition metal clusters to Mn based clusters studied by us and others in recent years. Other examples covered include di- and polynuclear {3d-Gd}, {Gd–Gd} and {Gd-2p} systems.[26] This study will also be restricted only to molecules and will not cover molecules adsorbed on the surface.[27] All the *J* values mentioned here are according to $-JS_1S_2$ formalism.

3.1.1 Regulating isotropic *J* for Mn-based dinuclear complexes. Mn-based[28] clusters have been of great interest to the molecular magnetism community for a long time. This is primarily due to the fact that Mn^{III} complexes often yield negative zero-field splitting parameters, a key ingredient in the construction of SMMs. Although the magnitudes of the *D* values are comparatively smaller for Mn^{III} ions (in the range of ± 4 cm^{-1}),[192] the sign is predictable (<0 cm^{-1} for elongated octahedral complexes); thus, Mn is a popular choice for synthetic chemists. The negative *D* values of Mn^{III} ions are associated with the inherent Jahn–Teller distortions; however, this distortion not only controls the single-ion and cluster anisotropy but also the intramolecular magnetic exchange interactions. In reference to this, we have probed three different types of bis-μ-alkoxo bridged Mn^{III} dimeric complexes $[Mn_2^{III}(\mu\text{-OR})_2(biphen)_2(ROH)_x(L)_y]$ (**1**) [R = Me, Et; H_2biphen = 2,2′-biphenol and L = terminally bonded N-donor ligand; *x*, *y* can vary in the numerical range of 2 to 4] (see Fig. 1) in collaboration with Jones and co-workers.[29] The complexes have been categorized based on the relative orientation of their

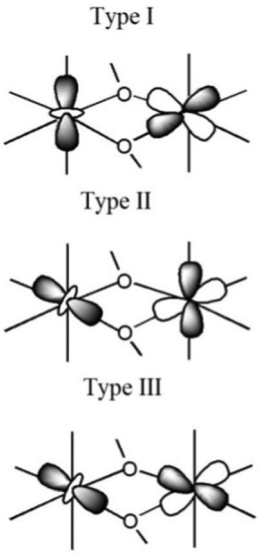

Fig. 1 Illustration of three types of magnetic spatial orientations in bis-μ-OR bridged Mn^{III} dimers. Reprinted with permission from ref. 29. Copyright 2012 Wiley-VCH.

associated J–T axes with respect to one another and their orientations with respect to the bridging ligand plane. Compared to structural parameters such as Mn–O bond distances or Mn–O–Mn bond angles, the dihedral plane between the two J–T axes has been proven to be the dictating factor for the different magnetic behaviours in the three types of complexes. The J–T axes in type I structures are parallel to each other but perpendicular to the bridging plane, while those in type II structures are parallel to each other as well to the bridging plane. Notably, these axes are perpendicular to each other in type III structures. DFT calculations (B3LYP/TZV setup) reproduce both the sign and magnitude of the *J* values across the series studied. Type I structures show moderately strong antiferromagnetic exchange, type II structures show weak ferro- and antiferromagnetic exchanges and type III structures are found to show moderately strong ferromagnetic exchange. Although the test set contains only 45 examples, the orientation seems to predict the nature as well as the magnitude of the *J* values ranging from -31.0 cm^{-1} to $+39.4$ cm^{-1} (see Fig. 2a). The observed values are rationalized based on MO analysis, where in type III dimers, due to the perpendicular orientation of the J–T distortions, significant orbital overlaps are avoided and the cross-interaction between the empty and single-occupied orbitals is enhanced, leading to strong ferromagnetic coupling (see Fig. 2b). Although this study offers a method to obtain ferromagnetic coupling in $\{Mn_2^{III}(OR)_2\}$ dimers, the perpendicular orientation of the J–T axis diminishes the magnetic anisotropy; this suggests that large positive *J* and *D* values are unlikely to co-exist in $\{Mn_2^{III}(OR)_2\}$ dimers.[29]

Although the established concept was for $\{Mn_2^{III}(OR)_2\}$ type dimers, the classification was also found to have relevance in other classes of dimers. By studying a series of phenolic oxime bridged Mn^{III} dimers $[Mn_2^{III}O(Me\text{-}Sao)(tpa)_2]^{2+}$ {Sao = salicylaldoxime, tpa = tris(2-pyridyl-methyl)amine} (**2**), the relevance of the J–T axis orientation in controlling the *J* values was established.[30]

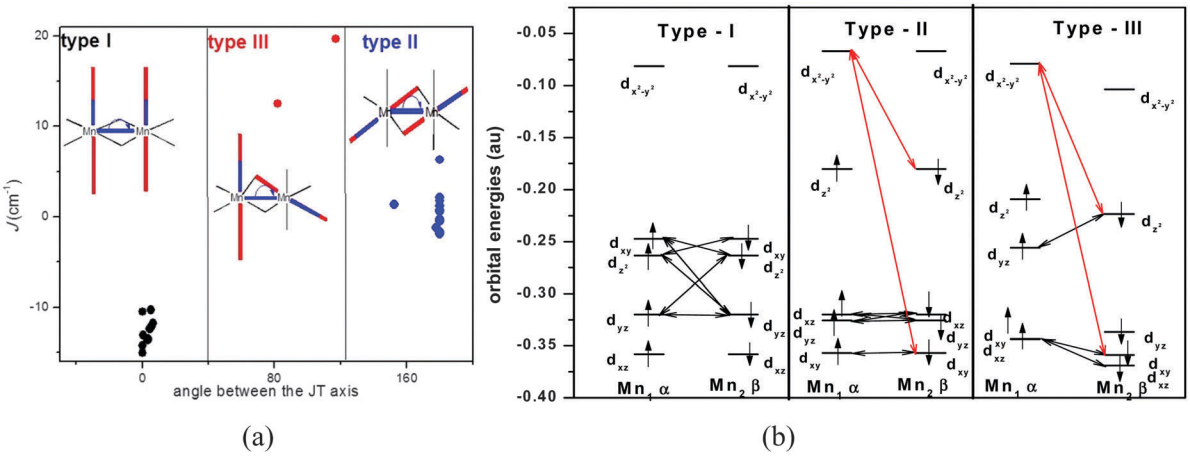

Fig. 2 (a) Plot of J (cm^{-1}) *vs.* the angle forged between the two J–T axes in Mn dimers of types I–III. (b) Computed significant magnetic exchange interactions between the magnetic orbitals in type I–III structures. Anti-ferromagnetic interactions are shown with black lines, while ferromagnetic interactions are denoted by red arrows. Reprinted with permission from ref. 29. Copyright 2012 Wiley-VCH (please note that the values given in the above figure correspond to $-2JS_1S_2$ formalism, while all the values in the text are pertinent to $-JS_1S_2$ formalism).

The complexes studied are categorized as type-I (see Fig. 3a) and possess strong antiferromagnetic interactions, as expected. Although the sign can be predicted, to rationalize the variation in the magnitude of the *J*s, one often must invoke variation in the structural parameters. Herein, the magneto-structural correlation developed for the Mn–N–O–Mn dihedral angle is found to play a decisive role in dictating the strength of the J values (the J_{AF} contribution decreases with increasing dihedral angle). When the structures are further altered, such as for $[Mn^{III}_2O(Me\text{-}Sao)_2(dpa)_2]^{2+}$ {dpa = di(2-pyridyl-methyl)amine} (**3**) complexes possessing two oxime (–N–O) bridged Mn^{III} dimers (see Fig. 3b), the sign can still be predicted (type I complexes); however, the magnitude varies as the dihedral angle is altered significantly.[31]

If we examine other accessible oxidation states of Mn ions, various other structural parameters are found to control the sign and strength of the J values. By studying the $[Mn_2O_2(NH_3)_8]^{n+}$ [32] (**4**) complex with varying '*n*' values, several important conclusions regarding the factors controlling the sign and strength of J values in mixed valance complexes are derived. Calculations reveal a strong dependency of *J*s on the Mn–Mn distance, where shorter distances (<2.3 Å) were found to yield very strong antiferromagnetic coupling (a situation resembling a tri-μ-oxo bridged system to obtain such short Mn–Mn distances), while a large (>3 Å) distance results in weak antiferro/ferromagnetic exchanges (see Fig. 3c).[32] Calculations on the same model with Mn oxidation states of +3/+4 yielded remarkably different J values, implying the dependence of the oxidation state on the estimation of the J values in the $[Mn_2O_2]$ core.[32] Additionally, if the bridging ligands are altered along with the oxidation states, significantly strong J values are noted. By studying a series of dinuclear Mn complexes possessing {III, III}, {III, IV} and {IV, IV} oxidation states and bridging ligands varying from μ-O to $\mu\text{-}O_2$ to additional acetates, variations in the J values are noted from +20 cm^{-1} (for the $\{Mn^{III}_2(\mu\text{-}O)(OAc)\}$ (**5**)[33] core) to −780 cm^{-1} (for the $\{Mn^{IV}_2(\mu\text{-}O)_3$ (**6**) core}).[34] Although these calculations overestimated the J values in some cases, they clearly predict a similar trend to the experimental observations and suggest a pronounced dependence of the bridging ligand on the nature of the J–T distortion for {III, III}, {III, IV} and {IV, IV} type complexes of Mn ion. Additionally, the calculations predicted the charge transfer abilities of the ligand donors as: peroxo ≥ oxo ≫ TACN (triazacyclononane) > acetate.[34,35] Moreover, analysis of the mechanism of exchange showed the prevalence of super-exchange *via* the μ-oxo bridges over direct Mn–Mn interactions.[36] In the $[Mn^{III}_2(\mu\text{-}O)(\mu\text{-}RCOO)_2(bipy)_2(OH)X]$ {R = acetate or phenyl acetate}

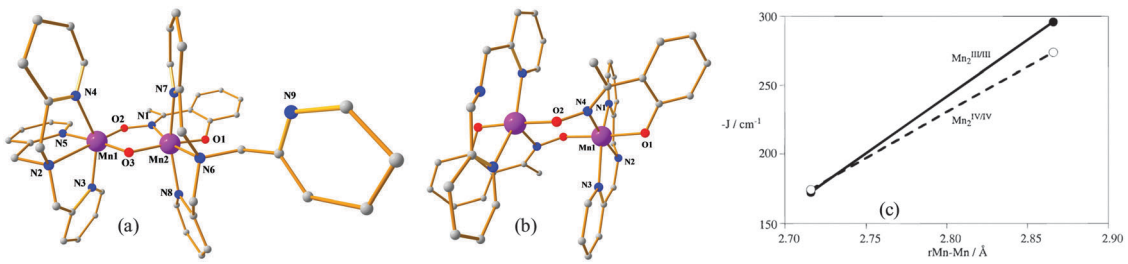

Fig. 3 Crystal structures of complexes (a) **2** and (b) **3**. These complexes show antiferromagnetic interactions of −9.8 (exp)/−12.0 (cal) cm^{-1} and −7.2 (exp)/−4.4 (cal) cm^{-1}, respectively. Note that in the abovementioned crystal structures, H-atoms have been omitted for clarity. {Color scheme: Mn^{III}: pink; N: blue; O: red; C: grey.} (c) Correlation between J for $Mn^{IV/IV}_2$ and $Mn^{III/III}_2$ complexes for the Mn_2O_2 core. Reprinted with permission from ref. 32. Copyright 1997 American Chemical Society.

(7) complex, switching of the coupling from antiferromagnetic to ferromagnetic was observed upon changing the ligand (X) from –Cl (or H_2O) {elongated Mn sites} to an azido ligand {compressed Mn sites}.[37] Weak antiferromagnetic *J*s were computed for bent Mn^{III}–O–Mn^{III} dimeric complexes. BS-DFT calculations on $[Mn^{III}_2(thme)_2(bpy)_2]^{2+}$ (**8**) showed a weak exchange between the ions.[38]

It is notable that the exchange interaction relies on an occupied orbital in a mononuclear fragment and on the overlap between the two molecular orbitals in the binuclear unit. Now, the spatial orientation of these magnetic orbitals and the resultant overlap is essentially dictated by the nature of the coordinated ligands as well as their relative positions. Based on this criterion, several reports have been published illustrating the crucial role of the bridging/twist angle and the nature of the bridging/terminal ligands attached to the metal ion.[193] This is also evident from our earlier examples (see Fig. 2), where we have explicitly shown that the relative position and occupation of the orbitals leads to variation in the *J* values. Furthermore, the different d orbital occupations in type I, II and III complexes (see Fig. 2b) are reminiscent of the classical orbital ordering concept by Khomskii,[194] which states the importance of magnetic orbitals and their ordering for magnetic exchange. Additionally, this concept inherits the essence of the GKA (Goodenough–Kanamori–Anderson)[195] rule, which dictates the nature of the exchange interactions for varying coordination environments and orbital occupations.

3.1.2 Exploring isotropic *J* in Mn polynuclear complexes. In this section, we aim to extend our understanding of the dinuclear Mn dimers to polynuclear Mn clusters and to examine whether the established mechanism of magnetic coupling also holds true for large Mn clusters. Unlike in dimers, where only one exchange interaction is present, polynuclear clusters contain several exchange constants; often, many of the parameters are same or similar. Although X-ray structures can be used as guides to determine the unique number of *J*s present in a cluster, this can sometimes be misleading, as significant variation in the structural parameters does not necessarily mean that the *J* values are drastically different. The sign and strength of the *J* values are controlled by the super-exchange mechanism; this must be understood clearly to judge the number of *J* values required. DFT calculations on $[Mn^{II}_3(Me_3CCO_2)_6(Me_3CCO_2H)_5]$ (**9**) affirm that the two-*J* model is more viable in reproducing magnetic data and suggest the use of this model for efficient calculation in trinuclear complexes.[39] Trinuclear complexes containing Mn are very common, and several Mn^{III} triangles are also reported in the literature. A fluoride bridged Mn^{III} triangle having the molecular formula $[NHEt_3]$ $[Mn_3O(bta)_6F_3]$ (**10**) (here, bta = benzotriazole, see Fig. 4a) has been studied. Two different exchange coupling values, J_a and J_b, are employed for this molecule, as the Mn–F–Mn angles are significantly different. The J–T axes have parallel orientation in this cluster, and both Mn–Mn interactions are classified as type I. Calculations yield *J* values of −6.0 and −4.2 cm^{-1}, as per expectations.[40] DFT calculations have been employed to extract *J* values in a linear {Mn^{II}–Mn^{III}–Mn^{II}} cluster $[Mn_3(HCht)_2(bpy)_4]^{3+}$ (**11**) (HCht = *cis*,*cis*-1,3,5-cyclohexanetriol; see Fig. 4b).[41] Calculations yield a *J* value of +7.0 for the Mn^{II}–Mn^{III} interactions and offer a value of +2.0 cm^{-1} for the next-nearest-neighbour Mn^{II}–Mn^{II} interactions. The calculations in this case clearly suggest that the next-nearest neighbour interactions cannot be neglected, as they can sometimes be strong enough to compete with the nearest-neighbour interactions.[41]

DFT studies performed on three pentanuclear Mn^{II} clusters, $[Mn_5(PzCAP)_6]^{4+}$, $[Mn_5(PzOAP)_6]^{4+}$ (**12**) and $[Mn_5(PyPzOAPz)_6]^{4+}$, (**13**) revealed $J = -3.0$, −3.2 and −3.0 cm^{-1}, respectively, which are in compliance with experimental values.[42] There are several theoretical studies on hexanuclear Mn clusters. Particularly, DFT calculations performed on a series of $\{Mn^{III}_2Mn^{II}_4\}$ mixed-valence clusters, $[Mn_6\{(CH_3)_3CCO_2\}_8(tmp)_2(py)_2]$ (**14**) and $[Mn_6(CH_3CO_2)_6(thme)_2(H_2tea)_2]$ (**15**) (here tmp = 1,1,1-tris-(hydroxymethyl)propane and thme = 1,1,1-tris(hydroxymethyl)-ethane) (see Fig. 5a and b), help to determine the nature of the ground state, as it could not be determined unambiguously from experimental data. Five different exchange coupling constants (see Fig. 5c) are assumed, and the computed *J* values offer an excellent fit to the susceptibility data for both the complexes, providing confidence in the extracted *J* values. All the computed

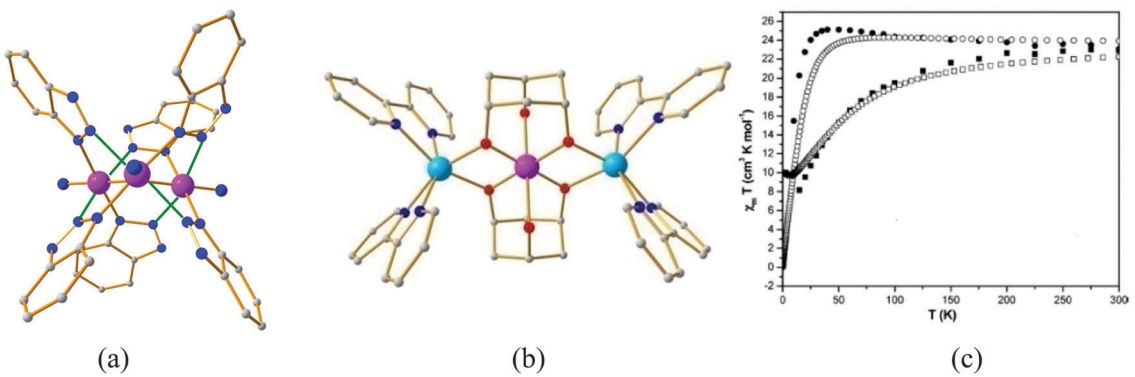

Fig. 4 (a) Crystal structure of **10** showing the position of the Jahn–Teller axis in green. (b) Crystal structure of **11**. (c) Variable temperature magnetic susceptibility plot for complexes **14** and **15** along with DFT computed data. The filled squares and circles correspond to experimental data, while the empty squares and circles represent DFT computed data for complexes **14** and **15**, respectively. Reprinted with permission from ref. 43. Copyright 2004 American Chemical Society.

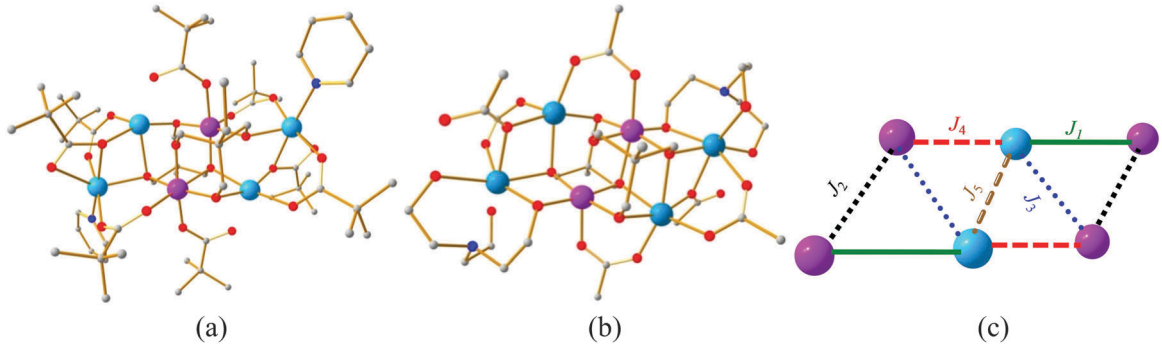

Fig. 5 Crystal structures of complexes (a) **14** and (b) **15**, where both the structures contain the $\{Mn^{III}_2Mn^{II}_4\}$ core unit. (c) Schematic of the five different DFT-computed exchange interactions where J_1 = −12.0, J_2 = −1.4, J_3 = +6.0, J_4 = +0.6, and J_5 = +3.0 cm^{-1} for **14**, J_1 = +4.8, J_2 = +0.2, J_3 = +2.0, J_4 = −4.0, and J_5 = −0.8 cm^{-1} for **15**, J_1 = −7.1, J_2 = −7.8, J_3 = +2.6, J_4 = −0.9, and J_5 = −6.8 cm^{-1} for **16**, J_1 = −7.6, J_2 = −5.0, J_3 = +6.8, J_4 = +0.2, and J_5 = +0.7 cm^{-1} for **17**, J_1 = −5.2, J_2 = −2.2, J_3 = +0.5, J_4 = +2.1, and J_5 = +4.9 cm^{-1} for **18**. {Note: all the J values given are in cm^{-1}}.

J values are weakly ferromagnetic or antiferromagnetic; of particular interest here is the Mn^{III}–Mn^{III} interaction present at the centre of the cluster. This interaction in both complexes (**14** and **15**) belongs to type II, as defined earlier. As per expectations, the J values were determined to be ferromagnetic and antiferromagnetic, respectively. The primary reason for the switching of the ground state is the J_5 interactions, which are found to be ferromagnetic in complex **14** and antiferromagnetic in complex **15**, leading to S = 4 and S = 0 ground states, as illustrated in Fig. 4c.[43]

Further to these examples, three structural analogues of $\{Mn^{III}_2Mn^{II}_4\}$ mixed-valance Mn_6 complexes have been studied in detail using DFT methods: $[Mn_6(acac)_4(OAc)_2(Htmp)_2(H_2N\text{-}ep)_2]$ (**16**), $[Mn_6(OAc)_8(tmp)_2(py)_4]$ (**17**), and $[Mn_6(OAc)_8(thme)_2(py)_4]$ (**18**) [H_3tea: triethanolamine; H_3tmp: 1,1,1-tris(hydroxymethyl)-propane; H_2N-H_2ep: 2-amino-2-ethyl-1,3-propanediol; H_3thme: 1,1,1-tris(hydroxymethyl)ethane]. The coupling scheme adapted is similar to the earlier examples, and the computed exchange interactions (see Fig. 5c) are in agreement with the experiments. Here, complex **16** possesses an S = 0 ground state, while **17** and **18** possess S = 4 ground states. The main difference in the magnetic properties arises from the J_5 interactions, which are found to be antiferromagnetic in complex **16** and ferromagnetic in complexes **17** and **18**. This interaction causes changes in the ground state, as illustrated earlier for complexes **14** and **15** (see Fig. 4d). The J_5 $\{Mn^{III}$–$Mn^{III}\}$ interaction is found to be type I in complex **16** and type II in complexes **17** and **18**, leading to antiferromagnetic and ferromagnetic coupling, as expected.[44]

In hexanuclear Mn clusters, oximato bridged isovalent $\{Mn^{III}_6\}$ clusters are important to note here, as some of the structures are reported to possess S = 12 ground states with D values as large as −0.43 cm^{-1}, leading to the observation of the largest U_{eff} of 86 K reported to date for any polynuclear transition metal complexes.[45,46] It is worth noting here that this Mn_6 cluster broke the U_{eff} record of the classical Mn_{12}Ac after ∼15 years. Although Brechin *et al.* have reported a series of $\{Mn^{III}_6\}$ clusters, DFT calculations have been performed on six $\{Mn^{III}_6\}$ clusters possessing the molecular formulas $[Mn_6O_2(H\text{-}sao)_6(O_2CH)_2(MeOH)_4]$ (**19**), $[Mn_6O_2(Me\text{-}sao)_6(O_2CCPh_3)_2(EtOH)_4]$ (**20**), $[Mn_6O_2(Et\text{-}sao)_6(O_2CPh^2OPh)_2(EtOH)_4]$ (**21**), $[Mn_6O_2(Et\text{-}sao)_6\{O_2CPh(Me)_2\}_2(EtOH)_6]$ (**22**) (see Fig. 6a for X-ray structure), $[Mn_6O_2(Me\text{-}sao)_6(O_2C\text{-}th)_2(EtOH)_4(H_2O)_2]$ (**23**), $[Mn_6O_2(Et\text{-}sao)_6(O_2C_{12}H_{17})_2(EtOH)_4(H_2O)_2]$ (**24**) [Et-saoH$_2$: 2-hydroxypropiophenone oxime, Me-saoH$_2$: 2-hydroxyethanone oxime, HO_2CCPh_3: triphenyl acetic acid, HO_2CPh^2OPh: 2-phenoxybenzoic acid, $HO_2C_{12}H_{17}$: adamantine acetic acid, HO_2C-th: 3-thiophene carboxylic acid]. In this series, except complex **22**, all other complexes possess S = 4 ground states. Five different exchange interactions are computed on this cluster (see Table 1) and except for complex **22**, where all the five interactions are ferromagnetic, weak ferro/antiferromagnetic couplings are noted. An adapted exchange scheme along with the DFT computed Js (see Fig. 6b) are given in Table 1, and they show an excellent fit to the susceptibility data (see Fig. 6c). In these clusters, the J_1–J_3 interactions have $\{Mn^{III}(O)(O\text{-}N)Mn^{III}\}$ cores, while the J_5 interaction is mediated *via* the $\{Mn^{III}_2(OR)_2\}$ core. The J–T axes in the J_5 interactions belong to type II, as defined earlier, and are expected to exhibit weak ferromagnetic or antiferromagnetic interactions. As the Mn–O–Mn angles are constrained in the polynuclear framework (for all structures, the Mn–O–Mn angles are in the range of ∼94 to ∼121 degrees), the J_5 interaction is computed to be ferromagnetic in all the cases studied. The J_4 interactions belong to type II but have $\{Mn^{III}(O)(O\text{-}N)Mn^{III}\}$ cores. The J_4 interaction is found to be weakly ferro or antiferro across all structures studied (see Table 1). On the other hand, the J_1–J_3 interactions in these structures belong to type I, but the Js are found to vary from −21 cm^{-1} to +5.8 cm^{-1}. This deviation is essentially due to the fact that the J–T angles for the J_1–J_3 interactions are not close to zero, as observed in the dinuclear complexes. The J–T angle (see Table 1) is found to vary significantly in the Mn_6 framework from 2 to 15 degrees in the studied structures. Therefore, the J_1–J_3 interactions are truly between type-I and type-III motifs, leading to a variation in the J values. It is important to note here that the Mn–N–O–Mn dihedral angle plays a very important role in determining both the sign and strength of J_1 to J_4 in these clusters, and magneto-structural correlations have been developed to show the switching of the sign of the Js in these clusters.[45]

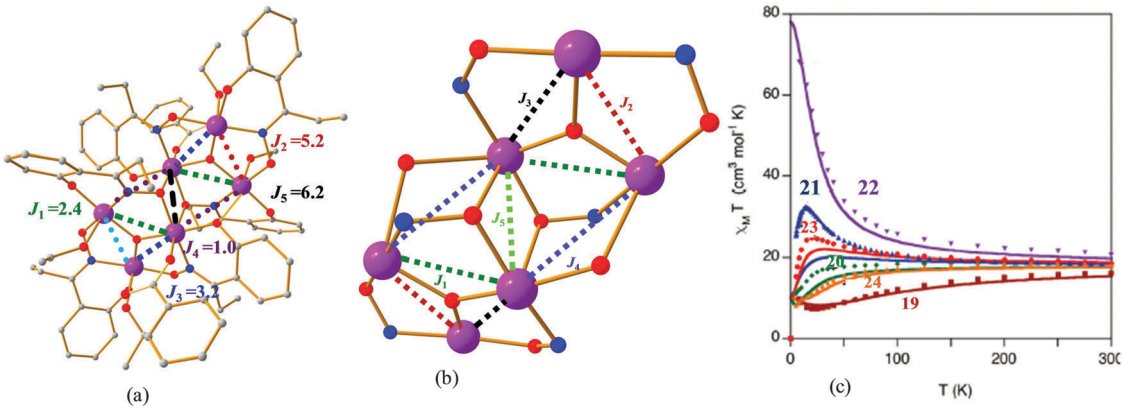

Fig. 6 (a) Crystal structure of **22** showing five different DFT-calculated exchange interactions. (b) Adapted exchange scheme used for DFT calculations on complexes **19–24**. (c) Representation of the magnetic susceptibility data for complexes **19–24**, wherein the solid symbols correspond to the experimental data while the solid lines correlate to the computed data. Reprinted with permission from ref. 45. Copyright 2009 American Chemical Society. {Note: all the J values given are in cm^{-1}}.

Table 1 Five calculated J values as depicted above in Fig. 6b, J–T angle between the J–T axes in all eight complexes, and their total ground spin states[45]

Complexes	J–T angle (°)	J_{cal} (cm^{-1})	S_{cal}
19	1.6, 13.2, 15.7, 160.2, 180.0	−21.0, −6.2, +2.6, −1.0, +5.8	4
20	13.5, 3.5, 6.0, 169.0, 180.0	+2.4, −3.2, −3.0, −1.6, +6.4	4
21	16.5, 7.4, 7.9, 167.2, 180	+6.2, −6.8, +1.6, −0.4, +7.2	4
22	15.2, 10.9, 7.6, 171.2, 180	+2.4, +5.2, +3.2, +1.0, +6.2	12
23	2.7, 13.6, 2.6, 170.4, 180	−4.6, +4.6, −3.6, −1.4, +4.2	4
24	16.3, 9.6, 9.6, 168.0, 180.0	−0.04, +5.8, −1.8, +0.1, +6.6	4
25	11.5, 3.1, 10.1, 170.8, 180	−2.2, +3.8, +3.2, −2.4, +5.8	1
26	23.6, 16.3, 9.3, 162.0, 180	+6.8, +1.2, +3.4, −0.2, +7.0	12

Further modifications in the oxime bridged $\{Mn^{III}_6\}$ clusters (**25** and **26**) been prepared, and DFT calculations have been performed, where weak ferromagnetic or antiferromagnetic couplings are noted due to variation in the Mn–O–N–Mn dihedral angles (see Table 1 for molecular formulas and computed coupling constants).[47] On heptanuclear clusters, DFT calculations have been performed on two mixed valent $\{Mn^{II}_4Mn^{III}_3\}$ discs, such as Mn_7 clusters, by Christou *et al.*[48] Calculations have been performed on $\{[Na(MeOH)_3][Mn_7(N_3)_6(mda)_6]\}_n$ (**27**) and $\{Na[Mn_7(N_3)_6(teaH)_6]\}_n$ (**28**) (see Fig. 7a) clusters to rationalize the observations of their S = 11 and S = 16 ground states, respectively. The computed J values along with the adapted exchange scheme are shown in Fig. 7a. The exchange interactions are between Mn^{II}–Mn^{III} and Mn^{II}–Mn^{II} pairs and are found to be weakly ferromagnetic to weakly antiferromagnetic. The increase in the ground state S value from S = 11 to S = 16 was attributed to the switching of Mn^{II}–Mn^{III} and Mn^{II}–Mn^{II} exchanges mediated *via* (μ_3-OR) bridges in these two complexes.[48]

To understand how the ground state and the magnetic properties are altered by oxidation states, DFT calculations were performed on four homo and heterovalent Mn_7 disklike clusters possessing the molecular formulas $[Mn^{II}_4Mn^{IV}_3(tea)(teaH_2)_3(peolH)_4]$ (**29**), $[Mn^{II}_4Mn^{III}_3F_3(tea)(teaH)(teaH_2)_2(piv)_4(Hpiv)(chp)_3]$ (**30**), (see Fig. 7b)[49] $[Mn^{II}_7(pppd)_6(tea)(OH)_3]$ (**31**) and $[Mn^{II}_7(paa)_6(OMe)_6]$ (**32**) ($teaH_3$ = triethanolamine, $peolH_4$ = pentaerythritol, Hpiv = pivalic acid, Hchp = 6-chloro-2-hydroxypyridine, pppd = 1-phenyl-3-(2-pyridyl)propane-1,3-dione; paaH = *N*-(2-pyridinyl)acetoacetamide). The ground state S was found to vary from 29/2 to 5/2 among these complexes. DFT calculations have been performed both on

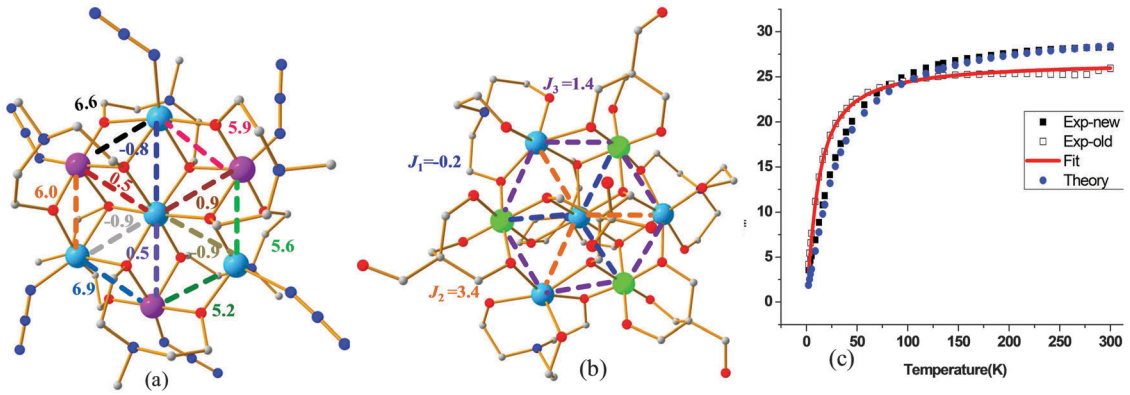

Fig. 7 Crystal structure of complex **27** showing all the possible exchange interactions. (b) Crystal structure of complex **29** (same colour scheme as earlier, with the addition of Mn^{IV}: light green). (c) Thermal variation of $\chi_M T$ for **32** from 300 to 2 K under a magnetic field of 1 T. Reprinted with permission from ref. 50. Copyright 2015 Wiley-VCH. {Note: all the J values given are in cm^{-1}}.

the full structures and on the dimeric building units to unravel the exchange pathways and their origins. Based on their structural topologies, three to eight different exchanges have been assumed in these clusters. Calculations offer weak ferromagnetic or antiferromagnetic exchanges for all the clusters. Among the structures studied, only one exchange was found between Mn^{III}–Mn^{III} pairs (mediated *via* μ_2-F and μ_3-O{$teaH^{2-}$} motifs), and this exchange was computed to be weakly ferromagnetic. This is consistent with the type II behaviour observed based on the J–T axis. For complexes **30** and **32**, significant deviations between the computed and experimental susceptibility data were observed. To ensure that the experimental data is reliable, the complexes were remade and susceptibility data were collected for the fresh samples (see Fig. 7c for the susceptibility plot of complex **32**). The new data collected matched strikingly with the DFT predicted behaviour, suggesting aging problems with the samples. This not only offers confidence for the computed value but clearly indicates the need for more than one experimental method; SQUID susceptibilities, INS, and EPR, in conjunction with each other or by other independent methods, can be used to validate experimental data and extract a reliable set of spin Hamiltonian parameters in polynuclear spin-coupled clusters.[50]

On the octanuclear front, two weakly connected $\{Mn_4^{III}\}$ complexes have been made and characterized using DFT. For the complex $[Mn_4O_2\text{-}(RCO_2)_6(pz)(H_2L)]_2$ (**33**) [H_4L, 1,3-bis[3-oxo-3-(2-hydroxyphenyl)propionyl]-2-methoxybenzene], four different exchange couplings are noted; the body–body exchange is found to be strongly antiferromagnetic in nature (see Fig. 8a). The J_{bb} is noted as -62.4 cm^{-1}, which is strongest among all the *J*s observed for all the complexes covered here. This unprecedentedly large *J* is essentially due to the near linear Mn–(μ_3-O)–Mn pathway. As the J–T axis runs along the bridge, significant overlap between the d_{z^2} is expected, leading to very strong antiferromagnetic coupling (see Fig. 8a). Other interactions were found to be weakly antiferromagnetic or ferromagnetic in nature.[51]

Calculations on larger nuclearity Mn clusters are a challenging task, as experimental fit to the susceptibility is cumbersome and inputs from calculations are needed if several exchange pathways are detected. In this regard, DFT calculations performed on a mixed valence $\{Mn_4^{II}Mn_6^{III}(\mu_4\text{-}O)_4(\mu_3\text{-}N_3)_4(hmp)_{12}\}^{2+}$ {hmp = 2-hydroxy-methyl pyridine} cluster (**34**) should be mentioned. Two exchange couplings comprising Mn^{III}–Mn^{III} (J_a) and Mn^{III}–Mn^{II} (J_b) were computed for complex **34**; both of these are ferromagnetic in nature, leading to an $S = 22$ ground state. The former interaction was found to be comparatively stronger, and this is essentially attributed to the mediation of *J via* the end-on-azido bridging ligand along this exchange pathway.[52]

There are several DFT studies on the magnetic coupling in dodecametallic Mn clusters.[53] DFT calculations were performed on the archetypical $[Mn_4^{IV}Mn_8^{III}O_{12}(CH_3COO)_{16}(H_2O)_4]$ (the Mn_{12}-acetate) (**35**).[54] Three different exchange couplings were assumed, and all were computed to be strongly antiferromagnetic in nature. However, a recent study aiming at computing all parameters, including the Heisenberg exchange, refutes this analysis and predicts weaker antiferromagnetic coupling.[55] These were also tested by simulating the full Hamiltonian using the Lancoz algorithm.[21] DFT calculations of exchange coupling on $[Mn_6^{III}Mn_6^{II}(O_2CMe)_{14}(mda)_8]$ (mda = *N*-methyldiethanolamine) (**36**) had been reported independently earlier.[56] This earlier report assumed six different exchange interactions to probe the origin of the $S = 7/2$ ground state obtained for this cluster, while the later report assumed 12 different exchanges, including next-nearest-neighbour/three-four body spin terms of the Hamiltonian. Calculations yielded small or negligible next-nearest neighbour interactions; interestingly, if these interactions were included, the standard deviations were found to be smaller.[53]

DFT calculations on other dodecametallic wheels include studies on the $[Mn_{12}^{III}(OMe)_{16}(L)_4(O_2CCMe_3)_4(MeOH)_4]$ (**37**) {L = proligand made up of phenolic oximes and diol moieties} (see Fig. 8c) wheel, where Mn^{III} ions are arranged sequentially. As in the earlier Mn_{12} cluster, in this cluster, the next-nearest (1,3) neighbour and next-next-nearest (1,4) interactions are computed to be very small (see Fig. 9a). The three nearest-neighbour interactions are found to be ferromagnetic in nature ($J_1 = +22.2$, $J_2 = +13.4$ and $J_3 = +3.8$ cm^{-1}) while all the other (1,3)/(1,4) interactions (J_4, J_5, J_6, J_7, J_8 and J_9) are found to be very weak (-0.14 to $+0.02$ cm^{-1}) in nature (see Fig. 9a). These J_1–J_3 interactions correspond to the Mn^{III}–Mn^{III} pair; they fall under

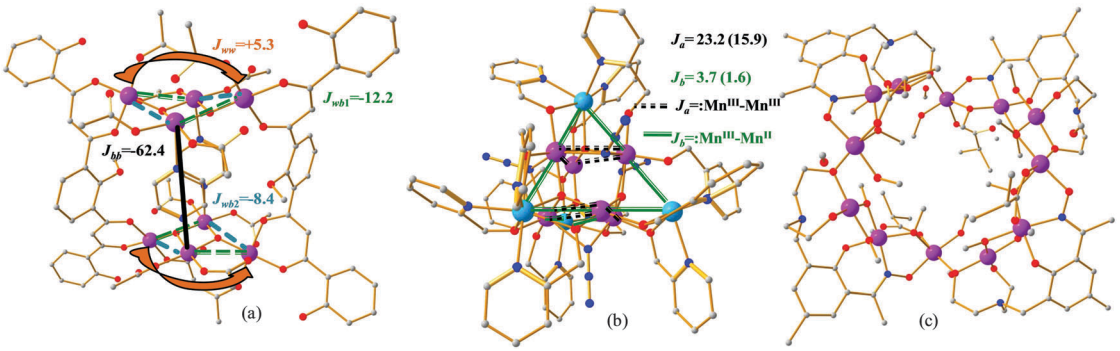

Fig. 8 (a) Crystal structure of **33** with DFT computed exchange interactions. (b) Crystal structure of **34** with DFT computed exchange interactions. The two values of exchange correspond to the results obtained based on two different levels of theory: PBE and B3LYP (within parentheses). (c) Crystal structure of **37**. {Note: all the *J* values given are in cm^{-1}}.

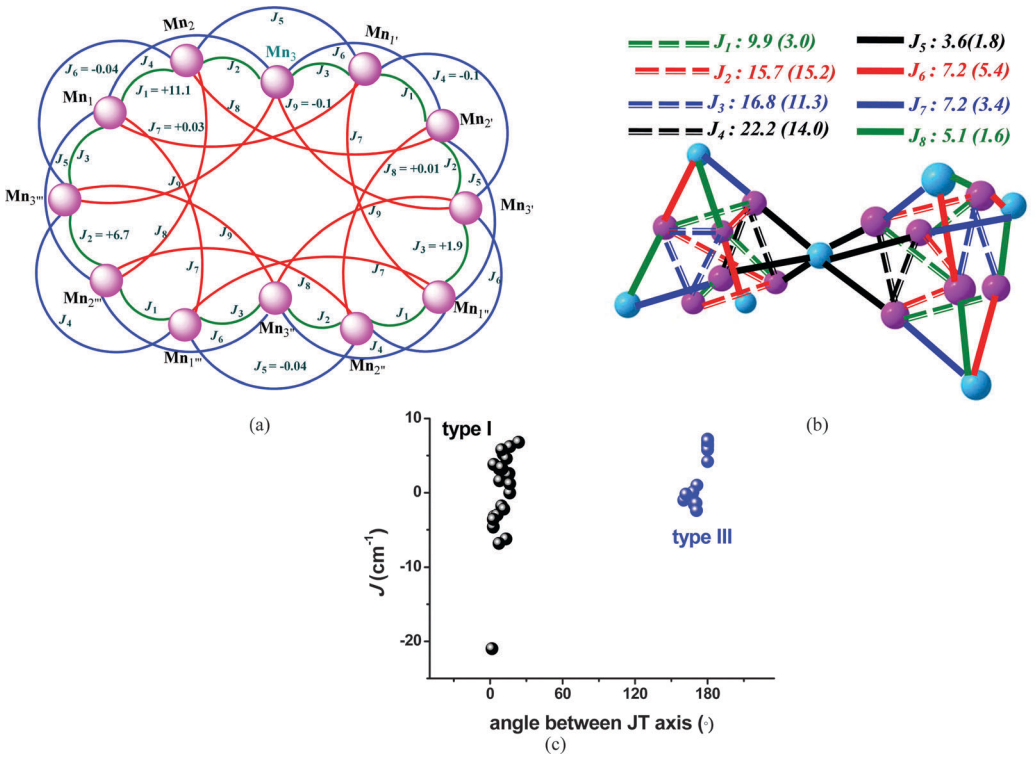

Fig. 9 (a) Schematic exhibiting DFT-computed exchange interactions in the dodecametallic wheel $[Mn^{III}_{12}(OMe)_{16}(L)_4(O_2CCMe_3)_4(MeOH)_4]$. All the exchange interactions depicted in this figure are based on $-2JS_1S_2$ formalism. (b) Schematic of DFT-computed exchange interactions in complex **39**. (c) The bottom origin plot implies the correlation between the magnetic exchange interaction (J) and the angle between the JT axis. The plot was constructed upon analysis of several studied complexes. All the points correspond to the data collected in Table 1 for complexes **19** to **26**.

the type-III category and yield ferromagnetic coupling, as expected. With increasing angle between the J–T axes (87.2°, 100.9° and 126.7° respectively for J_1, J_2 and J_3), the orthogonality between the two d_{z^2} orbitals is destroyed. This further reduces the cross-interaction between the d_{z^2} and empty $d_{x^2-y^2}$ orbitals, resulting in suppressed J_F contribution and leading to a decrease in the net J value. This analysis suggests that not only can the sign of J be qualitatively predicted for larger clusters, but the magnitude of J can also be rationalized based on the defined angle.[57]

Studies on other Mn_{12} structures include $[Mn^{III}_{12}O_4(H_3L)_8(H_2L)_4(TMA)_4]$ complex (**38**) {TMA = trimesic acid, L = proligand made up of phenolic oximes and diol moieties}. This complex comprises four triangles; each is composed of three Mn^{III} ions bridged by a μ_3-O^{2-} ion, an –N–O– oxime bridge and a carboxylate. DFT calculations yield $J_1 = +12.2, J_2 = +5.8, J_3 = -1.6$ and $J_4 = +0.04$ cm^{-1}, respectively. These ranges of exchange values categorize complex **38** as type III as per our earlier definition. The calculated values are found to correlate well with the J–T dihedral angle, as this value is found to vary from 25 to 8 degrees for these interactions. Additionally, the exchange interactions are also controlled by the Mn–O–Mn angle (minor variations) and the Mn–N–O–Mn torsional angle.[58]

There are only a limited number of studies on clusters beyond 12 Mn ions, as this requires significant computing time and comparison to experiments requires time consuming MC/QMC simulations. One elegant work which should be mentioned here is the computation of exchange coupling in a mixed-valance $\{Mn_{19}\}$ cluster ($Mn^{II}_7Mn^{III}_{12}$) (**39**) $\{Mn^{III}_{12}Mn^{II}_7(\mu_4\text{-}O)_8(\mu_3,\eta^1\text{-}N_3)_8(HL)_{12}(MeCN)_6^{2+}\}$ {H_3L = 2,6-bis(hydroxyl-methyl)-4-methylphenol}. Two different exchanges have been classified in the $\{Mn_{19}\}$ complex (see Fig. 9b), symbolizing J_1 to J_4 (through μ_4-O and μ_3-N_3 bridges) for Mn^{III}–Mn^{III} interactions and J_5 to J_8 (through μ_4-O and μ-OR) for Mn^{III}–Mn^{II} interactions. All the J values are found to be FM in nature, where J_1 to J_4 show stronger interactions as compared to J_5 to J_8, leading to an S = 83/2 ground state.[52] With eight different exchanges, QMC simulations astonishingly reproduced the experimental data. This reaffirms that for this large cluster with multiple J values, DFT calculations are the only viable option to estimate the magnetic interactions. Apart from Mn clusters, transition metal clusters based on other metal ions have been studied in detail using DFT calculations.[10,25a,59]

Beyond dimeric systems, we have chosen several polynuclear complexes with an aim to shed light on the common outcome of exchange analysis in these systems. We have reached the following conclusions: (a) three categories of complexes (type-I, II and III) are classified based on the variation in the angle between the J–T axes. This classification is also found to rationalize the sign and to a certain extent the magnitude of Js in polynuclear compounds (see Fig. 9c). (b) Next-nearest-neighbour interactions may not be negligible in all cases and may be required in some systems to precisely reproduce the experimental data. (c) The Mn–O–Mn angle and the Mn–O distances

are found to be prominent parameters that influence the exchange coupling. If these two parameters are similar, then other structural parameters such as torsion angle play a proactive role in determining the sign and strength of the *J* values. (d) For very large clusters possessing multiple exchange coupling, although the sign could be determined qualitatively from the structural parameters, hints to the strength must be ascertained from DFT calculations. With the tremendous increase in computing power in recent years, calculations can be performed even on very large clusters.

3.1.3 Modelling isotropic *J* in 3d-Gd^{III} SMMs. In this topic, we intend to review calculations with the aim to obtain isotropic exchange interactions in di- and polynuclear 3d-Gd complexes. As the incorporation of paramagnetic 3d metal ions is found to quench the QTM effects, these mixed {3d-4f} clusters have gained significant attention.[60,79] To quench the QTM significantly, very strong exchange interactions are needed.[60] Among all the 4f-elements, only Gd^{III} is isotropic in nature due to its pure $S = 7/2$, $L = 0$, orbitally nondegenerate ground state. Since DFT calculations can be employed straightforwardly to compute *J*s only in isotropic scenarios, our review will focus on the estimation of *J* values in di- and polynuclear {3d-Gd}[26] clusters. Apart from G09,[61] the SIESTA or NWCHEM suites are often employed to extract the *J*s in these clusters.[62] The first theoretical studies on 3d-Gd complexes were performed on a dinuclear [LCu^{II}Gd^{III}(NO$_3$)$_3$] complex (**40**) {L = 1,2′-bis((3-methoxysalicylidene)diamino)-2-methylpropane} (see Fig. 10a for the crystal structure).[63] The quest in this work is to probe the intrinsic ferromagnetic coupling observed between Cu^{II} and Gd^{III} ions in the majority of the complexes reported.[26,64] Due to the contracted nature of the Gd^{III} 4f orbitals and shielding by the 5s/5p occupied orbitals, a direct super-exchange mechanism between Cu^{II}-3d and Gd^{III}-4f is not viable. Several qualitative mechanisms for magnetic coupling for the {3d-Gd} pair have been proposed. Gatteschi *et al.* proposed a spin polarization mechanism with participation of the 6s orbital, while Kahn *et al.* proposed the participation of the 5d orbitals in the magnetic coupling.[65]

The *ab initio* calculations affirm weak overlap between the 4f-Gd^{III} and 3d-Cu^{II} orbitals. Moreover, the interaction between the 4f:Gd^{III}–3d:Cu^{II} ground configuration (GC) and the metal–metal charge transfer configuration (CTC) is also found to be inoperative. This means that it is imperative to consider another mechanism of fractional electron transfer from the singly occupied Cu^{II} orbital to the formally empty 5d-Gd^{III} orbital. This was substantiated by the larger transfer integral for the 5d-3d pathway than 4f-3d, as estimated using the extended Huckel approach. State-of-the-art quantum chemical calculations (CASSCF, CASPT2, MS-CASPT2)[63] reiterated Kahn's proposal of the involvement of the formally empty 5d-Gd^{III} orbital in the exchange. Moreover, these *ab initio* calculations also supported Gatteschi's statement of participation of spin polarization in the magnetic exchange.

The first attempt to reliably compute the isotropic exchange coupling in the {Cu–Gd} pair using DFT calculations has been undertaken on four structurally analogous complexes (**41** to **44**) (see Table 2). B3LYP/all-electron Douglas–Kroll–Hess (DKH) or zeroth-order regular approximation (ZORA) combination were found to yield good numerical estimates of the *J* values in this set of studied complexes.[66] An elaborate method assessment with ten different exchange–correlation functionals and with a combination of four different basis sets to estimate the magnetic coupling in {Cu–Gd} has been undertaken by us.[67] This assessment recommends the use of the B3LYP functional with a combination of an effective core potential basis set or the use of all electron basis sets with the relativistic effects incorporated explicitly *via* the DKH or ZORA methods. Participation of the Gd^{III}-5d orbital in the exchange is reaffirmed by analyzing the Kohn Sham orbitals and their energies. This is essentially due to the closer location of Gd^{III}-5d to Cu^{II}-d$_{x^2-y^2}$ in terms of energy (see Fig. 10b). Based on our analysis, we propose that interactions between Cu^{II}-3d and Gd^{III}-5d contribute to the J_F part of the total exchange, while interactions between Cu^{II}-3d and Gd^{III}-4f have two contributions: among the seven 4f-Gd^{III} orbitals, two overlap with the Cu^{II}-d$_{x^2-y^2}$ orbital, and this contributes to the J_{AF} part of the total exchange. Meanwhile,

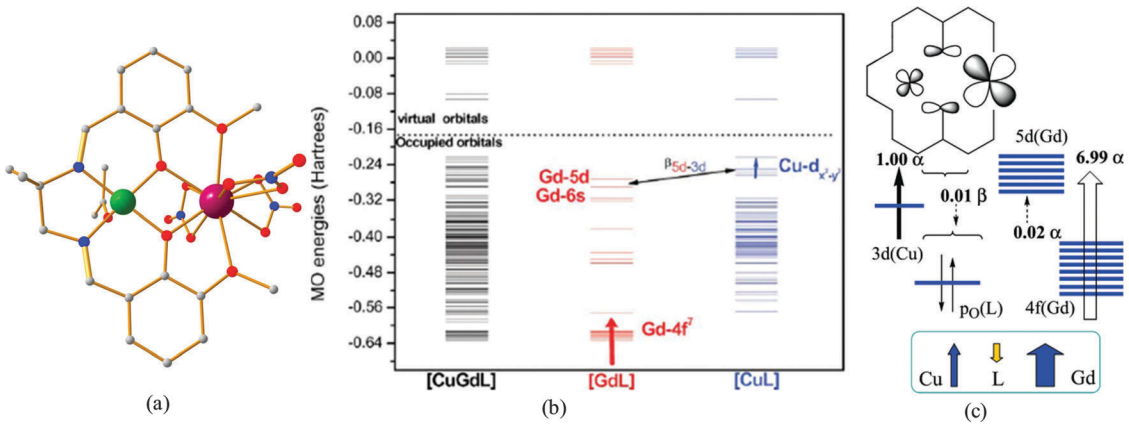

Fig. 10 (a) Crystal structure of complex **40**. (b) MO energy level diagram in complex **45** obtained employing B3LYP/CSDZ methodology. The blue and red arrows signify the approximate positions of unpaired electrons. The double headed arrow and the charge transfer integral denote the charge transfer between the two orbitals. Reproduced from ref. 67 with permission from the Royal Society of Chemistry. (c) Schematic of spin polarization over Cu^{II}, Gd^{III} and the ligand in complex **40**. Reprinted with permission from ref. 63. Copyright 2004 American Chemical Society.

Table 2 Collected {3d-Gd^{III}} di, tri, and tetranuclear complexes along with experimental and theoretical exchange estimates (in cm^{-1}), 3d-O–Gd angles and 3d-O–Gd–O dihedral angles

Molecular formula	J_{exp}	J_{cal}	M–O–Gd	M–O–Gd–O
$[L^{40}Cu^{II}Gd^{III}(NO_3)_3]$ (**40**)[63,66,210a]	+7.0	+2.4	107.4, 105.9	10.2
$[L^{41}Cu^{II}Gd^{III}(NO_3)_3]_3$ (**41**)[66,210b]	+1.3	+4.6	106.8, 105.1	4.05
$[L^{42}Cu^{II}Gd^{III}(CF_3SO_3)(H_2O)_3]$ (**42**)[66,210c]	−0.1	+8.9	104.7, 105.5	0.49
$[L^{43}Cu^{II}Gd^{III}(hfac)_3]$ (**43**)[66,210d]	+1.3	+4.6	93.1, 98.5	34.3
$[L^{44}Cu^{II}Gd^{III}(-H_2O)_4Cl_2]Cl$ (**44**)[66,210e]	+10.1	+8.5	108.7, 108.8	1.4
$[L^{45}Cu^{II}Gd^{III}(O_2CCF_3)_3(C_2H_5OH)_2]$ (**45**)[67]	+4.4	+5.9	103.3	10.3
$[L^{46}Cu(H_2O)_2Gd(NO_3)_3]$ (**46**)[70]	−0.5 to +7	+5.8	106.5, 107.9	2.8
$[Mn^{II}Gd^{III}\{pyCO(OEt)pyC(OH)(OEt)py\}_3]$ (**47**)[68]	−1.7	−2.7	86.9, 87.6, 88.3	37.6
$[L^{48}Mn^{II}(H_2O)_2Gd^{III}(NO_3)_3]$ (**48**)[70]	−1.7	+1.2	106.5, 107.9	2.8
$[Fe^{II}Gd^{III}L^{49}\text{-}(MeOH)(NO_3)_3]$ (**49**)[68]	+1.0	+1.4	107.3, 106.3	5.0
$[L^{48}Fe^{II}(H_2O)_2Gd^{III}(NO_3)_3]$ (**50**)[70]	0.2 to 0.5	+1.4	106.5, 107.9	2.8
$[L^{48}Ni^{II}(H_2O)_2Gd^{III}(NO_3)_3]$ (**51**)[70,71,210f]	−0.2 to 3.6	2.2/2.1	106.5, 107.9	2.8
$[(Ni^{II}L^{52})Gd^{III}(hfac)_2(EtOH)]$ (**52**)[71,210g]	0.34	0.36	90, 90.7 and 91.7	34.6, 38.4 and 38.9
$[L^{53}V^{IV}(O)Gd^{III}(H_2O)(NO_3)_3]$ (**53**)[72,210i]	1.5	2.2	107.1	2.83
$[L^{54}V^{IV}(O)\text{-}\{(CH_3)_2CO\}Gd^{III}(NO_3)_3]$ (**54**)[72,210i]	−2.6	−0.7	105.4	18
trans-$[Cr^{III}F_2(py)_4]Gd^{III}(hfac)_4$ (**55**)[73]	−0.82/−0.84	−0.80	178.3[a]	
$[Fe^{III}F_2(py)_4Gd^{III}(hfac)_4]$ (**56**)[74]		1.1	178.3[a]	
$[(L^{57}Ni(H_2O))_2Gd(H_2O)]^{3+}$ (**57**)[71,210h]	4.8, 0.1	2.2, 2.1, −0.2	106.9 to 108.2	15.3
$[(L^{58}Ni)_2Gd]^{+}$ (**58**)[71,210h]	0.91	0.6, 0.6, −0.1	95.0 to 96.2	35.8 to 37.4
$[Gd^{III}{}_2Cu^{II}{}_2(OH)_2(NO_3)_{2.5}(OAc)_{3.5}(L^{59})_2]_n$ (**59**)[75]	17.1, −2.1 and 2.6	6.0, −3.2, −3.7, 4.2, 4.1, 0.1, 0.1, 0.1	100.3 to 102.6	10–11
$[L^{60}V^{IV}(O)Gd^{III}(hfac)_2\text{-}(CH_3OH)_2]_2$ (**60**)[72,210j]	0.5	0.9	106.4	15.1
$[Ni(\mu\text{-}L^{61})(\mu\text{-}OAc)Gd(NO_3)_2]$ (**61**)[76]	1.4	2.1	101.3, 107.2	21.4, 22.0
$[Ni(H_2O)(\mu\text{-}L^{61})Gd(NO_3)_3]$ (**62**)[76]	2.2	3.3	109.3, 109.7	2.1
$[L^{63}Ni^{II}Gd^{III}(NO_3)_3(H_2O)]$ (**63**)[77]	0.6	0.1	103.1, 102.2	7.6
$[(CH_3CN)(H_2O)Ni^{II}(ovan)_2Gd^{III}(NO_3)_3]$ (**64**)[77]	2.3	2.9	106.6, 107.5	1.6
$[L^{65}Cu^{II}_2Gd]^{+}$ (**65**)[70]	5.0	1.1, 1.9, 0.7		
$[L^{65}Ni^{II}_2Gd]^{+}$ (**66**)[70]	−0.3	−0.2		
$[L^{65}Mn^{II}_2Gd]^{+}$ (**67**)[70]	0.1	0.2, −0.02		
$[L^{65}Fe^{II}_2Gd]^{+}$ (**68**)[70]	1.3	1.4		

L^{40} = 1,2′-bis((3-methoxysalicylidene)diamino)-2-methylpropane, L^{41} = *N*,*N*′-bis((5,6-dimethoxyphenolato-2-yl)methylene)ethylenediamine, L^{42} = 1,3-bis-(dimethylamino)-2-propanol, L^{43} = *N*,*N*′-bis(salicylidene)-2-aminobenzylamine; hfac = hexafluoroacetylacetanato, L^{44} = 1,2-bis((3-methoxy-salicylidene)amino)-2,2′-dimethylpropanato, L^{45} = *N*,*N*′-bis(3-ethoxy-salicylidene)-1,2-diamino-2-methylpropanato, L^{46} = [2,2′-[2,2-dimethyl-1,3propanediylbis(nitrilomethylidyne)]bis(6-methoxyphenolato)(2-)], L^{47} = [2,2′-[2,2-dimethyl-1,3propanediylbis(nitrilomethylidyne)] bis(6-methoxy-phenolato)(2-)], L^{49} = (H_2L = *N*,*N*′-bis(3-methoxysalicylidene)-1,3-diamino-2,2′-dimethylpropane), L^{52} = 1,1,1-tris(*N*-salicylideneaminomethyl)ethane, L^{53} = [*N*,*N*′-bis(3-methoxysalicylidene)-1,2-diamino-2-methylpropane], L^{54} = [*N*,*N*′-bis(3-methoxysalicylidene)-1,3-diamino-2-2′-dimethyl-propane], [a] Cr–F–Gd; L^{57} = *N*,*N*1-2,2-dimethylproppylenedi(3-methoxosalicylidene iminato), L^{58} = triamine 1,1,1-tris(aminomethyl)ethane, L^{59} = 2-pyridinyl-methanol, L^{60} = 2-hydroxy-*N*-{[[(2-hydroxyphenyl)-methylene]amino}-2-methylpropyl)benzamide, L^{61} = *N*,*N*′,*N*″-trimethyl-*N*,*N*″-bis(2-hydroxy-3-methoxy-5-methylbenzyl)diethylenetriamine, L^{63} = combination of 1,2-bis(3-aminopropylamino)ethane, *o*-vanillin and acetate; ovan = orthovanillin, L^{65} = (S)P[N(Me)N=CH-C_6H_3-2-OH-3-OMe]$_3$.

the remaining five interactions, being orthogonal, contribute to the J_F part of the total exchange (see Fig. 11a). As the J_F part dominates here, this leads to FM coupling, supporting our computed data. Among all the structural parameters, the Cu–O–Gd–O dihedral angle was found to play a proactive role in regulating the magnitude of the magnetic exchange. On increasing the dihedral angle, the magnitude of *J* gradually decreases.[67]

Another extensive theoretical study on several {3d-Gd} systems (see Table 2) was reported by Ruiz *et al.*;[68] this study provides further understanding of the mechanism of coupling in this area. Doubly bridging ligands were found to be more influential than triply-bridging ligands in inducing FM coupling for complexes with small 3d-O–O–Gd hinge angles.[68] Basis set assessment within DFT formalism has been attempted; it reveals that the 5d orbital of Gd^{III} ion (in the basis set of Gd) is imperative (see Table 3) in reproducing experimental data.

While the 6s orbital makes a very small contribution to the *J*s. Furthermore, the mechanistic study suggests that the spin polarization of the metal–ligand bonding electron pairs engages the formally empty 5d-Gd^{III} orbitals, implying that charge transfer is not a dominant component of the exchange coupling. Although much is known now about the mechanism of magnetic coupling in the {3d-Gd} pair, the contribution of the different components to the total exchange remains unexplored. An MRCI calculation such as that which has been undertaken on Cu^{II}-acetate by Loth *et al.*,[69] where individual contributions to the *J*s can be clearly established, would be needed to bring further clarity to the mechanism of magnetic coupling.

As the methodology is established, further calculations have been performed on other {3d-Gd} dimers (see Table 2). Very recently, an important contribution on the Cu^{II}–Gd^{III} complexes was published which suggested J_{CuGd} to be weakly FM for complexes bridged through single oxygen and three-atom bridges comprising O, C, and N atoms.[207] However, J_{CuGd} has been found to be weakly AFM in complexes bridged by two atoms, such as the N–O oximato bridge. The role of the spin populated Gd-5d orbital (the 6s orbital was discarded) in FM interaction was reiterated in {3d-Gd} complexes (3d ions possess half-occupied $3d_{x^2-y^2}$ orbitals). The singly occupied $3d_{x^2-y^2}$ orbital favours FM interaction, while the unoccupied $3d_{x^2-y^2}$ orbital leads to AFM interaction.

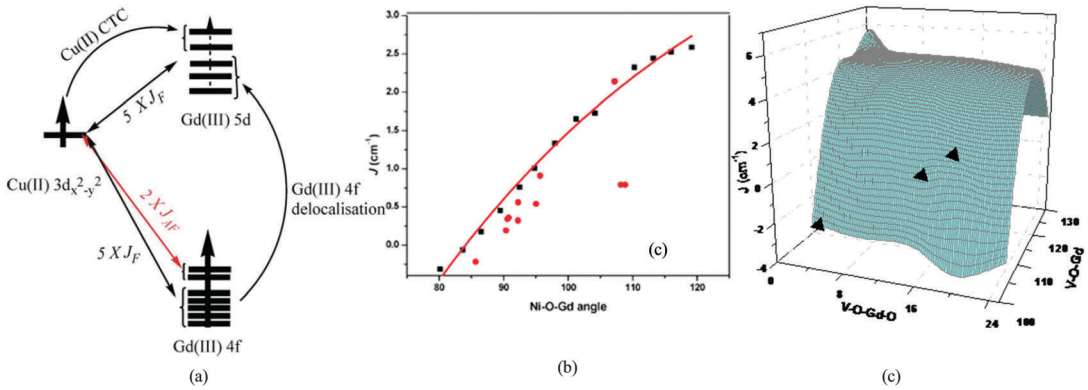

Fig. 11 (a) DFT computed schematic mechanism of magnetic exchange on complex **44**. Reproduced from ref. 67 with permission from the Royal Society of Chemistry. (b) Magneto-structural correlation developed on complex **50** by varying Ni–O–Gd angle. Reproduced from ref. 71 with permission from the Royal Society of Chemistry. (c) Magneto-structural correlation developed on complex **53** varying the V–O–Gd angle and V–O–Gd–O dihedral angle simultaneously. Reproduced from ref. 72 with permission from the Royal Society of Chemistry.

Table 3 Computed J (cm^{-1}), natural bonding orbital (NBO), atomic and spin (in parentheses) populations acquired employing B3LYP//ECP-CSDZ methodology for complex **43**

Basis set	J	4f (Gd)	5d (Gd)	6s (Gd)	3d (M)
hs, full basis set	+9.6	7.33 (6.67)	0.18 (0.029)	0.11 (0.00)	9.36 (0.56)
hs, no Gd 5d orbitals	−0.9	7.45 (6.54)		0.12 (0.00)	9.35 (0.57)
hs, no Gd 5d orbitals Without Cu^{II}	+10.2	7.10 (6.88)	0.23 (0.035)	0.10 (−0.01)	
ls, full basis set		7.32 (6.67)	0.19 (0.025)	0.09 (0.00)	9.36 (−0.53)

This eventually states that FM interaction might be enhanced by increasing the Gd-5d spin population.[207] To address the magnetic coupling for the $\{Ni^{II}Gd^{III}\}$ pair, calculations have been performed on two dinuclear and two trinuclear complexes (**51**, **52**, **57** and **58**). In all cases, DFT yielded good numerical estimates of the J values. For the trinuclear complexes, apart from the Ni–Gd interactions, the (1,3) Ni–Ni interactions were also computed; these were found to be significant compared to the transition metal clusters described above. This is due to the large and diffuse empty orbitals of Gd^{III}, which mediate relatively stronger coupling between two Ni^{II} ions. Extensive magneto-structural correlations performed on di- and trinuclear complexes reveal both the Ni–O–Gd angle and the Ni–O–Gd–O dihedral as important parameters (see Fig. 11b).[71] Calculations on complexes **61** and **62** (see Table 2) suggested a weak but considerable increment of J_{NiGd} with the planarity of the Ni–$(O)_2$–Gd bridging fragment (hinge angle; angle between the O–Ni–O and O–Gd–O planes) and with the increase of the Ni–O–Gd angle (θ).[76] Recently, DFT calculations on complexes **63** and **64** have envisaged that the hinge angle and θ angle are not sufficient to explain the observed trend of the J values. Moreover, the combined effect of a small θ and a large hinge angle, τ (O–Ni–O–Car torsional angle) and γ (Ni–O–Car–Car torsional angle) dictates the attenuation of the magnitude of magnetic exchange coupling constants.[77] Studies have been extended to a star-like $\{Ni_3Gd\}$ cluster $[Ni^{II}_3Gd^{III}\{(py)_2C(H)O\}_6]$ (**69**) {pyC(H)O$^-$ is the anion of di-2-pyridylmethanol}, where the Ni–Gd interactions are computed to be −1.4, −1.7 and −1.3 cm^{-1} (J_{exp} = −1.1 cm^{-1}) while the Ni–Ni interactions are estimated as −0.4, −0.3, and −0.6 cm^{-1} (J_{exp} = −1.0 cm^{-1}). Interestingly, the (1,3) Ni–Ni interactions are found to be as strong as the {Ni–Gd} interactions in this cluster, which results in significant spin frustration.[78] The computed values are in agreement with earlier experimental reports.

In another study, calculations been performed on two $\{V^{IV}–Gd^{III}\}$ dinuclear complexes, one possessing ferromagnetic coupling (**53**, see Table 2) and another possessing antiferromagnetic coupling (**54**). The sign of exchange is found to correlate to the overlap of the V^{IV} d_{xy} orbital with the Gd^{III} 4f orbitals. Controlled CASSCF calculations were performed to gain further clues on the mechanism of exchange. These calculations suggest that the d_{xy}–$f_{xyz}\{Gd^{III}\}$ overlap plays a proactive role in determining the sign of exchange in this set of complexes.[79] This was supported by our developed correlation, where the reduction of the V–O–Gd angle from 105.5° to 99.0° results in switching from ferromagnetic to antiferromagnetic interaction and subsequent enhancement of the d_{xy}–$f_{xyz}\{Gd^{III}\}$ overlap values. Notably, more than one structural parameter (V–O–Gd and V–O–Gd–O) is found to be imperative for switching the exchange from ferromagnetic to antiferromagnetic interaction (see Fig. 11c). Finally, calculations were performed on a dimer of dimers (tetrameric) $\{V^{IV}_2–Gd^{III}_2\}$ complex (**60**, see Table 2). The calculations yielded ferromagnetic interaction within the dimeric unit but very weak antiferromagnetic interaction between the dimers. This suggests an S = 0 ground state for the molecule, and the computed J values reproduce the experimental magnetic $\chi_m T$ data nicely up to 1.2 K.[72] Similar to this motif, where two dimers are connected by a bridge, DFT calculations have been employed to

extract {Cu–Gd} interactions in a one dimensional chain structure ($[Gd_2^{III}Cu_2^{II}(OH)_2(NO_3)_{2.5}(OAc)_{3.5}(L^{58})_2]_n$, **59**). Considering the complexity, eight different exchange couplings (Cu–Gd, Cu–Cu and Gd–Gd) were computed for this complex (see Table 2). The extracted exchange parameters were found to give a reliable fit to the magnetic susceptibility data.[75]

Contrary to the belief that {3d-Gd} interactions are ferromagnetic, we have witnessed a fluoride bridged complex (**55**) showing AFM interaction.[67,73] Unlike the other studied 3d metal ions, Cr^{III} does not possess any unpaired electrons in its e_g orbitals; this attenuates the charge transfer to the 5d orbitals of Gd^{III} ion, leading to competing ferro-antiferro coupling. On the other hand, the number of overlap values between the two sets of magnetic orbitals of Cr^{III}-3d and Gd^{III}-4f are larger compared to those of the Cu^{II}–Gd^{III} pair, resulting in a predominant J_{AF} contribution and, hence, a net antiferro-exchange. A magneto-structural correlation was developed by varying the Cr–F–Gd angle, where ferromagnetic interactions are detected at very small angles. Quite interestingly, if the J values of several polynuclear {CrGd} complexes synthesized are mapped along with the corresponding Cr–F–Gd angle, there is an astonishing match between the experimental and theoretical points; this highlights the potential of magneto-structural correlations in determining the sign/strength of the J values in polynuclear clusters.[80] This example illustrates that ferromagnetic couplings are not intrinsic to {3d-Gd} pairs, and several factors, such as the electronic configurations of the metal ions, the structural distortions and the nature of the bridging group, determine the sign of the J values.

The quest for the exchange interaction in the {3d-Gd} motif continued and directed us to explore these details in fluoride bridged trigonal bipyramidal {Fe^{III}/Cr^{III}–Gd^{III}} structures. DFT computations yielded AFM coupling for the {Cr^{III}–Gd^{III}} pair, while ferromagnetic exchange (1.1 cm^{-1}) was detected for the {Fe^{III}–Gd^{III}} [$Fe^{III}F_2(py)_4Gd^{III}(hfac)_4$] (**56**) pair.

Our developed magneto-structural correlations (see Fig. 12a) revealed an increase in the ferromagnetic $J_{Fe–Gd}$ exchange with

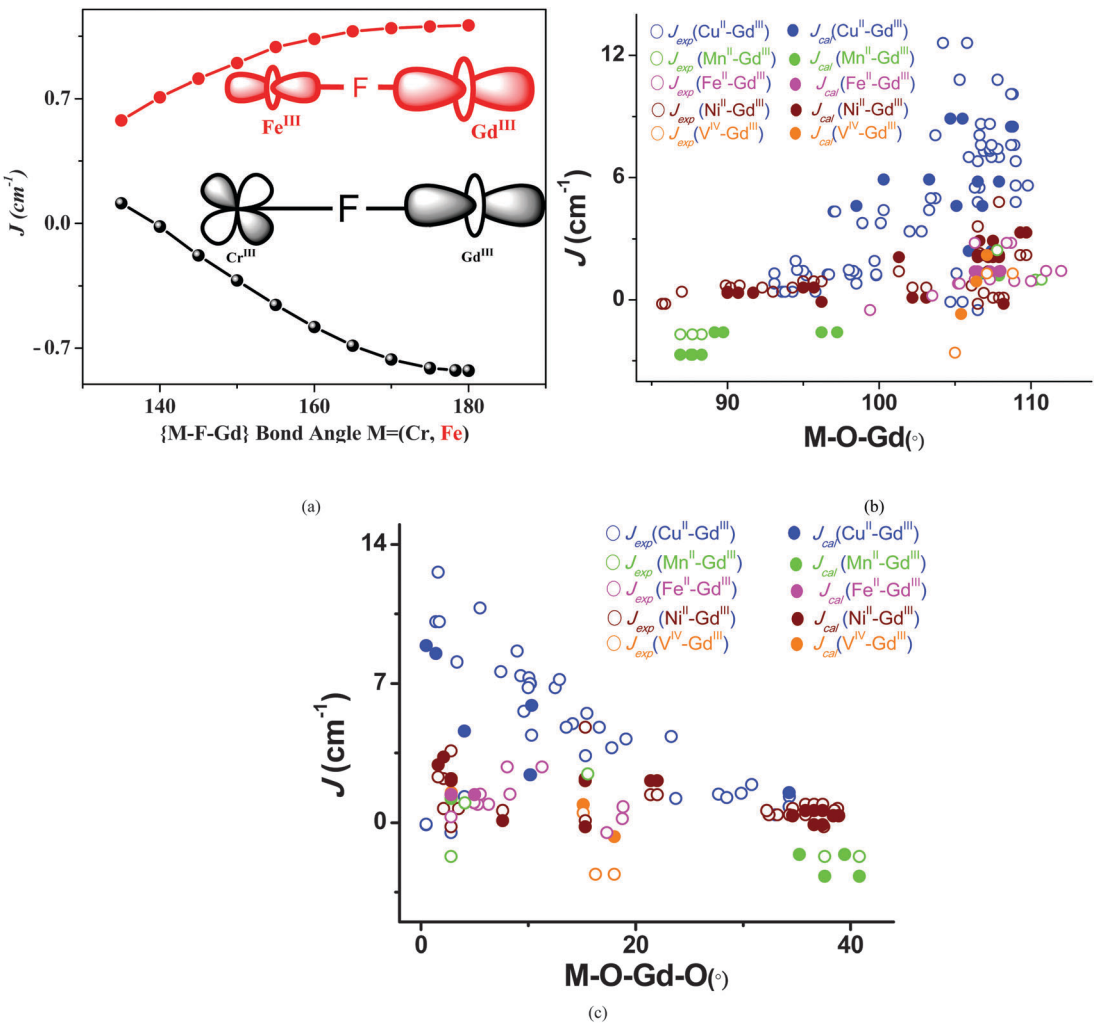

Fig. 12 (a) Magneto-structural correlation developed for complexes **55** and **56**. Adapted with permission from ref. 74. Copyright 2014 Wiley-VCH. (b) Schematic of the linear correlation between the 3d-O–Gd angle and the magnitude of J. (The empty circles imply experimental data, while the filled triangles correspond to computed values for the respective 3d-Gd series.) (c) Schematic of the linear correlation between the 3d-O–Gd–O dihedral angle and the magnitude of J. (The empty circles imply experimental data, while the filled triangles correspond to computed values for the respective 3d-Gd series.)

the bridging (Fe–F–Gd) angle, while the reverse trend was observed for the {Cr^{III}–Gd^{III}} pair. This can be attributed to the larger $Fe^{III}d_{z^2}$–Gd^{III}5d interaction, while for the {Cr^{III}–Gd^{III}} pair, this interaction decreases due to the enhanced orthogonality of the interacting orbitals.[74]

This growing confusion over ferro/antiferromagnetic coupling in {3d-4f} and the factors governing the coupling led us to perform detailed analysis[70] of the exchange on {3d-Gd} dimers (**48**, **50** and **51**, see Table 2) and {3d-Gd^{III}-3d} trinuclear complexes (**65–68**). Using DFT methods, some polynuclear {3d-Gd} clusters were studied, and we intend to describe them here in brief. The initial report includes studies on five polynuclear complexes, $[(NO_3)Mn^{II}(L)(\mu\text{-}NO_3)Gd^{III}(L)Mn^{II}(NO_3)]$ (**70**) {H_2L = *N*,*N*′-2,2-dimethylpropylenebis(3-methoxysalicylideneimine)}, $[Mn^{III}_2Gd^{III}_2O_2(O_2CCMe)_8(HO_2CCMe_3)_2(MeOH)_2]$ (**71**), $[Fe^{III}_4Gd^{III}_2(\mu_4\text{-}O)_2(NO_3)_2(piv)_6(Hedte)_2]$ (**72**) (H_4edte = *N*,*N*,*N*′,*N*′-tetrakis(2-hydroxyethyl)ethylenediamine) $[Et_4N][Ni^{II}_6Gd^{III}_2(val)_{12}(MeCN)_6(H_2O)_3][Gd(NO_3)_5](ClO_4)_5$ (**73**) {val = valine anion}, $[Fe^{III}_5Gd^{III}_8(\mu_3\text{-}OH)_{12}(L)_4(piv)_{12}(NO_3)_4(OAc)_4](H_3L)$ (**74**) {H_2L = *N*-butyldiethanolamine} (see Fig. 13).[81] As mentioned earlier, experimental fitting of magnetic data is cumbersome for large polynuclear complexes, and the situation is even more complex for large {3d-Gd} clusters because (i) the exchange interactions are often very small and can be FM or AFM in nature; (ii) such clusters often contain {Gd–Gd}, {3d-Gd}, and {3d–3d} interactions, and the magnitude of the *J*s for these pairs are in the following ranges: 10^{-3} to 1 cm^{-1}, 1 to 10 cm^{-1}, and 10 to 1000 cm^{-1}, respectively. These large {3d-Gd} clusters are also attractive, as they often possess very large MCE values. DFT calculations on the aforementioned four complexes reproduced experimental data nicely. Two exchange interactions are possible in face-sharing complex **70**, one *via* three bridging ligands (two μ_2-alkoxo and one μ-nitrate) and the other mediated through two μ_2-alkoxo bridges. The former resulted in antiferromagnetic coupling, while weak ferromagnetic coupling was computed between two centres bridged by two ligands in the face sharing complex; this is in accordance with the experimental trend (see Fig. 13). Three different exchanges are possible in complex **71** (see Fig. 13), among which the interaction between the two Mn^{III} ions is found to be the strongest (-67.2 cm^{-1}), while the three remaining interactions incorporating Gd^{III} are very weak in nature.

Calculations were undertaken on complex **72**, speculating six possible exchange interactions (see Fig. 13); this yielded an $S = 7$ ground state. Three possible exchange interactions, *i.e.* Ni^{II}–Ni^{II}, Ni^{II}–Gd^{III} and Gd^{III}–Gd^{III} in complex **73** (see Fig. 13), were found to be weak in nature; among these, the Ni–Ni interaction is antiferromagnetic, while the other two are weakly ferromagnetic in nature, leading to an $S = 13$ ground state. The study of complex **74** is of paramount importance, as it possesses a very large *S* value (81/2, very close to the largest value of $S = 83/2$ observed for the Mn_{19} cluster). Computations showed weak Fe^{III}–Gd^{III} interactions and much weaker Gd^{III}–Gd^{III} interactions, in compliance with previous studies on similar structural motifs, leading to an $S = 41/2$ ground state. Since the *J* values are very small, numerous states often lie within a few wave numbers in energy, causing difficulties in correctly estimating the ground state *S* values. The small estimated entropy for complex **74** has been ascribed to the antiferromagnetic J_5 Fe^{III}–Gd^{III} interaction (-0.6 cm^{-1}, see Fig. 13).[81]

Other polynuclear examples studied include the $[Gd^{III}_9Cu^{II}_8]$ complex $[Gd^{III}_9Cu^{II}_8(NO_3)_2\text{-}(OH)_{10}(L^3)_4(OAc)_{18}(H_2O)_4(NO_3)_2(OH)_3]$[75] (**75**) (here, L^3 = Schiff base ligand; see ref. 75 for details). In another attempt, calculations were carried out on the $[Gd^{III}_6Cu^{II}_{12}\text{-}(OH)_{12}(L^3)_6(NO_3)_7\text{-}(OAc)_3(H_2O)_{12}](OH)_8$ (**76**)[75] (here, L^3 = Schiff base ligand; see ref. 75 for details) wheel-like structure (see Fig. 14a and b). From both these studies, the following conclusions can be drawn: (a) ferromagnetic exchange for doubly O–R bridging ligands (singly bridged); (b) one O–R and one carboxylato bridge led to antiferromagnetic coupling (double bridging); (c) two O–R bridges and one carboxylato bridge (triply bridged) correspond to an antiferromagnetic exchange interaction. This clearly indicates the predominant role of the Cu–O–Gd–O angle in regulating the exchange parameters. Recently, our group has attempted entropy calculations in {Cu^{II}–Gd^{III}} polynuclear complexes. We have designed and evaluated six- and four-exchange pathways between Cu^{II} and Gd^{III} ions in $\{Cu_5Gd_4\}$ clusters $[Cu^{II}_5Gd^{III}_4O_2(OMe)_4(teaH)_4(O_2CC\text{-}(CH_3)_3)_2(NO_3)_4]$ (**77**) {teaH = triethanolamine} and $[Cu_5Gd_2(OH)_4(Br)_2\text{-}(H_2L)_2(H_3L)_2\text{-}(NO_3)_2(OH_2)_4]$ (**78**) [H_4L = (2-{[(2-hydroxy-3-methoxyphenyl)-methylene]amino}-2-(hydroxymethyl)-1,3-propanediol)]; (finally forms H_2L and H_3L) respectively (see Fig. 14c and d). The calculated DFT *J* values show the existence of moderate as well as stronger antiferromagnetic interactions between Cu^{II} ions *via* μ_5-oxo, μ_2-alcoholic and μ_5-oxo bridges, respectively. The difference in the magnitude of the exchange is rationalized based on the Cu–O–Cu angles. As a whole, the strong antiferromagnetic interaction between Cu^{II} ions tends to favour the $S = 31/2$ state in $\{Cu_5Gd_4\}$ clusters. The computed *J* values are able to reproduce the experimental curves nicely, giving us confidence in our employed methodology.[82] DFT calculations have been undertaken by us recently on {$Gd^{III}_4Co^{II}$} $[Gd^{III}_4Co^{II}\text{-}(\mu_3\text{-}O)(dipp)_6(DMSO)_6(MeOH)_2]$ (**79**) {$dippH_2$ = 2,6-di-iso-propylphenylphosphate} clusters to estimate two types of {Gd–Gd} and {Gd–Co} exchanges; the estimated *J*s are in the range of 10^{-2} to 10^{-3} cm^{-1}, resulting in large MCE values for this cluster.[83]

In this work, and also in other studies, some of the {Cu–Gd} interactions are antiferromagnetic; this suggests the relevance of magneto-structural correlations where antiferromagnetic coupling is predicted at acute angles. Although these angles are difficult to achieve in dinuclear frameworks, very acute angles and large structural distortions in the dihedral angles are very common in polynuclear complexes.

To gain deeper insights into the dependence of *J* on the angles/dihedral angles, we have undertaken comparative analysis of several {3d-Gd^{III}} complexes with varying 3d metal ions (see Fig. 12b and c and Table 2). Our analysis revealed the strongest exchange for the {Cu–Gd} pair, reproducing the literature reports. The exchange value varies as $J_{Cu^{II}\text{–}Gd^{III}} > J_{Ni^{II}\text{–}Gd^{III}} > J_{Fe^{II}\text{–}Gd^{III}} > J_{Mn^{II}\text{–}Gd^{III}} > J_{Cr^{III}\text{–}Gd^{III}}$ if all the structural parameters are maintained (with a few exceptions).[70] With increasing 3d-O–Gd angle for all the 3d ions, the interaction progressively becomes more ferromagnetic in nature (see Fig. 12b). However,

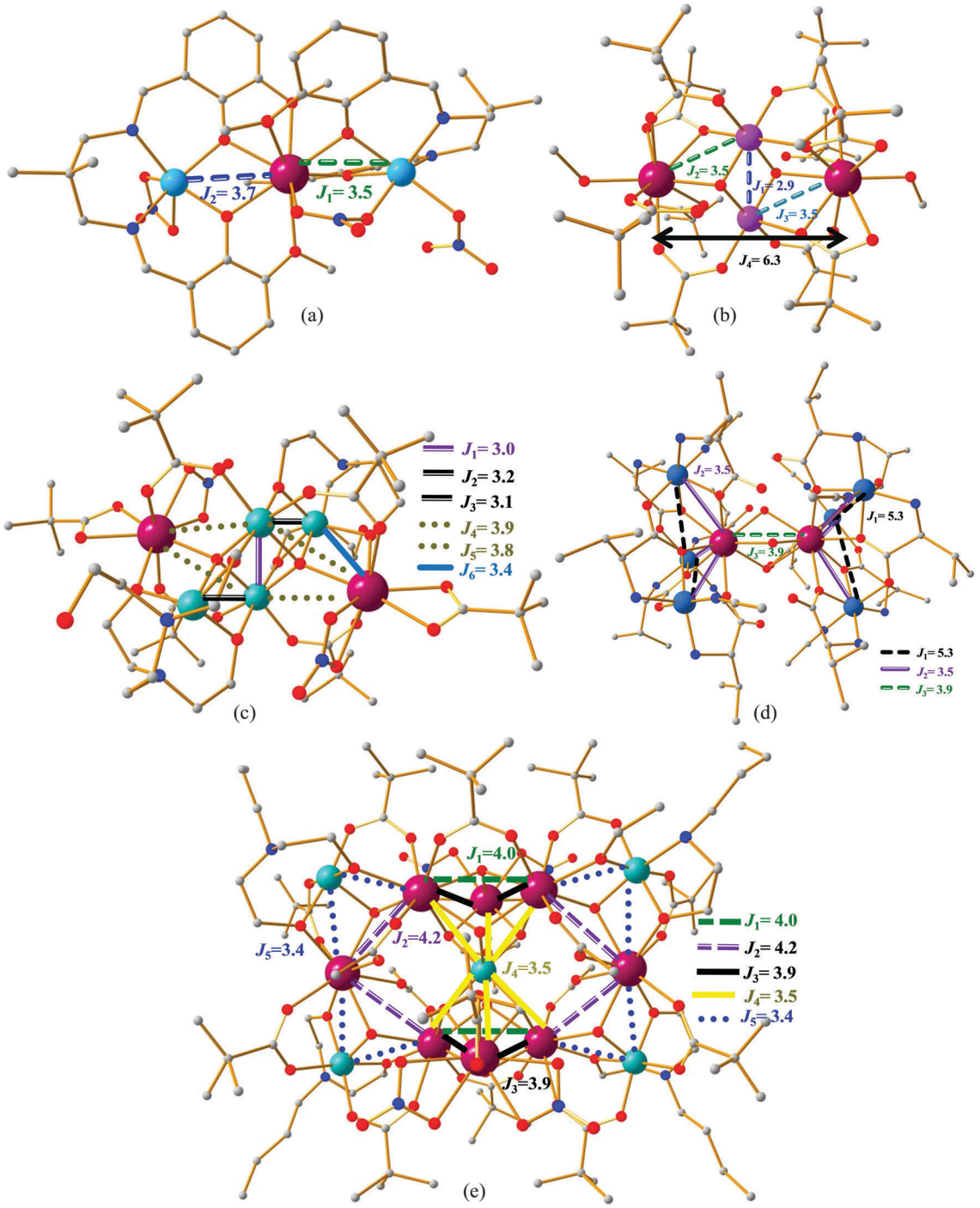

Fig. 13 Crystal structures of complexes (a) **70**, (b) **71**, (c) **72**, (d) **73**, and (e) **74** showing possible exchange interactions within them. Color scheme: Gd^{III}: brown, Mn^{II}: sky, Mn^{III}: pink, Fe^{III}: bluish green, Ni^{II}: sky blue, O: red, N: blue, C: grey. In all the complexes, H-atoms were omitted for clarity. The structures also contain the numbers of the *J*s employed in the calculations, along with the computed J_{DFT} values. {Note: all the *J* values given are in cm^{-1}}.

upon increasing the 3d-O–Gd–O dihedral angle, the interaction becomes more antiferromagnetic in nature irrespective of the nature of the 3d ion (see Fig. 12c). This proves the presence of a linear correlation between the 3d-O–Gd angle/3d-O–Gd–O dihedral angle and the magnitude of *J*. However, the effects of the angle and the dihedral angle on the *J* values are inversely correlated to each other. This correlation entails the need for ligand field design with larger bending angles and smaller torsional angles in {3d-Gd} moieties in order to obtain stronger *J* values, enabling new predictions for novel targeted syntheses. Here, as well, irrespective of the nature of the 3d ion, next nearest neighbour interaction is proved to be an intrinsically important parameter of the magnetic exchange. The combination of structural parameters, *i.e.* angle, dihedral angle, hinge angle and

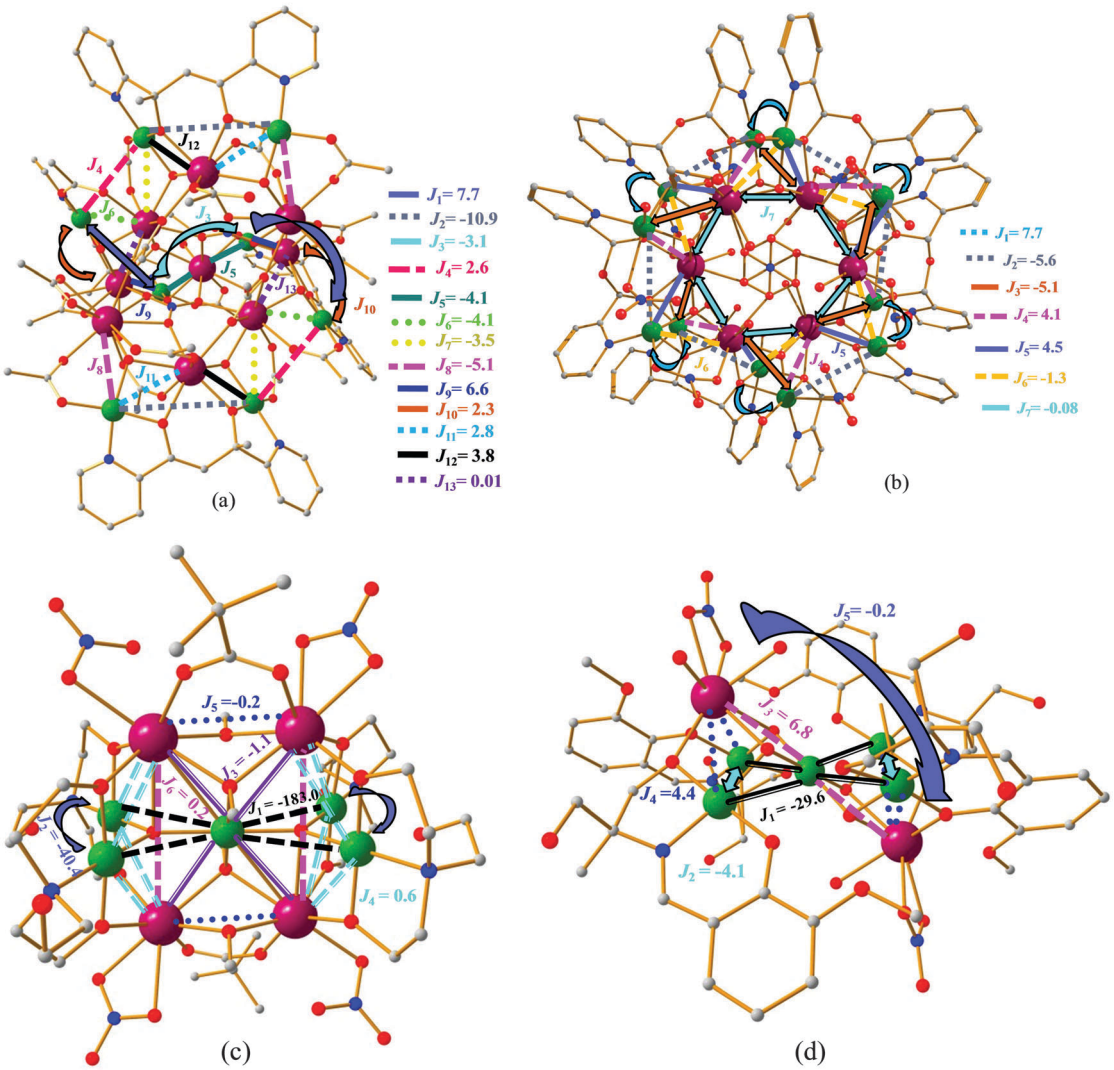

Fig. 14 Crystal structures of complexes (a) **75**, (b) **76**, (c) **77**, and (d) **78** showing possible exchange interactions within them. {Note: all the *J* values given are in cm^{-1}}.

several others, are imperative to fine tune the magnitude of *J* for all {3d-Gd} complexes. We have also demonstrated a generic mechanism for exchange in {3d-Gd} complexes, with a prominent role of the Gd^{III} empty 5d orbitals. Additionally, the nature of the bridging ligand, the type of coordination mode, and the ligand binding together play crucial roles in dictating the sign and strength of *J* values in {3d-Gd} clusters.

3.1.4 Modelling isotropic *J* in 4f-4f and 4f-2p SMMs. In this section, we aim to cover magnetic exchange coupling computed for the {Gd–Gd} pair. We have performed extensive calculations[84] on a dinuclear $\{Gd^{III}–Gd^{III}\}$ complex $\{Gd^{III}(OAc)_3(H_2O)_2\}_2$ (**80**)[84] with the aim to assess a suitable methodology to calculate *J* values and to investigate the underlying mechanism of exchange. In this regard, several pure, hybrid, and meta-hybrid functionals including relativistic effects of Gd^{III} *via* ECP, ZORA and DKH have been performed. Our rigorous methodology assessment predicted a combined SARC-ZORA (to incorporate the relativistic effect of Gd^{III} ion) methodology with the B3LYP functional to provide superior reproduction of numerical estimates of *J*. Additionally, extensive magneto-structural correlations were performed on several structural parameters, and the calculations reiterated the importance of the Gd–O–Gd angle in switching the coupling from ferromagnetic to antiferromagnetic interaction (see Fig. 15a). DFT calculations have been undertaken by us recently on $\{Gd_5^{III}\}$ $[Gd_5^{III}(\mu_3\text{-}OH)(NO_3)_2(dipp)_6(MeOH)_7(H_2O)_4]$ (**81**) clusters to estimate two types of {Gd–Gd} interactions. These interactions are estimated to be -1.3×10^{-3} cm^{-1} and 1.0×10^{-4} cm^{-1}, resulting in large MCE values for this cluster. In this cluster, the average Gd–O–Gd angles are found to be 108.8° to 110.9°; very weak *J* values are predicted, as these values are at the boundary of the crossover from ferro- to antiferromagnetic coupling.[83]

Estimation of magnetic coupling in {Gd–Gd} complexes has also been previously attempted. Spin DFT (SDFT) calculations were carried out on {Gd–Gd} $([\{[(Me_3Si)_2N]_2(thf)Gd\}_2(N_2)])$[85] (**82**) complexes in accordance with experiments. Using a

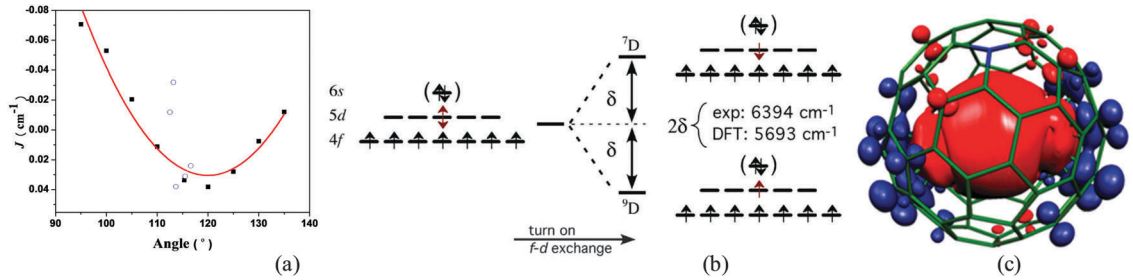

Fig. 15 (a) Developed magneto-structural correlation on **80** upon varying the Gd^{III}–O–Gd^{III} angle. Reprinted with permission from ref. 84. Copyright 2004 Wiley-VCH. (b) Electronic splitting of the Gd^{III} atom as a function of 4f-5d exchange perturbation. Reprinted with permission from ref. 85. Copyright 2006 American Chemical Society. (c) DFT-computed spin density plot for the optimised structure of complex **85**. Reproduced from ref. 93 with permission from the Royal Society of Chemistry.

similar methodology, calculations were carried out on several Gd^{III} dinuclear complexes, and the computed results are in line with the experiments. The study highlights the importance of the $4f^7$-5d exchange in the mechanism of magnetic coupling (see Fig. 15b).[85] Employing a similar methodology, calculations were also carried out for {3d-Gd_6} complexes.[86]

Although a significant amount of work has been devoted for understanding magnetic coupling in {3d-Gd} clusters, the very large J values, on the order of a few hundred wavenumber, required to substantially quench the QTM effects are not found in this class of complexes. Other viable options to promote this strong exchange include incorporation of other paramagnetic species, such as radical ligands. This approach resulted in record high magnetic coupling in lanthanide chemistry.[87] As with the developments on {4f-2p} complexes, a theoretical study[88] aiming to understand the nature of magnetic coupling in this pair has also been undertaken. Our analysis on the N_2^{3-} radical bridged Gd^{III} dinuclear complex $[\{[(Me_3Si)_2N]_2Gd(THF)\}_2(\mu\text{-}\eta^2\text{:}\eta^2\text{-}N_2)]^-$ (**83**) predicts strong antiferromagnetic Gd^{III}-rad (1,2) interaction (-47.4 cm^{-1}) and weak antiferromagnetic Gd^{III}–Gd^{III} (1,3) interaction (-1.0 cm^{-1}).[89] The estimated exchange coupling is in agreement with the experimental results (J_{exp}: Gd-rad -54 cm^{-1}). Unlike in {3d-Gd} clusters, where the exchange interactions are routed through a bridge (super-exchange), here the radicals are directly bonded to the Gd^{III} ions, leading to an efficient overlap. NBO analysis on this complex predicts weak π_{py}^*-$\delta(d_{xy})$, strong π_{py}^*-4f interaction (supported by overlap integral analysis) and a small increase in the occupation of the 5d orbitals, leading to net antiferromagnetic coupling for the Gd-radical pair. Additionally, the magneto-structural correlations predicted N–N, Gd–N–Gd, N–Gd–N–Gd and the non-planarity of the {Gd_2N_2} unit to be proactive in regulating the magnitude of exchange. A recent experimental report where potassium ions are incorporated in the {$Gd_2N_2^{3-}$} moiety reveals deviation in the Gd–N–N–Gd dihedral; for this new structure, similar Gd-radical interactions but stronger Gd–Gd interactions are observed, as predicted.[90]

Persistent interest in the {4f-2p}[91] moiety triggered us to continue our analysis of these classes of complexes. Several such dinuclear {4f-radical} complexes have been reported, comprising versatile substituted nitronyl-nitroxide ligands with J values ranging from -54 cm^{-1} to $+12.1$ cm^{-1}. Our vigorous method of assessment resulted in the following trend of enhanced accuracy in predicting J values in comparison with experiments: B(40HF)LYP < BHandHLYP < TPSSH < Pw91 < PBE < BP86 < OLYP < BLYP < PBE0 < X3LYP < B3LYP < B2PLYP. Computations show B2PLYP to be superior to B3LYP in predicting J values. Here, contrary to our earlier statement, relativistically corrected ECP has been found to yield better results compared to all electron SARC-ZORA/DKH methods. Moreover, the Gd–O–N–C dihedral angle is found to play a decisive role in determining the sign and strength of exchange values compared to other structural parameters.[92]

Moreover, we have very recently attempted calculations on the endohedral-metallofullerene based complexes Gd_2@666-($C_{79}N$) (**84**) and Gd_2@665-($C_{79}N$) (**85**) (see Fig. 15c for spin density). The exchange between $C_{79}N$ radical fullerene and Gd^{III} is found to be exceptionally strong (+400 and +378 cm^{-1} for complexes **84** and **85**, respectively), offering a viable way to obtain novel SMMs.[93]

3.2 Double exchange

"Double exchange" was first been proposed by Zener[197] to be a mechanism incorporating electron spin interaction that is characteristically different from the general notion of exchange; this provides a rationale for the magnetoresistive effects (ferromagnetic ordering temperature T_c), ferromagnetism in doped magnetic semiconductors and ferromagnetic–paramagnetic phase transitions. This is necessarily seen in transition metal compounds possessing two or more metal sites of varying non-integer oxidation numbers, known as mixed valence complexes.[213] In mixed valence complexes, double exchange (in addition to Heisenberg exchange) is generated due to the presence of an extra additional electron, which aligns the localized magnetic moments. As this additional electron maintains its spin during transfer between the metal sites, double exchange always favours the same spin orientation. Hence, double exchange plays a vital role in synthesizing molecules with high-spin ground states.[94] For mixed valence (AB) dimeric systems, Girerd *et al.*[196] have established a spin Hamiltonian of the following form:

$$\hat{H} = (-J_{AB}S_A\cdot S_B + E_A)O_A + (-J_{AB}S_A\cdot S_B + E_B)O_B + BT_{AB} \quad (5)$$

where E_A and E_B represent the energies of the dimer when the excess electron lies on the A and B sites of the dimer, respectively. S_A and S_B imply spins on the A and B centres, respectively.

Superscripts have been added, as the numerical values of S_A and S_B rely on the position of the extra electron. The O_A and O_B operators signify occupation operators. B = the double exchange parameter. T_{AB} represents the transfer operator which converts $|A\rangle$ into $|B\rangle$ (and *vice versa*) and generates the $(S_{AB} + \frac{1}{2})$ factor from the dimer spin S_{AB}. BT_{AB} represents the spin-dependent delocalization operator, which is proportional to the hopping integral between the two atom centred orbitals.

$$B = \beta/(2S_0 + 1) \quad (6)$$

B = electron transfer integral (hopping integral) between magnetic orbitals occupied by transferable electrons. S_0 = spin of the metal centers without extra electrons.

$$\beta_{\text{eff}} = \frac{\beta(2S+1)}{2(2S_0+1)} \quad \{\beta_{\text{eff}} = \text{effective transfer integral}\} \quad (7)$$

It is worth noting that double exchange interactions split each spin state into two levels possessing in-phase (gerade) and out-of-phase (ungerade) combinations. Moreover, stabilization within a dimer is proportional to $S + 1/2$. Hence, the double exchange parameter (B) in a mixed valence compound stabilizes the high spin ground state of maximum spin ($S = S_{max}$), and its magnitude is much larger than the J values. This facilitates the procurement of an isolated ground state (in addition to obtaining a large S value); thus, the B parameter is beneficial for obtaining novel SMMs. The computational approach to estimate the B parameter using the Hamiltonian described above is discussed in detail elsewhere.[95] Here, we intend to discuss various attempts which have been made to obtain this parameter.

Computing double exchange in 3d-based mixed-valence complexes. In addition to obtaining double exchange parameters by solving the aforementioned equations, they can also be derived from *ab initio* calculations {CASCI (complete active space configuration interaction) and DDCI (difference dedicated configuration interaction)} by analysing energy levels, as proposed by Guihery *et al.*[198] Furthermore, electronic structural parameters relevant to double exchange can also be extracted using DFT calculations.[199] Transfer operators can be extracted from DFT energies of the two monodeterminantal spin states of the highest multiplicity. Additionally, calculations of independent DFT single determinant energies (solutions) are imperative to estimate amplitudes of interactions for the generalized Hamiltonian, hopping integral, electron–electron repulsion and on-site exchange integral values.[199] Eventually, double exchange interaction as well as the spectrum can be evaluated from analytical correlations between the aforementioned interactions and those of the double-exchange model.[199] It is noted that the double exchange mechanism induces the formation of the spin polaron of the spin between ferromagnetically oriented neighbouring spin centres.[200] Furthermore, polaron formation is an inevitable generic phenomenon driven by spin disorder scattering; it plays a vital role in the magnetic transition, magneto-transport and magneto-resistive effects of the paramagnetic state. Incorporation of the spin polaron in the double exchange model is found to improve the predictions with respect to experiments and results in several interesting phenomena (increase of T_c with enhancement of the electron/hole density, increase of T_c against the external magnetic field).[200] The mixed valence compounds (mostly class II and III) exhibit important coupling of electron movement with geometrical distortions, and this subsequently affects the degree of localization of the extra electron. This was first proposed by Piepho, Krausz and Schatz through their quantum-mechanical vibronic simplified model (PKS model) to illustrate intervalence charge transfer absorption bands in mixed valence systems.[201a] Double exchange, in conjunction with vibronic interaction, assists in analysing electron delocalization patterns and spin states in the Robin and Day classification of mixed valence complexes. In the PKS model, the donor and acceptor each possess a single orbital, which accounts for the coupling between the extra electron and the vibrations of the ligand environment of donor/acceptor centres.[201a] The deficit of considering the breathing vibration in the PKS model was compensated by the improved effective Hamiltonian model approach proposed by Borshch and co-workers.[196c,201b] This arose from the concept that vibronic coupling and electron transfer parameters are not independent and that electron transfer necessarily relies on displacement of the bridging ligand.[196c,201b] Considering that the significant impact of vibronic PKS vibrations on the indirect electron transfer matrix is driven by the bridging ligands, a further extension of the simple PKS model was constructed.[201c] This is viable for finding stability criteria with respect to the PKS vibrations of the mixed valence clusters of the Robin and Day classification.[201c]

The initial attempt to compute various SH parameters of mixed-valence systems were carried out by Bencini[95a] *et al.* using the VWN-Stoll functional on the Fe^{II}–Fe^{III} mixed valence compound $[Fe_2(OH)_3(tmtacn)_2]^{2+}$ (**86**) (tmtacn = 1,4,7-trimethyl-1,4,7-triazacyclononane) with the aim to develop a consolidated characterization procedure for mixed valence complexes. Computations predict a large ferromagnetic interaction (+274 cm^{-1}) and, consequently, strong double exchange (1366 cm^{-1}) for this Fe-mixed valence complex. Changes in the Fe–Fe distances were found to have an impact on the magnitude of J and B.[95b] The displacement of the bridging –OH ligands towards one of the Fe sites and relaxing of the remaining part of the molecule paves the way towards maintaining the minimum energy path along the potential surface. These calculations were carried out with varying Fe–Fe[96] distances for the Fe^{II}–Fe^{III} complex, which was classified as a class III mixed valence compound (metal–metal charge transfer transition). DFT calculations (ADF suite) were carried out on mixed valence Mn^{II}–Mn^{III} and Mn^{III}–Mn^{IV} complexes $[Mn_2O_2(NH_3)_8]^{n+}$ (**87**) employing Xα-VWN-Stoll approximation on the geometry of minimum energy. The transfer integral parameter β for this specific complex was computed in order to subsequently evaluate the double exchange parameter (B). The computed exchange in these class-II compounds was found to be FM in nature between the Mn^{II}–Mn^{III} and Mn^{III}–Mn^{IV} ions.[95b]

Using a combination of DFT and TD-DFT methods, an attempt has been made to thoroughly characterize a $\{V^{II}$–$V^{III}\}$ $[(PY_5Me_2)_2V_2(m\text{-}5,6\text{-dimethylbenzimidazolate})]^{4+}$ (**88**) mixed valence complex. Switching of AFM to FM exchange upon oxidation of

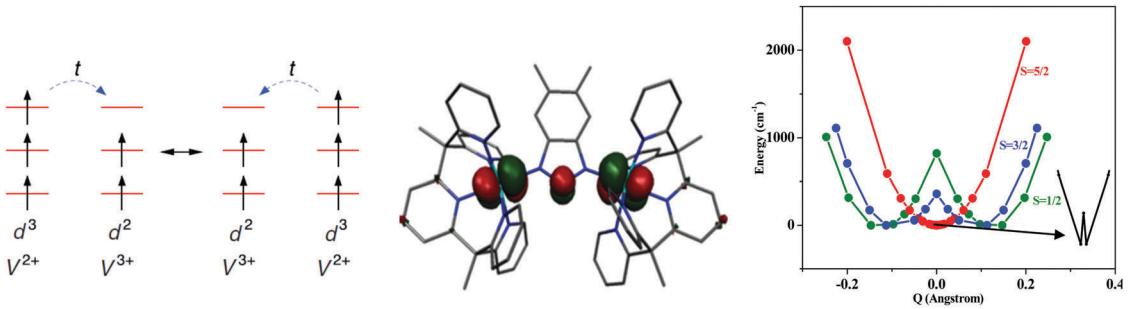

Fig. 16 (a) Generic orbital scheme for a mixed valence $\{d^2–d^3\}$ $\{V^{II}–V^{III}\}$ pair representing spin-dependent electron transfer (double exchange). Reprinted with permission from ref. 97. Copyright 2012 American Physical Society. (b) DFT-computed spin density plots for the LUMO of high spin states showing equal d_{xz} contributions on both the V ions. The iso-density surface represented corresponds to a value of 0.03 Bohr^3 e^{-1}. The green and red colours indicate positive and negative densities. Reproduced from ref. 98 with permission from the Royal Society of Chemistry. (c) DFT-computed potential energy surface for different spin states of complex **88**. Reproduced from ref. 98 with permission from the Royal Society of Chemistry.

the complex is in accordance with our earlier statement that the presence of double exchange in a mixed valence complex (see Fig. 16a[97]) tends to stabilize the highest ground spin state. Structural optimization and CASSCF calculations predicted $S = 5/2$ as the ground state, reproducing the experimental observation. Spin density distribution implies complete delocalization of the electron and equal d_{xz} orbital contributions on both the V^{II}/V^{III} ions[98] (see Fig. 16b). Using the DFT and TD-DFT combination, the isotropic J is estimated to be -14 cm^{-1}, while B is computed to be 666 cm^{-1} (see Fig. 16c for the developed PES). These estimates are in accord with experimental values.[94,99] Calculations suggest complex **88** as an intermediate of the class II and class III types.[94] More accurate Density Matrix Renormalization Group[100] (DMRG, BLOCK code) calculations have been performed on $[Fe_2S_2(SCH_3)_4]^{2-/3-}$ (**89**) and $[Fe_2S_2(SCH_3)_4]^{2-}$ (**90**) complexes by Neese *et al.* These calculations demonstrated that the conventional Heisenberg double exchange model underestimates the number of low-lying states, and this can be ascribed to the absence of very important Fe d–d transitions. This work essentially necessitates the accessibility of low-lying states for its implication in multiple electronic states and the non-adiabaticity of the reactions.

Although the B parameter is a boon for SMMs, there are several challenges in obtaining a complete delocalization of the unpaired spins in polynuclear complexes. For these reasons, there are no SMMs reported to date which demonstrate operational double-exchange phenomena. This is also correlated to the very small number of experimental and theoretical studies in this direction. A synergetic experimental and theoretical study focusing on several novel mixed valance systems is needed to effectively utilize B in the design of novel SMMs.

3.3 Anisotropic exchange interaction

Anisotropic exchange[101] is basically a synergistic effect of spin–orbit coupling perturbations and coupling between the ground state of an ion and the excited states of another ion.[1d] In complexes with orbitally nondegenerate ground states, isotropic exchange prevails and a simple Heisenberg model can be used to represent the "spin-only" exchange parameter. Contrarily, for complexes with orbitally degenerate ground states where the angular momentum is not suppressed by low-symmetry ligand fields, "spin-only" analysis of the exchange (the conventional Heisenberg–Dirac–Van-Vleck model) fails to sufficiently provide the theory behind the magnetic data. This implies the need for a kinetic exchange Hamiltonian (an orbitally dependent exchange Hamiltonian) which can be represented by orbital matrices, variables and spin operators.[102] The Hamiltonian corresponding to the anisotropic exchange can be described as follows:

$$\hat{H}_{ex} = -J_x\hat{S}_{1,x}\hat{S}_{2,x} - J_y\hat{S}_{1,y}\hat{S}_{2,y} - J_z\hat{S}_{1,z}\hat{S}_{2,z} \quad (8)$$

Four cases based on the above eqn (8) may arise: (i) $J_x = J_y = J_z$; the standard Heisenberg model Hamiltonian for magnetic exchange and the resulting exchange is isotropic in nature, and its spin is three dimensional; (ii) $J_x = J_y = 0$; this is known as the Ising model for magnetic exchange. This defines an anisotropic spin exchange model where the spins align themselves either up or down along the z axis, but the xy plane is spin free, *i.e.* one dimensional spin; (iii) $J_z = 0$, termed the X–Y model for magnetic coupling; as in case (ii), this form of exchange is also anisotropic; (iv) $J_x = J_y = J_z \neq 0$ which gives rise to a three component anisotropic exchange model. The orbitally dependent exchange is considered to be the salient feature of the unquenched orbital angular momentum in complexes with orbitally-degenerate ions manifesting strong magnetic anisotropy; it may dramatically enhance the barrier for magnetization reorientation. This induces prominent exchange anisotropy[103,104] in complexes with orbitally degenerate ions. Moreover, the ligand field effect, spin–orbit coupling and Zeeman interaction must also be accounted for in these orbitally degenerate systems. The dependence of magnetic exchange on the spin population (arising from spin delocalization/polarization exerted on the ligand) of different symmetry orbitals has been noted earlier by Atanasov *et al.*[105] Additionally, in consideration of isotropic exchange coupling, incorporation of this orbital dependent[102] (anisotropic part) exchange is found to induce huge exchange anisotropy in the studied

complexes,[105] stressing its importance. Anisotropic exchange has been illustrated earlier by the potential exchange term, neglecting the kinetic exchange model and including spin orbit coupling through super-exchange.[106] The computational approach to extract anisotropic exchange is described in detail elsewhere;[104,107] here, we intend to discuss the results obtained through such calculations.

Pragmatic instances of computing orbitally-dependent anisotropic magnetic exchange. Although the computation of orbitally-dependent anisotropic magnetic exchange is rare, these parameters are often extracted by fitting various experimental data with a model Hamiltonian. Coupling 3d-ion to $[Mo^{III}(CN)_7]^{4-}$ pentagonal bipyramidal heptacyanometallate[104] was shown to trigger strong exchange anisotropy and a large magnetic exchange interaction, blocking temperature and energy barrier for magnetization reversal. Studies on extracting the anisotropic exchange for four complexes, $[Mn^{II}_2(H_2O)_5Mo^{III}(CN)_7]\cdot 4H_2O$ (**91**), $[Mn^{II}_2(H_2O)_5Mo^{III}(CN)_7]\cdot 4.75H_2O$ (**92**), $K_2[Mn^{II}_3(H_2O)_6Mo^{III}(CN)_7]$ (**93**), and $[N(CH_3)_4]_2[Mn^{II}(H_2O)]_3[Mo^{III}(CN)_7]_2$ (**94**) with similar core structures of $[Mo^{III}$–CN–$Mn^{II}]$ have been attempted. Analysis yields opposite signs for the two strongly anisotropic exchange interactions, *i.e.* $J_z > 0$ and $J_{xy} < 0$, arising from the orbital degeneracy and strong spin–orbit coupling of Mo^{III} ion. This prevents precise determination of the nature of exchange, ferro/antiferro, and exemplifies an extreme case of exchange anisotropy. These results by Mironov *et al.*[104] are reminiscent of previous studies on the Yb^{III}–Cr^{III} [107b] pair, which shows opposite signs ($J_{\parallel} = -5.2$ cm^{-1} and $J_{\perp} = +4.2$ cm^{-1}) of exchange interaction. It is notable that although the origins (spin–orbit coupling) of exchange anisotropy and the anisotropic ***g*** tensor are similar, no actual correlation exists between them. BS-DFT (ADF suite) in conjunction with VWN-PW91 was carried out on different sets of cyanometallate complexes with Cu^{II}–NC–M^{III} [M = Cr and low spin Mn, Fe] fragments.[105] Different occupations of t_{2g} orbitals (x, y and z) of low spin Fe^{III} lead to a T-type orbitally degenerate ground state, which is prone to be disturbed by J–T effects in the presence of spin–orbit coupling. Calculations reiterate the need to incorporate orbital dependent exchange contributions for reproducing experimental J values of ions with T-type (x, y and z) ground states. The extended ligand field DFT (LFDFT, ADF suite) method has been employed to gain insights into anisotropic magnetic (exchange) properties by merging local, single and two-centre magnetic anisotropy.[108] Calculations were carried out using spin-projected and spin-unprojected methods on a set of Fe^{III}–CN–M^{II} complexes $[(CN)_5Fe^{III}\text{-}CN\text{-}M^{II}(CN)(NH_3)_4]^{2-}$ [M = Cu (**95**), Ni (**96**)]. The T-type ground state of low-spin Fe(III) triggered the exploration of two different types of[108] exchange parameters, $J_x = J_y \equiv J(E)$ and $J_z \equiv J(B_2)$, for Fe^{III}–M^{II}, which depicts a C_{4v} pseudo-symmetry around each individual pair. This subsequently led to the calculation of symmetric and antisymmetric tensors for each pair representing magnetic anisotropy.[108] In order to validate the experimentally (TeraHz-EPR, INS) observed anisotropic exchange coupling in $[Mn^{III}_2(5\text{-Brsalen})_2(MeOH)_2M^{III}(CN)_6]^+$SMM {$M^{III}$ = Fe (**97**), Os (**98**), Ru (**99**)} {5-Brsalen = *N*,*N*′-ethylenebis(5-bromosalicylide-ne)iminate, see Fig. 17a}, calculations were performed on the full structure using DFT methods by our group.[109] In addition to DFT calculations, the CASSCF/RASSI-SO approach has also been employed to understand the nature of the determinants.[110] By generating various configurations using DFT calculations, various components of the three-axis anisotropic exchange were computed for complexes **97–99** (see Table 4 and Fig. 17b for spin density plots). Calculations performed on **99** yield ferromagnetic interaction along the *x*-direction while yielding antiferromagnetic interactions along the *y*- and *z*-direction. These estimates are consistent with experimental studies[110] (magnetic studies, INS and terra-hertz EPR) carried out to extract these SH parameters in these complexes. The methodology developed here has the potential to extract these intricate parameters using computational techniques.[109] Hence, our overall analysis suggests that orbitally dependent magnetic exchange is a vital parameter to increase the blocking temperature as well as the barrier height in order to gain improved SMM characteristics, unlike the conventional need for the single-ion uniaxial zero-field splitting parameter (see Fig. 17c).[111,112]

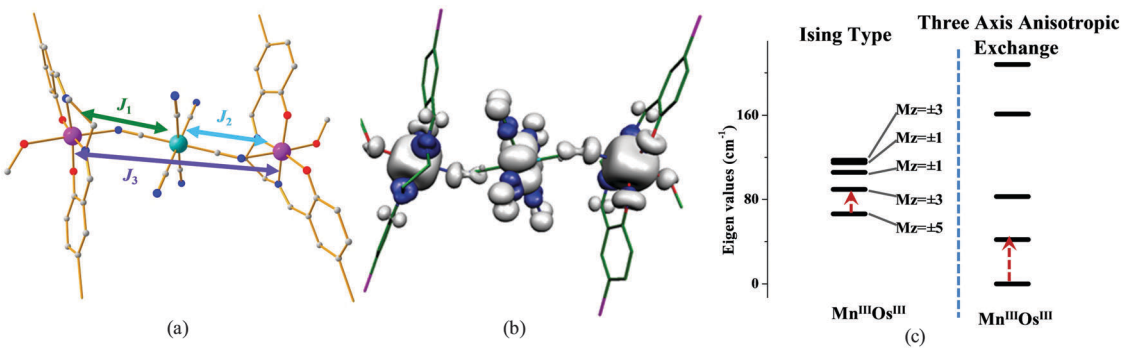

Fig. 17 (a) Crystal structure of complex **97** with possible exchange interactions. Adapted with permission from ref. 109. Copyright 2014 Wiley-VCH. (b) Spin density plot for complex **99** having $S = 9/2$ when the unpaired electron is in the d_{xy} orbital (with isovalue of 0.002 e^{-1} Bohr^{-3}). Reprinted with permission from ref. 109. Copyright 2014 Wiley-VCH. (c) MAGPACK computed spin energy levels for **98**; left corresponds to Ising type ferromagnetic interactions in **98** ($J_x = +25.5$ cm^{-1} and $J_y = J_z = 0$), while right indicates anisotropic interaction in **98** ($J_x = +25.5$ cm^{-1}, $J_y = -102$ cm^{-1}, $J_z = -22.5$ cm^{-1}). Reprinted with permission from ref. 109. Copyright 2014 Wiley-VCH.

Table 4 DFT computed magnetic exchange for complex **99** along with experimental values

Complex		J_{DFT} (cm^{-1})			J_{exp} (cm^{-1})		
		J_1	J_2	J_3	J_1	J_2	J_3
99	x	12.1 (7.5)	12.1 (7.5)	0.09	7.5	7.5	— —
	y	−6.9 (−10)	−6.9 (−10)	0.06	−9.0	−9.0	—
	z	−14.1 (−39)	−14.1 (−39)	0.27	−76.5	−76.5	—

3.4 Zero-field splitting parameter (*D*)

The zero-field splitting[113] tensor is a salient parameter of an effective spin Hamiltonian. It instigates splitting of the $2S + 1$ magnetic level[202] into $M_S = S, S - 1, \ldots, -S$ sublevels in the absence of the magnetic field, and it can be represented by the corresponding axial (D) and rhombic (E) parameters. The zfs parameter is prominent in transition metal complexes with unquenched orbital angular momentum in the pure electronic ground state. It is worth noting that stabilization of the lowest absolute value of $\pm M_S$ leads to a positive D value (no bistability), while a negative D value is noted for the highest $\pm M_S$ state stabilization. Hence, to design novel SMMs, large negative D and small E parameters must be achieved. Perturbation theory has predicted two contributions to the origin of zfs:[114] (i) direct spin–spin coupling (SS) – originates from electron–electron magnetic dipole–dipole interaction;[115] (ii) mixing of excited states into the ground state through the spin–orbit coupling effect (SOC). The SOC[116] term basically incorporates angular momentum into the ground state. It should be noted that second order SOC is a prevalent source of zfs in open-shell transition metal[114c] complexes, while the first order SSC contribution predominates in organic radicals.[117] The Hamiltonian corresponding to the D and E parameters is:

$$\hat{H}_{zfs} = D\left[\hat{S}_z^2 - \frac{1}{3}S(S+1)\right] + E\left(\hat{S}_z^2 - \hat{S}_y^2\right); \qquad (9)$$

Moreover, $D = D_{zz} - \frac{1}{2}(D_{xx} + D_{yy})$ and $E = \frac{1}{2}(D_{xx} - D_{yy})$, given that they obey $0 \leq E/D \leq 1/3$.

The sign of D is found to be positive for an oblate spin distribution and negative for a prolate spin distribution. Most importantly, the magnitudes of D and E are correlated to the strength of the dipolar interaction. Notably, a large rhombicity ($E/D = 1/3$) value results in uncertainty of the D values.[11b] The sign of the D value relies on D_{zz} and $(D_{xx} + D_{yy})/2$, where a comparatively larger D_{zz} term corresponds to a negative D value and the reverse case indicates a positive D value.[118] Electronic transition between the d-orbitals with the same $\pm M_l$ values, *i.e.* d_{xy} and $d_{x^2-y^2}$ ($M_l = \pm 2$) and d_{xz} and d_{yz} ($M_l = \pm 1$), contributes to the negative D parameter.[2c] It was determined that if the energy difference between the two orbitals is larger than 0.03 a.u., the D value should be small. Axial elongation is associated with small negative D values, while compression leads to positive D values.[118] Moreover, a large rhombic regime ($E/D = 0.16$–0.33) can be ascribed to large distortion around the metal coordination sphere.[188] Experimentally, electron paramagnetic resonance (EPR), HF-EPR, magnetic circular dichroism (MCD), ENDOR, ESEEM, ODMR and Mössbauer spectroscopy can be utilized to determine the magnitude of D and E. The illustration of these small magnitude D and E parameters in a coordination environment is challenging.[114c,119] On this note, quantum chemistry calculations play a vital role by (i) aiding the precise analysis and rationalization of the experimental EPR spectra; (ii) evaluating the correlation between the structural geometry and the D tensor; (iii) illustrating the controlling factors that contribute to the observed D tensor.[120] Both DFT and *ab initio* (CASSCF/PT2 (2nd order perturbation theory, effective Hamiltonian approach, EHA), NEVPT2, MRCI) methods are available to calculate the zfs parameters (D and E) of transition metal complexes. A detailed computational approach to the estimation of zfs been discussed elsewhere.[11a,121,122] Although DFT calculation of the zfs has previously been extensively used, it often fails to arrive at the correct sign or magnitude, as excited states of different multiplicities contribute significantly to the zfs parameters.[133] For these reasons, we intend to focus our attention here on the estimation of zfs parameters using *ab initio* methods. Also, the literature on the computation of zfs is very rich; here, we have considered only two prominent metal ions for the discussion: Ni^{II} and Co^{II}. This is essentially due to the fact that very large D values, as high as 500 cm^{-1}, are observed for Ni^{II} complexes, while several Co^{II} complexes exhibit SMM behaviour with large U_{eff} values. Other metal ions have so far failed to make the mark in either of the criteria mentioned. Additionally, an exhaustive review on this topic has already covered several other examples.[11c,122]

Pragmatic instances of computing zfs parameter in monomeric Ni^{II} metal complexes. Since the last decade, several Ni^{II} ($S = 1$) monomeric complexes have been reported that possess a large range of D values, from −500 cm^{-1} [123] ($E = 0.18$ cm^{-1}) to +200 cm^{-1}, and appealing magnetic properties. Despite the associated large D values, they do not demonstrate SMM behaviour, essentially due to the strong coupling between $M_S = \pm 1$ states.[124] D values of Ni^{II} based complexes vary upon changing the coordination environment, *i.e.* hexacoordinate octahedral[125] {−10 (E/D = 0.02) to +10 cm^{-1}}, pentacoordinate trigonal bipyramidal (−120 to −200 cm^{-1}, $E \sim 3$ to 0 cm^{-1}), tetrahedral (−8 to +11 cm^{-1}), and pentagonal bipyramidal (−13 cm^{-1}; $E = 1.2$ cm^{-1}).[126] The trigonal bipyramidal structures with small distortion are found to be the most suitable ones to design SMMs with large negative magnetic anisotropy. The Ni^{II} ion, with a d^8 configuration and trigonal bipyramidal geometry, has degenerate d_{xy} and $d_{x^2-y^2}$ orbitals and an unquenched orbital angular momentum. J–T distortion is expected to remove the degeneracy to place the first excited state at proximity to the ground state. This results in the observation of large negative D values for Ni^{II} complexes possessing trigonal bipyramidal geometry. Structural distortion will enhance the ground-excited state energy gap; subsequently, the D value will be reduced. Deformation of the equilateral triangle constituted by the equatorial ligands (α), bending of the axial metal–ligand bonds (β), and placing large ligands in the equatorial position and

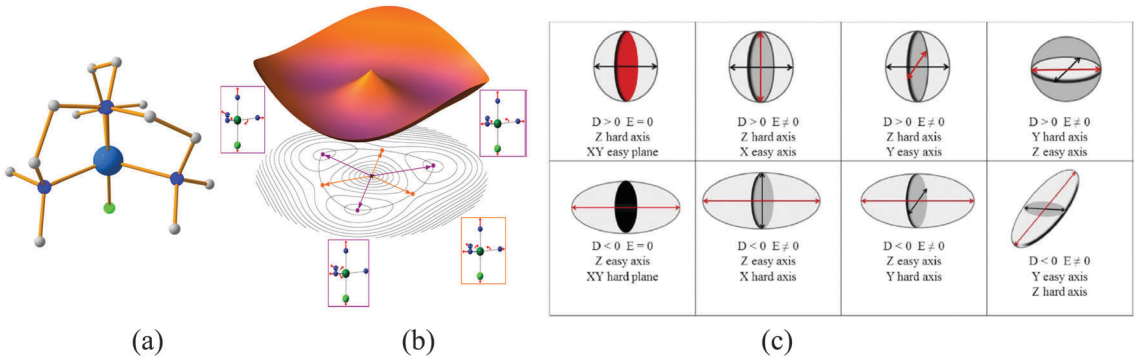

Fig. 18 (a) Crystal structure of complex **102** {Cl: green, remaining color scheme same as mentioned before}. (b) Schematic diagram explaining the moat around the J–T C_3 axis along with three symmetry-equivalent minima and transition states. Reprinted with permission from ref. 124. Copyright 2013 American Chemical Society. (c) Schematic of the conventions used to schematize the nature of magnetic anisotropy and to exhibit the magnetic axis frame of the *D* tensors. Prolate electron density (ellipsoid) implies axial anisotropy, while oblate electron density (ellipsoid) represents planar anisotropy (hard planes and hard axes are shown in black, easy planes and easy axes are represented by red; in the absence of rhombicity, only one axis has been shown). Although this has been demonstrated based on dinuclear complexes, the theory is also valid for mononuclear complexes. Reprinted with permission from ref. 134. Copyright 2014 American Chemical Society.[134]

bulky (rigid) ligands (always weak field ligands) in the axial positions enables minimization of the structural distortions (enhanced *D*). It is of high relevance to mention here that MRCI calculations on $[Ni(MDABCO)_2Cl_3]^+$ (**100**) ($MDABCO^+$ = 1-methyl-4-aza-1-azo-niabicyclo[2.2.2]octanium cation) give a predicted *D* value of ~ -535 cm^{-1} (E = 0.18 cm^{-1}); this has very recently been verified by HF-EPR studies.[123,127,123b] Other Ni^{II} monomeric complexes with trigonal bipyramidal geometry which also exhibit large *D* values include [Ni(Me$_6$tren)Br](Br) (tren = tris-(2-aminoethyl)amine) (**101**) and [Ni(Me$_6$tren)Cl](ClO_4) (**102**) (see Fig. 18a), where *D* values as high as -200 cm^{-1} (E = 1.6 cm^{-1})[124] have been observed. In both the above cases, the ground state degeneracy has been removed (J–T induced transition states), leading to a reduction in the first-order spin–orbit coupling. This is essentially because the J–T distortion is counterbalanced by the rigid organic ligand, which helps to maintain higher symmetry for the structure (see Fig. 18b and also 18c for correlation between nature of magnetic anisotropy and D-tensor axis frame[134]).[124] Other structures of Ni^{II} ion which are found to exhibit very large *D* values include the trigonal pyramidal structure, where a combined experimental and theoretical study undertaken on $K\{Ni(N[CH_2C\text{-}(O)NC(CH_3)_3]_3)\}$ (**103**) complex revealed a D_{cal} value of -244 cm^{-1} (E_{cal} = 1.9 cm^{-1}), while experiments yielded $D_{exp} = -200$ cm^{-1}. The large *D* value observed in these structures can be attributed to the d-orbital spitting in the J–T distorted trigonal pyramidal ligand environment, placing the excited state at close proximity to the ground state.[123b]

A CASSCF study undertaken by us to discover models possessing large *D* values is of relevance here (see Table 5), where *D* values in the range of +96 cm^{-1} to -300 cm^{-1} (E_{cal} = 0 cm^{-1}) were observed for several structures.[128] There are several reports on the estimation of zfs parameters in octahedral Ni^{II} complexes. *Ab initio* CASSCF/CASPT2/RASSI-SO (restricted active space state interaction-spin orbit)/atomic mean-field approximation (AMFI) has been employed successfully on a series of Ni^{II} mononuclear complexes with structures varying from compressed tetragonal systems to elongated ones in order to compute axial as well as rhombic zfs parameters. The test set includes 12 different complexes belonging to four categories: group I (homoleptic complexes; $\{NiN_6\}$), $[Ni(iz)_6]^{2+}$ (**104**) (see the transition responsible for the *D* value in Fig. 19a), group II (quasi octahedral; $\{NiN_4N_2'\}$), $[Ni(iqu)_4(NCS)_2]$ (**105**) group III (tetragonal; $\{NiN_4O_2\}$) $[Ni(pz)_4(ac)_2]$ (**106**) and group IV (rhombic systems; $\{NiN_2O_2O_2'\}$ $\{Ni(dmeiz)_2(fm)_2(H_2O)_2\}$ (**107**); iz = imidazole, iqu = isoquinoline, pz = pyrazole, dmeiz = 1,2-dimethylimidazole), and they also show *D* values in the range from -3.7 to +8.8 cm^{-1}; E/D_{cal} varies from 0.01 to 0.32.[128] Computations on $[Ni(HIM_2\text{-}Py)_2NO_3]^+$ (**108**) (HIM = imidazole) (D_{cal}/D_{exp} = $-10.6/-10.2$ cm^{-1} and E_{exp}/E_{cal} = 8.1/4.4) and [Ni(glycoligand)]$^{2+}$ (**109**) (D_{cal}/D_{exp} = 8.1/4.4 cm^{-1} and E_{exp}/E_{cal} = 0.6/0.8) complexes predict an influential role of *xy*-plane angular (along N–Ni–N) distortion on the zfs parameter. Moreover, these calculations also revealed a strong correlation between the geometry and σ-donor character of the ligand in modulating the zfs parameter.[129] Distortion within a structure leads to the observation of positive *D* values (+2.1 to +5.5 cm^{-1}, with E/D_{cal} varies from 0.00 to 0.33) as corroborated by *ab initio* calculations on a series of Ni^{II} complexes $[Ni(L^1{\cdot}H_2O)(OH_2)_2](PF_6)_2$ (**110**), $[Ni\text{-}(L^1{\cdot}H_2O)(O_2NO)]NO_3$ (**111**), $[Ni(L^1{\cdot}H_2O)(OOCCH_3)]PF_6$ (**112**), $[Ni(L^2{\cdot}H_2O)\text{-}NCMe](PF_6)_2$ (**113**), $[Ni(L^3{\cdot}H_2O)OH_2](PF_6)_2$ (**114**), and $[Ni(L^4{\cdot}H_2O)NCMe](PF_6)_2$ (**115**) {L^1 to L^4 are various substituted bispidine ligands}.[190] The contribution of the SOC constant and excited states to the *D* value were found to

Table 5 CASSCF + RASSI-SO computed *D* values for $[Ni(NH_3)_n]^{2+}$ models with n = 2 to 7. The *E* values are found to be zero for all the models

Coordination	Geometry	D_{cal} (cm^{-1})	E_{cal} (cm^{-1})	D_{exp} (cm^{-1})
2	Linear	−123.38	0	8.6 to 14.2
3	Trigonal planar	96.86	0	
4	Square planar	−293.70	0	32
4	Tetrahedral	−94.54	0	55
5	Trigonal bipyramidal	−278.27	0	−120 to −180
7	Pentagonal bipyramidal	−300.84	0	−13.9

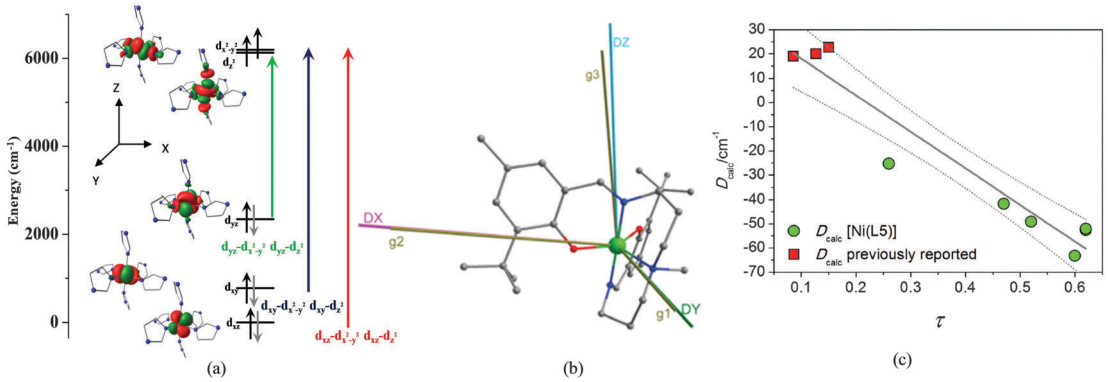

Fig. 19 (a) CASSCF-computed metal based d-orbitals with single excitations. The picture shows all possible spin-conserved excitations responsible for the zfs for the set tested. The green and red regions indicate positive and negative spin populations. The isodensity surface represented corresponds to a value of 0.015 e^- $Bohr^{-3}$. The orbitals and the energies are for the group-I complex of ref. 128. Reprinted with permission from ref. 128. Copyright 2014 Wiley-VCH. (b) CASSCF/NEVPT2-computed principal axis of the zfs tensor for **120**. Reproduced from ref. 135 with permission from the Royal Society of Chemistry. (c) Magneto-structural correlation developed between D and the geometrical parameter (τ) on complexes **120–125**. Reproduced from ref. 135 with permission from the Royal Society of Chemistry.

increase as we moved down group 17 in the periodic table, as revealed by the calculations on Tp*NiX complexes {Tp* = hydrotris(3,5-dimethylpyrazole)borate, X = Cl (**116**), Br (**117**), I (**118**)}. Notably, SOC constants of heavier halogens sometimes overcome the contribution from the metal centre. This leads to the enhancement of individual excited state contributions to the D parameter and consequently increases the negative D values to 3.9/3.8 (D_{cal}/D_{exp}), −11.4/−6.9, −22.8/−19.6 cm^{-1} for **116**, **117** and **118**, respectively. Moreover, metal–ligand covalency and low symmetry effects must be targeted simultaneously for precise determination of zfs parameters.[130] A meticulous literature survey and computations on nearly square pyramidal structures $[L^1Ni^{II}(6,6'\text{-diMe-2,2'-bipy})]^+$ (**119**) {HL^1 = 2-[(1*E*)-*N*-(2-amino-2-methylpropyl)ethanimidoyl]phenol} reveal large positive D values (CASSCF: D = 32.5 cm^{-1}, E = 9.7 cm^{-1}, E/D = 0.3; NEVPT2: D = 21.9 cm^{-1}, E = 7.0 cm^{-1}, E/D = 0.32).[131] Despite the similar number of coordinated donor ligand atoms, structural/electronic differences in the binding mode (*i.e.* *trans*-N_4N_2' and meriodoinal-N_3N_3') around the metal ion leads to different D values. Moreover, computations allow us to demarcate the σ-donating abilities of the N donor atoms.[132] In most cases, *ab initio* calculations are found to overestimate rhombic anisotropy.[131] Electronic transition between the d-orbitals with same $\pm M_l$ values[126] (d_{xy}–$d_{x^2-y^2}$ and d_{xz}–d_{yz}) contributes to negative D values, while the transition between different $\pm M_l$ values corresponds to positive D contributions. The negative D contribution can be enhanced by decreasing the energy gap between the ground and excited states by promoting coupling between them. Decreasing the energy gap between the three sets of orbitals, (d_{xz}, d_{yz}), (d_{xy}, $d_{x^2-y^2}$) and d_{z^2}, will facilitate the negative contribution of the D parameter.[126] However, this negative D contribution can be further increased by substituting the axial ligand with a better σ-donor in order to increase the energy of the d_{z^2} orbital or by inducing the π-donor ligand to promote the energy lowering of the (d_{xz}, d_{yz}) orbital set.[126,114c],133 Several other calculations have reaffirmed the role of the J–T axis and the role of organic ligands in dictating the zfs parameters.[124]

Calculations were carried out on six pentacoordinate Ni^{II} complexes (square pyramid and trigonal bipyramid) of the general formula [Ni(L^5)], (**120–125**) {H_2L^5 = salen type; (3-*tert*-butyl-2-hydroxy-5-methylbenzylidenyl)-1,7-diamino-4-methyl-4-azaheptan} but varying in the R-group substitution at the phenyl ring and the two N-atoms (see Fig. 19b for one of the crystal structures of complex **120**). *Ab initio* calculations on these series yielded a large negative range of D values, *i.e.* −25.3 (E/D = 0.17) to −63.2 (E/D < 0.07) cm^{-1}. This is again suggestive of an inverse relationship between negative axial zfs parameter and rhombicity. Moreover, trigonal bipyramidal geometry corresponds to negative D values, while square planar geometry is associated with positive D values. This was evidenced by the developed linear correlation between D and the geometrical parameters (τ, torsional angle, see Fig. 19c).[135] The magnitude of D is computed to be affected by the Ni–O and Ni–Se bond lengths, while the D values in S-containing complexes only rely on the Ni–O bond length. Elongation along the z and x/y axes results in negative and positive D contributions, respectively. Large E/D values (large rhombicity) cause issues in the accurate prediction of D values. Calculations on *trans*-[Ni^{II}{$(OPPh_2)(EPPh_2)N$}$_2$(sol)$_2$] (E = S, sol = DMF (**126**); E = Se, sol = DMF (**127**); E = S, sol = THF (**128**); E = Se; sol = THF (**129**)) (**126–129**) inferred large D values for S {3.1/2.6 and 9.2/6.4 cm^{-1}} D_{cal} (S/Se) DMF and THF substitution, *i.e.* **126**, **127**, **128** and **129** respectively, (E/D = 0.16 to 0.33) containing Ni^{II}-complexes as compared to the respective Se-coordinated compounds. Among CASSCF/MRDDCI2/QDPT, CASSCF/SORCI/QDPT and NEVPT2/QDPT, this last methodology gives the best numerical estimate of the zfs parameters for transition metal based complexes.[188] Completely axial high-spin (S = 1) tetrahedral Ni^{II} complexes, *i.e.* [Ni{$^iPr_2P(Se)NP(Se)^iPr_2$}$_2$] (**130**) show large negative D values (D_{cal}/D_{exp} = 47.9/45.4 cm^{-1}; E/D_{cal} = 0.05 *vs.* E/D_{exp} = 0.04), and the major contribution comes from the SOC interaction of Ni ion (the Se contribution is negligible).[136] A meticulous survey on the calculation of zfs parameters in Ni^{II} complexes clearly revealed that axial anisotropy parameters calculated with DFT are, in general, anomalously small for these complexes.[133]

Pragmatic instances of computing the zfs parameter in Co monomeric complexes. Several complexes comprising cobalt ions in their different oxidation states have been reported.[137] All of these possess a wide range of D values, *i.e.* Co^{I}: +42 cm^{-1} (E = 0.08);[138] Co^{II}: −112 (E = −1.1 cm^{-1}) to +55 cm^{-1} (E/D = 0.20 to 0.32),[139,140,203,208] Co^{III}: 35 to 145 cm^{-1}.[141,142] It is worth noting that Co^{II} complexes may exist in various symmetries, *i.e.* D_{2d}, C_{2v}, C_2 and C_1, complicating the analysis.[143] Moreover, the magnetic susceptibility data for Co^{II}-pseudotetrahedral compounds are insensitive to the sign of D.[143] Hence, gaining intuitive understanding of the magnetic properties of Co-based complexes using computational techniques is of prime interest. Multireference *ab initio* methods have been employed on the complex $[Co^{II}(PPh_3)Cl_2]$ (**131**), yielding zfs parameters which are in good agreement with experiments (D_{cal}/D_{exp} = −17.6/−14.8 cm^{-1}). Spin–orbit coupled (SOC) N-electron states play a proactive role compared to the respective spin–spin coupled states (SSC) towards determining the ground state zfs parameter. Incorporation of the spin–orbit mean field (SOMF) in CASSCF/QDPT calculations improved the accuracy of the computed results.[139b] Torsional angles (ω, R-S-Co^{II}-S) were found to play a decisive role (see Fig. 20a) in regulating the D values for pseudotetrahedral $[Co^{II}(SR)_4]$ complexes (**132**). In complexes with D_{2d} geometries, the $d_{x^2-y^2}$ to d_{xy} electronic transition contributes predominantly to the D parameter, resulting in negative D values. For a torsional angle variation of $45^\circ < \omega < 135^\circ$, the energy of the d_{xy} and d_{xz}/d_{yz} orbitals increases and decreases, respectively (see Fig. 20a); when $\omega < 45^\circ$ and $>135^\circ$, the orbital energy ordering is reversed.[144] There are also reports on the observation of a broad range of D (−8 to +11 cm^{-1}, E/D varies from 0.01 to 0.28) for flattened pseudo-tetrahedral $[Co^{II}L_2Cl_2]$ complexes (**133**) {here, L can be quinoline, benzimidazole, cytosine, imidazole, 2-aminopyrimidine}.[189] Very recently, detailed theoretical studies have been reported on pentacoordinated S = 1, Co^{III} complexes.[145] Contrary to our earlier statement for Ni^{II} on halide ligands, in Co^{III}-LX {X = Cl (**134**), Br (**135**), and I (**136**)} (L = 2,2′-(2,2′-bipyridine-6,6′-diyl)bis(1,1-diphenylethanethiolate)) structures, the D value decreases going down the column of group 17 in the periodic table (32, 22, and 16 cm^{-1} for **134**, **135** and **136**, respectively). This has been attributed to the favoured spin-conserved transitions between the comparatively close lying SOMOs–DOMOs (see Fig. 20b) in the CoCl analogue (as compared to CoBr/CoI).[145] This prominent halide ligand effect on the D values encouraged us to explore ligands of group 16. Recently, a synergetic approach between experiment and theory has been undertaken to switch the sign of zero-field splitting in a tetrahedral Co^{II} complex. Initially, a tetrahedral Co^{II} complex ($[Co^{II}(L)(X)_2(MeCN)]$; here, L = 2,3-diphenyl-1,2,3,4-tetrazolium-5-olate and X = Cl and Br) was synthesized, possessing D values of +15.6 and 11.1 cm^{-1} for the Cl and Br derivatives, respectively. CASSCF calculations performed by us on the X-ray structures yielded D_{cal} values of +20.35 and +18.5 cm^{-1} for the Cl and Br derivatives, respectively. In addition to rationalizing the observed positive zfs values based on the orbital energies and corresponding transitions (see Fig. 20c), a search for possible negative D values has been undertaken. In this regard, S and Se derivatives of the ligands have been modelled *in silico*, yielding D_{cal} values of −20.46 cm^{-1} and −20.52 cm^{-1} for the S and Se models, respectively. With this feedback, experimental groups synthesized the sulphur analogue, leading to a D_{exp} value of −11.30 cm^{-1}. Although there is a large deviation in the magnitude of the computed D parameters, calculations performed on the X-ray structure of the sulphur analogue bridged this gap (D_{cal} of −15.9 cm^{-1}). Most importantly, as predicted by the calculations, the incorporation of softer donor ligands was found to switch the sign of zero-field splitting, yielding a zero-field SIM with a larger U_{eff} barrier. The change in D (positive for the O analogue to negative for the S analogue) on moving down the column (adding more np valence orbitals) is ascribable to the favourable $d_{x^2-y^2}$ to d_{xy} transition of the S analogue contribution to the D_{zz} component, resulting in a large negative D value (see Fig. 20c).[146] This unequivocally underlines the role of theoretical calculations for targeted MNM synthesis beyond serendipity.

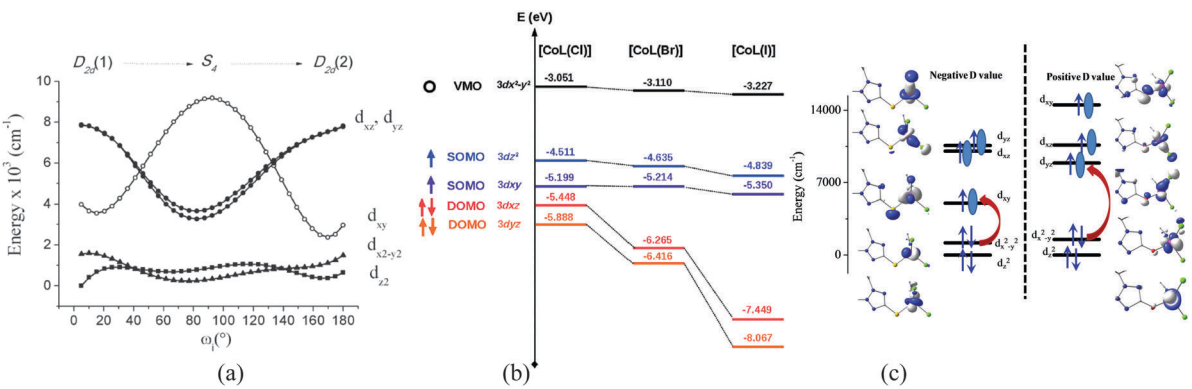

Fig. 20 (a) Energy splitting of d orbitals along the D_{2d} to S_4 to D_{2d} interconversion pathway, plotted as a function of the torsional angle ω, on complex **132**. Reprinted with permission from ref. 144. Copyright 2011 American Chemical Society. (b) Energy splitting of the five d-orbitals of three CoX complexes (**134**, **135** and **136**), where X is Cl, Br or I.[145] Reprinted with permission from ref. 145. Copyright 2016 Wiley-VCH. (c) DFT computed eigenvalue plots of the five d-orbitals for Co^{II} complexes with O (left) and S (right) ligands, respectively.[146] Reproduced from ref. 146 with permission from the Royal Society of Chemistry.

3.5 Exchange anisotropy

Exchange anisotropy[103,214] implies magnetic manifestation of an exchange interaction across the interface between two magnetically ordered materials. With the aim to probe the importance of exchange anisotropy and its relationship with single-ion anisotropy, *ab initio* calculations were performed on the $[Mn^{III}Cu^{II}Cl(5\text{-}Br\text{-}sap)_2(MeOH)]$ (**137**) dinuclear complex.[147] In the case of a strong exchange limit (where the isotropic exchange integral is larger than the anisotropic interactions), the zfs of the spin state S can be determined by vector coupling of two spins, S_{Mn} and S_{Cu}, which is given by the following equation:

$$D_s = d_{Mn}D_{Mn} + d_{MnCu}D_{MnCu} \quad (10)$$

where D_{Mn} is the single-ion anisotropy of Mn^{III} ion and D_{MnCu} is the anisotropy that arises due to exchange between these two ions: exchange anisotropy. The d coefficients are $d_{Mn} = 3/5$ and $d_{MnCu} = 1/5$.[2c] Similar SA-CASSCF (State Averaged-CASSCF) calculations on the overall dinuclear complex (10 electrons in 13 orbitals) results in high energy of the low-lying excited states, triggering a decrease in the overall global total ground-state anisotropy parameter {cluster anisotropy; $D_{5/2}$} for this complex. This large energy gap between the ground and excited states for the overall complex can be attributed to the computed strong ferromagnetic exchange coupling (+78 cm^{-1}) between the Mn^{III} and Cu^{II} ions. Using the above equation, the estimated exchange anisotropy was found to be −0.27 cm^{-1}. Hence, the global ($D_{5/2}$) anisotropy is being dictated by the combined effects of $D_{Mn^{III}}$ and D_{MnCu}. A decrease in the Mn–L_{axial} bond length (axial compression) to 2.1 Å results in an increase of the $D_{5/2}$ value, while further reduction of the bond length corresponds to the switching of the anisotropy to a positive value (see Fig. 21a).

In addition to computing the exchange anisotropy, magneto-structural correlations along the Bailer Twist directions were performed on complex **137**; a competing nature of $D_{Mn^{III}}$ and D_{MnCu} was detected, leading to a reduction of the $D_{5/2}$ values as the distortion (twisting) increases (see Fig. 21b). This antagonizing behaviour is attributed to the computed stronger magnetic exchange, asserting that strong exchange and strong anisotropy are unlikely to coexist in a SMM.[147] This is reminiscent of earlier work by Ruiz *et al.*,[113] which deters the coexistence of large spin and large magnetic anisotropy, consolidating our findings. Further examples of this kind must be studied in detail to obtain a clear picture of how exchange anisotropy influences the ground state anisotropy of polynuclear complexes.

The parameters extracted above are valid only for strong exchange limit scenarios; in weak exchange limit scenarios, the anisotropy tensors D_a, D_b and D_{ab} must be extracted directly.[192b] Most importantly, in general, the overall magnetic anisotropy can be deduced from the local anisotropy (except for complexes of weak-exchange regimes).[134] On this note, the calculation of local anisotropy tensors for each metallic ion in a weak exchange coupled dimeric Mn^{III} complex is notable.[216] DFT and multi-reference correlated *ab initio* calculations (uses Hamiltonian containing terms to depict local and inter-site interactions) yielded D_{Mn} as +4.29 cm^{-1} ($E_{Mn}/D_{Mn} = 0.19$). This is quite consistent with the value obtained from the fitting of the experimental EPR spectra (D_{Mn} = 4.50 cm^{-1}; $E_{Mn}/D_{Mn} = 0.07$).[192b,204,216]

3.6 *g* tensor magnetic anisotropy of lanthanide complexes

Zeeman splitting[148] splits each J-state into $2J + 1$ levels with concomitant M_J, corresponding to the values $-J, -J+1, \ldots, J-1, +J$. This invokes consideration of an effective g-value (g_J) instead of an isotropic electronic g factor, which can be expressed as:

$$g_J = 1 + \frac{J(J+1) + S(S+1) - L(L+1)}{2J(J+1)} \quad (11)$$

The g value becomes direction dependent due to the inherent orbital contribution of the magnetic field exerted on the electron. Hence, in an applied magnetic field, incorporating the "g tensor" following an effective Hamiltonian can be used:

$$\hat{H} = \mu_B \hat{B} g \hat{S} = \mu_B \begin{bmatrix} H_x & H_y & H_z \end{bmatrix} \begin{bmatrix} g_{xx} & g_{xy} & g_{xz} \\ g_{yx} & g_{yy} & g_{yz} \\ g_{zx} & g_{zy} & g_{zz} \end{bmatrix} \begin{bmatrix} \hat{S}_x \\ \hat{S}_y \\ \hat{S}_z \end{bmatrix} \quad (12)$$

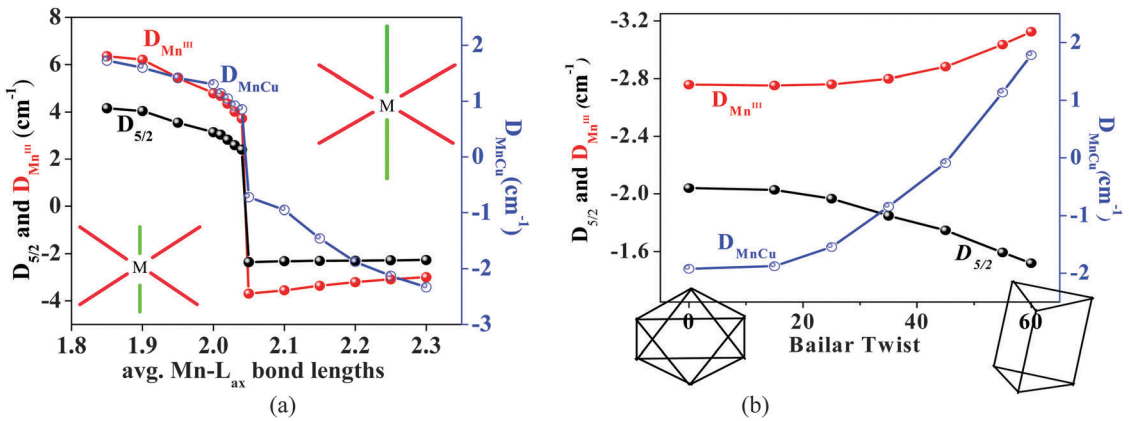

Fig. 21 (a) CASSCF-computed D values for complex **137** by varying M–L_{ax} bond lengths (J–T distortion). Reprinted with permission from ref. 147. Copyright 2014 Wiley-VCH. (b) CASSCF-computed D values as a function of the Bailar Twist. Reprinted with permission from ref. 147. Copyright 2014 Wiley-VCH.

The *g* tensor possesses information about the wave function of a molecule in its electronic ground state. The relative weight of the three main values of the *g* tensor anisotropy implies different types of magnetic anisotropy of the ground states.[149] Based on the directional dependence of *g*, they have been classified into three categories: isotropic ($g_{xx} = g_{yy} = g_{zz}$), axial ($g_{xx} = g_{yy} \neq g_{zz}$) and rhombic ($g_{xx} \neq g_{yy} \neq g_{zz}$). Moreover, two extreme cases of axiality may arise: (i) when $g_{zz} \ggg g_{xx} = g_{yy}$: Ising type anisotropy and (ii) $g_{xx} = g_{yy} \ggg g_{zz}$: substantial transverse components: transverse anisotropy.[150] Ising type anisotropy favours relaxation *via* the excited state and tends to enhance the barrier height for magnetization relaxation (U_{eff}) and fulfil the requirement to observe SMM behaviour. In these instances, considering the values of the two lowest principal *g* values as zero, magnetic properties in Ln^{III} ions can be estimated to an effective spin $S_{eff} = 1/2$ of the Ising type. It is noteworthy that the Ising model can be validated at low temperatures only when the ground states are populated.[149] Hence, it is clear that the nature of the ***g***-tensors dictates the relaxation of magnetization in SMMs, and their evaluation is done simultaneously through *ab initio* calculations. In some instances, our computed speculations for preferred stronger axial/weaker equatorial ligand fields in oblate ions has recently been verified by experimentalists.[215] Significant efforts have already been dedicated to understanding the magnetic anisotropy of lanthanide complexes using *ab initio* (CASSCF/RASSI-SO/SINGLE_ANISO or POLY_ANISO) calculations. In this article, we would like to briefly cover the studies on Dy^{III} and Er^{III} mononuclear complexes. The computational approach to the estimation of these parameters is detailed elsewhere.[151,205]

Modelling *g* tensors in Dy^{III} based monomeric complexes. Owing to their unquenched orbital angular momentum and inherent magnetic anisotropy, lanthanides are the most ubiquitous and suitable candidates for SMMs. This quality has led to the design of SMMs possessing one lanthanide spin carrier, and these are known to show large magnetization blockade barriers; they are termed Single Ion Magnets (SIMs).[14a] In SIMs,[152,153] the crystal field of the coordinated ligands dictates the magnetic properties underlining the ligand field environment as a salient feature. The coordination environment, coordination number around the metal ion, local point group symmetry, distortion around the metal ion,[154] and strength and position of the ligand field must be targeted simultaneously in order to produce large U_{eff} values. Magnetic anisotropy in these SIMs arises due to the interaction between the single metal ion and the ligand field, leading to a preferential direction of the magnetic moment. Hence, the dependence of the magnetic properties of SIMs on their surroundings, in addition to the structural and electronic aspects of the molecule, complicates the understanding of spin dynamics in SIMs. Stabilization of the highest $\pm M_J$ level and minimal mixing of these $\pm M_J$ states are crucial to achieve slow relaxation of magnetization and improved SIM characteristics. This favourable geometry can be achieved by placing the crystal field preferably along the axial and equatorial directions for oblate {Ce^{III}, Pr^{III}, Nd^{III}, Tb^{III}, Dy^{III} and Ho^{III}} and prolate {Pm^{III}, Sm^{III}, Er^{III}, Tm^{III} and Yb^{III}} ions,

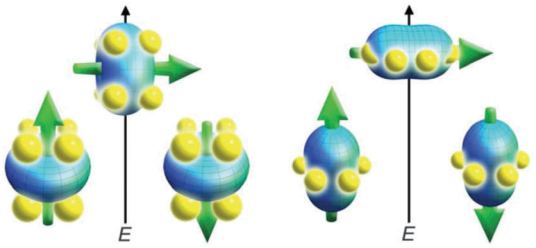

Fig. 22 Image describing the low- and high-energy configurations of the 4f-orbital electron density with respect to the ligand field environment for a 4f ion with oblate (left) and prolate (right) electron density. Reproduced from ref. 155 with permission from the Royal Society of Chemistry.

respectively (Fig. 22).[155] These presumptions are underlaid with the old tabulated Stevens coefficients[206a] α, β, γ of the rank (order) $k = 2, 4, 6$, respectively, of the extended Stevens operator O_k^q in the crystal field Hamiltonian. Only considering ground ranked parameters ($k = 2$) (B_k^q = computed crystal field parameter; B_2^0), Ln^{III} ions with negative α values (Ce^{III}, Pr^{III}, Nd^{III}, Tb^{III}, Dy^{III} and Ho^{III}) will possess the highest $\pm M_J$ level ground states in the presence of the axially elongated ligand field environment. However, the equatorial/axial compressed environment is expected to stabilize the highest $\pm M_J$ level ground state for Ln^{III} ions with positive α values {Pm^{III}, Sm^{III}, Er^{III}, Tm^{III} and Yb^{III}}.[154] To promote the stabilization of the medium-to-high $\pm M_J$ level, Tb^{III}, Er^{III} and Tm^{III} ions require preferred ligation along the *xy* plane, while Pr^{III}, Nd^{III}, Dy^{III}, Ho^{III} and Yb^{III} should have preferential ligation at polar angles of $\sim$50 to 60°.[154] This entails a proper definitive theoretical analysis[13c] of the crystal field Hamiltonian in Ln^{III} SIMs, as the crystal field solely leads to the zero-field splitting of the Ln^{III}-ion $\pm M_J$ ground state.[206b,206c] In order to achieve an ideal SIM, the extradiagonal parameters should be negligible and the diagonal parameters should prevail; otherwise, in the reverse case, the mixing of $\pm M_J$ levels will decrease the SIM behaviour.[154] Complexes with D_{4d}, C_{5h}, D_{6d} (ideal pseudo-axial symmetry) and symmetry of the order 7 or higher seems to be the ideal geometry to stabilise the highest $\pm M_J$ level ground state, given the maximization of B_2^0. In an axially elongated coordination environment (another crystal field parameter, A_k^q, is positive; $B_2^0 \propto \alpha A_2^0$), ions with positive α values are associated with positive B_2^0 values, while ions with negative α values possess negative B_2^0 values. On the other hand, in an axially compressed ligand field atmosphere (another crystal field parameter, A_k^q, is negative), ions with positive α values are associated with negative B_2^0 values, while ions with negative α values possess positive B_2^0 values. In general, the sign of B_2^0 is dictated by the axial (polar angle $< 54.7°$) or equatorial (polar angle $> 54.7°$) nature of the Ln^{III} centres. This synergistic correlation between the crystal field parameter, the nature of the Ln^{III} ion and the coordination environment is extremely crucial to obtain ideal SIMs.[154] Among all the Ln^{III} based SIMs, Dy^{III} {$^6H_{15/2}$} has been found to be the most promising[156,157] candidate due to (i) stronger magnetic anisotropy than the early lanthanides; (ii) the largest orbital angular momentum (M_J) and magnetic moment; (iii) an odd number of 4f electrons (9), which confirms the bistability and the presence of Kramer's doublets.[156a]

Electrostatic models based on electrostatic energy minimization (atomic charges coordinated to the metal centre) have been established to extract the orientation of the anisotropy axis.[158] At low temperature, the ground doublet of Dy^{III} ion is approximated as an effective spin of $S_{eff} = \frac{1}{2}$, with gyromagnetic factors $g_{\parallel} \sim 20$ and $g_{\perp} \sim 0$.[2c,159] This ideal case was evidenced by the *ab initio* calculations, where a very large energy barrier (>2085 cm^{-1}) was achieved for a perfect axially symmetric $[DyO]^{+}$ complex.[160] It is notable that extensive theoretical studies have proved non-collinearity between the principal molecular symmetry axis and the orientation of the magnetic anisotropy.[159,161] *Ab initio* calculations on Dy-aluminate complex $[Dy(AlMe_4)_3]$ (**138**) reproduced the experimental findings of weak SMM behaviour. Additionally, it is suggested that the intermolecular Dy–Dy interaction is a significant contributor to the observed prominent QTM effect.[162] Extensive studies were carried out on a series of twenty Dy^{III} SIMs[157] (ranging from zero-field and field induced to no SMM behaviour) to gain deeper insights into the key parameters that control the SMM characteristics. A meticulous survey revealed two types of compounds: (a) the heterolepticity of the ligand environment corresponds to the strongest axial anisotropy, while (b) sandwich type complexes are associated with small anisotropy. Triangular dodecahedron and square antiprismatic coordination environments were found to improve SIM/SMM behaviour, while cubic geometry has the reverse effect. The 4f-β electron densities of Dy^{III} tend to concentrate to an axially compressed shape, as expected for an oblate-shaped Dy^{III} ion, in order to minimise electrostatic repulsion.

The incorporation of electron withdrawing elements on the targeted ligands around Dy^{III} ion was found to substantially increase the U_{eff} values, as exemplified by $[Dy_2(valdien)_2(L)_2]$ (**139–140**) complexes {H_2valdien = *N*1,*N*3-bis(3-methoxysalicylidene) diethylenetriamine}; L = nitrate or acetate.[163] The application of a magnetic field and dilution of the magnetic sample induces suppression of QTM, resulting in enhanced U_{eff} values.[164] The linkage between *ab initio* calculations and experimental (IR,INS) techniques proved to be viable in the accurate determination of the ***g***-tensor anisotropy and other magnetic properties.[165] The correlation between the accurate ligand position and the nature of the 4f-electron density was evidenced by the *ab initio* calculations on $[Dy(COT)_2]^{-}$[166] complex (**141**). The preferential equatorially aligned COT''^{2-} ligand around Dy^{III} corresponds to the $M_J = \pm 1/2$ stable ground doublet in $[Dy(COT)_2]^{-}$,[167] corroborating earlier statements. Surprisingly, changes in the second coordination sphere ligated atoms, *i.e.* introducing trimethylsilyl groups onto the COT''^{2-} ligand, leads to a variation in the orientation of the ***g***-tensor anisotropy of ground state KD (see Fig. 23). Detailed magneto-structural correlation on $[Dy(DOTA)(H_2O)]^{+}$ (**142**) complex {DOTA = 1,4,7,10-tetraazacyclododecane *N*,*N*′*N*″,*N*‴-tetraacetic acid} clearly revealed the impact of the second-coordination sphere (hydrogen atoms of water molecules) on the orientation of the easy anisotropy axis, ***g***-tensor magnitudes and U_{cal} values.[159,161] The observation of slow magnetization dynamics in transverse anisotropic (easy plane anisotropy) Dy^{III}-analogue was again corroborated

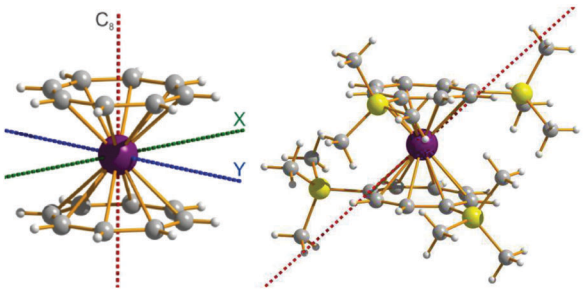

Fig. 23 Left: Orientation of the main anisotropy axis in the ground Kramer's doublet of $[Dy(COT)_2]^{-}$ along the C_8 axis; right: change of that axis on incorporation of trimethylsilyl groups on the COT''^{2-} ligand. Reprinted with permission from ref. 167. Copyright 2013 American Chemical Society. Reprinted with permission from ref. 166. Copyright 2014 Wiley-VCH.

by another set of calculations on [Dy(trensal)] complex (**143**) {trensal = 2,2′,2″-tris-(salicylideneimino)triethylamine}. This once again clearly indicates the lack of correlation between the magnetic anisotropy of Ln^{III} ions and the slow relaxation dynamics and emphasizes the necessity of spectroscopic techniques in this regard.[168,169] Rapid progress in *ab initio* calculations resulted in derivation of the magnetic relaxation pathways in several SIMs. Such calculations on $[(^{i}Pr_3Si)_2N\text{-}Dy\text{-}N(Si^{i}Pr_3)_2]^{+}$ (**144**) complex yielded six almost pure $\pm M_J$ states with two strongly mixed higher lying KDs. This was further corroborated by the complete Ising nature of the ground state KD ($g_{zz} = 19.9$ and $g_{xx} = g_{yy} = 0$) and the very large value of g_{yy} (~ 17.5) for the eighth KD; a barrier height as high as 1800 cm^{-1} has been suggested.[170,171] Very slight modification in the ligand field around Dy^{III}, *i.e.* replacement of an amine by an imine, leads to enhancement of the U_{cal}/U_{eff} values, as evidenced by calculations on {Dy^{III}*N*,*N*′-bis(imine-2-yl)methylene-1,8-diamino-3,6-dioxaoctan (**145**)} and {Dy^{III}*N*,*N*′-bis(amine-2-yl)methylene-1,8-diamino-3,6-dioxaoctane (**146**)}complexes [U_{cal}/U_{eff} as 95/35 and 59/24 cm^{-1} for **145** and **146**, respectively]. This is necessarily due to (i) shorter Dy-imine bonds inducing stronger bonds in the axial position and, hence, a stronger ligand field and (ii) subsequent increased electron density along the anisotropic axis, corresponding to the highly anisotropic Dy^{III} ion.[172] The strong equatorial ligand field created by the three negatively charged Cp′ ligands (compared to neutral phosphine) disfavours the SIM behaviour of $[Cp'_3Dy^{III}PH_2Mes]$ (**147**) adduct, resulting in a decrease of the U_{cal}/U_{eff} values.[173] The reduction of the cavity from $[Dy(15C5)(H_2O)_4]$ (**148**) to $[Dy(12C4)(H_2O)_5]$ (**149**) (larger in 15-crown-5 compared to the 12-crown-4 analogue) in a crown ether half-sandwich Dy^{III} complex results in zero-field SIM behaviour (U_{cal}/U_{eff} as 58/34 cm^{-1}) and no SIM behaviour for **148** and **149**, respectively.[174] Strongly linearly aligned negatively charged and weakly neutral ligands at the axial and equatorial sites, respectively, are ideally suited geometric environments for oblate type Dy^{III} ions. This was corroborated very recently[175] by calculations on two complexes, $[Dy(BIPM^{TMS})(BIPM^{TMS}H)]$ [$BIPM^{TMS} = \{C(PPh_2NSiMe_3)_2\}^{2-}$ and $BIPM^{TMS}H = \{HC(PPh_2NSiMe_3)_2\}^{-}$] (**150**) and $[Dy(BIPM^{TMS})_2]$-[K(18C6)(THF)2] (**151**). Magnetic relaxation is promoted *via* the 4th and 5th KD in **151**, resulting in the experimentally (565 cm^{-1}) and theoretically (563 cm^{-1}) largest ever barrier for magnetization

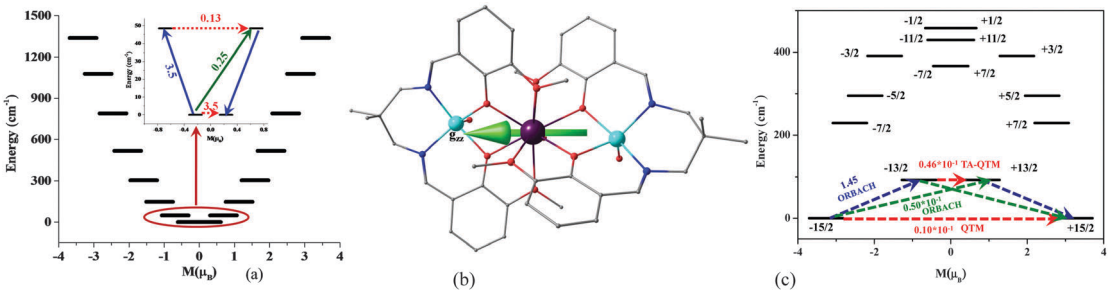

Fig. 24 (a) Magnetic relaxation computed for complex **152**. Reproduced from ref. 177 with permission from the Royal Society of Chemistry. (b) Ground state *g*-anisotropy orientation in complex **160**. Reprinted with permission from ref. 183. Copyright 2015 Wiley-VCH. (c) Magnetic relaxation computed for complex **160**. Reprinted with permission from ref. 183. Copyright 2015 Wiley-VCH.

reversal for any Dy^{III}-based SIM.[175] *Ab initio* calculations suggest pure well isolated $|\pm15/2\rangle$, $|\pm13/2\rangle$ and $|\pm11/2\rangle$ as the 1st, 2nd and 3rd KDs, respectively, quantized along the C = Dy = C axis (corresponding to bis-methandiide ligand). This subsequently quenches the relaxation *via* the low lying states and induces relaxation to occur *via* strongly mixed 4th and 5th KDs. For complex **150**, relaxation takes place *via* the 3rd KD, where there is a nice correlation between theory and experiments (U_{cal}/U_{eff} = 170/177 cm^{-1}). The quest for a suitable coordination number encouraged us to perform calculations on Dy^{III} models with varying coordination numbers (2 to 12). The calculations suggested a coordination number of ten to be the most favourable one, which is in good agreement with experimental observations.[176] The disadvantage of the equatorial ligand field around Dy^{III} was proved by our calculations with the stabilization of the $M_J = \pm1/2$ ground state for $[Dy^{III}(NSiMe_3)_3]$ (**152**) complex (see Fig. 24a and QTM = 3.5 μ_B). To our surprise, simple incorporation of two –THF (oxygen bound) ligands in the axial position $[Dy(NHPh^iPr_2)_3(THF)_2]$ (**153**) leads to the stabilization of the $M_J = \pm15/2$ state, stressing the presence of an axial ligand environment for oblate ions.[177] To achieve relaxation *via* the highest KDs, apart from favourable ligand arrangements, high symmetry also needs to be maintained. The computed/experimental barrier for $[Dy(^tBu\text{-}acac)_3bpy]$ (**154**) complex {^{t}Bu-acac = 2,2,6,6-tetramethylheptane-3,5-dionate and bpy = bipyridine} at different temperatures suggests that the magnetic anisotropic axis is insensitive to structural deformations due to thermal effects. Hence, the demarcation between theory and experiment can be attributed to the limited size of the employed basis sets, unaccounted dynamic correlation and intermolecular dipolar interaction.[178] We have also performed extensive calculations on {Dy-OH} models with varying coordination numbers around Dy^{III} and varying numbers of coordinated –OH ligands.[186] Our model studies predicted the crucial role of two axial ligands in stabilising a larger angular momentum projection for Dy^{III} SIMs. We would like to note here that based on our predictions, experimental groups[211a] synthesised a Dy^{III} air stable SIM complex possessing D_{5h} symmetry (two axial ligands). This complex unprecedentedly shows magnetization blocking (T_B) up to 12 K with an anisotropy barrier (U_{eff}) as high as 735.4 K (511.1 cm^{-1}; U_{cal} = 478.4 cm^{-1}). Most importantly, the magnetic hysteresis has been found to increase to 30 K (12 K), which is phenomenal in the field of MNMs (Table 6).[211a] This much larger barrier height for magnetization reversal is found to correlate to the pseudo D_{5h} symmetry found in this molecule. This high symmetry significantly quenches the QTM effects and promotes relaxation *via* the second excited KD, leading to a record high blocking temperature. This is another example where a coherent experimental and theoretical study unearthed a novel Dy^{III} single-ion magnet. This approach now has been extended to other lanthanide ions, yielding unprecedented SIM behaviour in other lanthanide complexes.[215]

As we mentioned earlier, the inclusion of 3d ions onto a 4f ion plays a proactive role in quenching QTM and increasing the U_{cal} value. On this note, the use of Zn^{II}-diamagnetic ion compared to other paramagnetic 3d ions is preferred because: (a) it promotes suppression of Ln–Ln exchange through internal magnetic dilution; (b) paramagnetic ions might generate random transverse fields, which would favour QTM and mitigate the relaxation; (c) it induces increments of ligand donor atom electron density. With all these logical background concepts, reports of $[Dy(HL)_2(NO_3)_3]$ (**156**) and $[ZnDy(NO_3)_2(L)_2(CH_3CO_2)]$ (**155**) {2-methoxy-6-[(*E*)-phenyliminomethyl]phenol (HL)} gain relevance. In our attempt[179] to enhance the ligand field interaction, we predicted that the incorporation of diamagnetic ions such as Zn^{II} can enhance the magnetic properties; complexes **156** and **155** prove this idea, where the barrier heights are estimated to be U_{cal}/U_{eff} = 91/83 cm^{-1} and 76(46)/16 cm^{-1} for complexes **155** and **156**, respectively. Moreover, the enhancement of U_{cal} (U_{eff}) upon inclusion of Zn^{II} (diamagnetic ion) has become the most pursued research topic of MNMs in recent years. This has thus instigated us to profoundly explore the relaxation and role of Zn^{II} ions in this regard. In both the complexes (**155** and **156**), calculations revealed axial type ground state anisotropy. DFT calculations predicted a larger negative charge polarization on the bridging oxygen of [ZnDy] (**155**) analogue compared to [Dy]-only complex (**156**), which subsequently promotes large electrostatic interaction.[179] This corresponds to the destabilization of excited states and enhanced U_{cal} values for [ZnDy] analogue (**155**), suggesting the necessity of the cation near the coordination environment to enhance the barrier for magnetization reversal.[179] *Ab initio* calculations predicted an axial (g_{zz} = 19.43) pure $M_J = |\pm15/2\rangle$ ground doublet (strong easy-axis anisotropy) for $[Zn_2Dy]$ $[ZnCl(\mu\text{-}L)Dy(\mu\text{-}L)ClZn][ZnCl_3(CH_3OH)]$ (**157**).

Table 6 Comparison of Dy^{III}-SIM with some mononuclear 4f polynuclear 4f and 3d-4f based SMMS

Complexes	U_{eff}/cm^{-1}	U_{cal}/cm^{-1}	ZFC maxima (T_B)/K	Hysteresis		Coercivity/T	Ambient air stability	Ref.
				T/K	T s^{-1}			
$[^tBuPO(NH^iPr)_2]_2[Dy(H_2O)_5][I]_3$	452.0, 511.1[c]	478.4	12	12[a]	0.0018	~0.9 (1.8 K)	Yes	211*a*
				30[b]	0.02	~1.5 (2.0 K)		
$[Dy(BIPM^{TMS})_2][K(18C6)(THF)_2]$	502, 565	563	10	16	0.0035	<0.7 (1.8 K)	No	175
						<0.8[c] (1.8 K)		
(Cp*)Er(COT)	224.5, 136.9	164.5	5[c]	5.0	0.000916	~ 0 (1.8 K)	No	211*b*
						~0.01[c] (1.8 K)		
(Cp*)Er(COT)	224.5, 136.9	164.5	—	—	0.07[c]	1.3[c] (1.6 K)	No	211*b*
$Er[N(SiMe_3)_2]_3$	122	331	—	1.9	—	~0	No	211*d*
$[Li(DME)_3][Er^{III}(COT'')_2]$	130	247.1	—	8.0	0.0022	0.6250 (1.8 K)	No	211*c*
$[Er(COT)_2]^-$	199	244.7	—	12	0.0035	0.7 (1.8 K)	No	166
$[Er(COT)_2]^-$	150.1	280.4	10[c]	10	0.00078	0.7 (1.8)	No	211*e*
						1.1[c] (1.8 K)		
$[Li(THF)_4[Er\{N(SiMe_3)_2\}_3Cl]\cdot 2THF]$	44.0	—	—	3[c]	0.00346	<0.02[c] (1.8 K)	No	211*f*
$[Pc_2Tb][TBA]$	230	—	—	—	—	—	No	4*a*
$[TbPc_2]/[TBA][Br]$	640.8[c]	—	—	—	—	—	No	211*g*
$[TBA][Tb\{Pc(phth^3)\}_2]$	463	—		2.0	0.01666	<0.03 (2.0 K)	No	211*h*
$[TbPc_2]$	410.1	—	—	—	—	—	No	211*i*
$[Tb\{Pc(OEt)_8\}_2][SbCl_6]$	549.7	—	—	—	—	—	No	211*j*
$[TBA][Tb\{Pc(OEt)_8\}_2]$	508.7	—	—	—	—	—	No	211*j*
$[Tb\{Pc(S\text{-}DOP)_8\}_2]$	479.6	—	—	—	—	—	No	211*k*
$[Tb(Pc)(Pc')]^-$	652	—	—	—	—	—	No	211*l*
$[(Cp'_2Dy)\{\mu\text{-}P(H)Mes\}]_3$	210, 256[c]	127, 134, 135	—	4.4[c]	0.0026[c]	~0.03[c] (1.8 K)	No	173
$[K(18C6)]\{[(Me_3Si)_2N]_2(THF)Dy\}_2$-$(\mu\text{-}\eta^2\text{:}\eta^2\text{-}N_2)$	123	—	8.3	8.3	0.08	~1.5 (2–6 K)	No	87*b*
$[Dy_4K_2O(O^tBu)_{12}]\cdot C_6H_{14}$	481, 220	373	—	5.0	0.14	<0.15 (0.03 K)	No	211*m*
	585[c]	617		6.0[c]		~0.25[c] (0.03 K)		
$[Dy_5(\mu_5\text{-}O)(\mu_3\text{-}O^iPr)_4(\mu_2\text{-}O^iPr)_4(O^iPr)_5]$	367	400	—	1.85	—	—	No	211*m* and
	559[d]	685		7[c]	0.001[c]	~0[c]		211*n*
$[K(18C6)(THF)_2][\{[(Me_3Si)_2N]_2$-$(THF)Tb\}_2(\mu\text{-}\eta^2\text{:}\eta^2\text{-}N_2)]$	227	—	14	14	0.0009	<5.0 (11 K)	No	87*a*
$[(\eta^5\text{-}Cp)_2Dy(\mu\text{-}bpym)]_2[BPh_4]$	88	—	6.5	6.5	0.002	~0.6 (3 K)	No	211*o*
$[Dy(hfac)_3(\mu\text{-}pyNO)]_2$	116	—	—	1.4	0.02	~0.0121 (1.4 K)	Yes	211*p*
$[Cp'_2Dy(\mu\text{-}SSiPh_3)]_2$	133	113	—	1.8	—	~0	No	211*q*
$[Er_2(COT'')_3]$	224	~168	—	12	0.0022	<0.2 (1.8 K)	No	211*r*
$K_2(THF)_4[Er_2^{III}(COT)_4]$	213	~188	—	12	0.0018	~0 (1.8 K)	No	211*r*
$[Zn_2(L^1)_2DyCl_3]\cdot 2H_2O$	299	355.6	<4.5	8	0.000166–0.0005	~0 (1.8 K)	Yes	211*s*
				12	0.02	—		
	302[c]		—	—	—	0.03[c] (1.8 K)		
$[Zn_2(L^1)_2Dy(MeOH)Br_3]\cdot 3H_2O$	162	351.8	<3.5	6	0.000166–0.0005	~0 (1.8 K)	Yes	211*s*
$[Zn_2(L^1)_2Dy(H_2O)Br_2]\cdot[ZnBr_4]_{0.5}$	84	313	<2.5	4	0.000166–0.0005	~0 (1.8 K)	Yes	211*s*
$[Zn_2(L^2)_2DyCl_3]\cdot 2H_2O$	277	351.9	<4.5	8	0.000166–0.0005	~0 (1.8 K)	Yes	211*s*
$[Fe_2Dy(L^3)_2(H_2O)]ClO_4\cdot 2H_2O$	319	313.9	—	—	—	—	Yes	211*t*
$[Zn_2Dy(L^4)_2(MeOH)]NO_3$	305	289	—	11	0.02	>0.02 (2.0 K)	Yes	211*u*
$[Co_2Dy(L^4)_2(H_2O)]NO_3$	417	—	—	—	—	—	Yes	211*v*
$[Dy(Cy_3PO)_2(H_2O)_5]Cl_3$	328	299	<8	11	—	—	Yes	211*w*
$[Dy(Cy_3PO)_2(H_2O)_5]Br_3$	377.4	276	<11	20	—	—	Yes	211*w*
[Dy(bbpen)Cl]	492	586	7.5	8	—	—	Yes	211*x*
[Dy(bbpen)Br]	712	721	9.5	14	—	—	Yes	211*x*

[a] Hysteresis mode. [b] Continuous sweep mode. [c] Diluted in diamagnetic matrix. [d] (–) = not reported. (~) = close to or not equal to. $BIPM^{TMS}$ = $\{C(PPh_2NSiMe_3)_2\}^{2-}$; 18C6 = 18-crown-6; Cp* = pentamethylcyclopentadienide; COT = cyclooctatetraene; DME = dimethoxyethane; COT'' = 1,4-bis-(trimethylsilyl)cyclooctatetraenyl dianion; THF = tetrahydrofuran; Pc = dianion of phthalocyanine; TBA = tetra-*n*-butyl ammonium; Pc(phth3) = bis(*N*,*N*,*N*,*N*-tetra((*S*)-methyl(phenyl)methyl)-29*H*,31*H*-2,3,9,10,16,17,23,24-phthalocyaninatotetradicarboximide); $Pc(OEt)_8$ = dianion of 2,3,9,10,16,17,23,24-octaethoxyphthalocyanine; SDOP = (*S*)-2-(dodecyloxy)propan-1-oxy; Pc' = octa(*tert*-butylphenoxy)-phthalocyanine; Cp' = η^5-C_5H_4Me; Mes = mesityl; bpym = 2,2′-bipyrimidine; hfac = hexafluoroacetylacetonate; PyNO = pyridine-*N*-oxide; H_2L^1 = *N*,*N*′-bis(3-methoxysalicylidene)phenylene-1,2-diamine; H_2L^2 = *N*,*N*′-bis(3-methoxysalicylidene)-1,2-diaminocyclohexane; L^3 = 2,2′,2″-(((nitrilotris(ethane-2,1-diyl))tris(azanediyl))tris(methylene))tris-(4-chlorophenol); L^4 = 2,2′,2″-(((nitrilotris(ethane-2,1-diyl))tris(azanediyl))tris(methylene))tris-(4-bromophenol); H_2bbpen = *N*,*N*′-bis(2-hydroxybenzyl)-*N*,*N*′-bis(2-methylpyridyl)ethylenediamine.

Complex {H_2L = *N*,*N*′-dimethyl-*N*,*N*′-bis(2-hydroxy-3-formyl-5-bromo-benzyl)ethylenediamine}, which is in line with the experimental zero-field SMM behaviour (U_{cal}/U_{eff} = 129/97 cm^{-1}). The calculated ground KD magnetic moment is located between the planes constituted by two Dy–O–Zn–O moieties and is colinear with the two shortest Dy–O distances, stressing the oblate nature of Dy^{III} (in compliance with the electrostatic model).[180] The efficacy of this topic induced profound study on another set of complexes (**158**) possessing $[Zn_2^{II}Dy^{III}]^{3+}$ core structures with ligands = {[2-(2-hydroxy-3-(hydroxymethyl)-5-methylbenzylideneamino)-2-methylpropane-1,3-diol] (LH_4)}, where the relaxation is computed to occur through the first excited KD (U_{cal}/U_{eff} = 147/47 cm^{-1}), predominantly *via* the TA-QTM process. The ground state is strongly axial, and this uniaxial anisotropy is

found to orient along the Zn^{II}–Dy^{III}–Zn^{II} unit. Experiments clearly revealed the Zn^{II}–Dy^{III}–Zn^{II} unit as an origin of magnetic relaxation rather than intermolecular interactions/long range ordering.[181] *Ab initio* calculations suggested pure Ising type ground state anisotropy, corresponding to an almost pure $M_J = |\pm 15/2\rangle$ state for $[ZnCl(\mu\text{-}L)Dy(\mu\text{-}L)ClZn]PF_6$ (**159**) {H_2L = *N*,*N*′-dimethyl-*N*,*N*′-bis(2-hydroxy-3-formyl-5-bromo-benzyl)ethylenediamine}. The C_2 symmetry axis around Dy^{III} ion in complex **159** enforces a different electronic distribution in the Dy^{III} coordination sphere and consequently induces relaxation *via* the 2nd excited KD (U_{cal}/U_{eff} = 243/222 cm^{-1}).[182] Recently, we have studied three complexes: $[LZn(H_2O)_2Dy(H_2O)](CF_3SO_3)_3$ (**160**), $[(LZnBr)_2Dy(H_2O)](ClO_4)$ (**161**) and $[(LZnCl)_2Dy(H_2O)](ClO_4)(MeOH)$ (**162**, see Fig. 24b and the corresponding magnetic relaxation mechanism in Fig. 24c) H_2L is the N_2O_2 compartmental ligand, *N*,*N*′-2,2-dimethylpropylenedi(3-methoxysalicylideneiminato); these complexes are isostructural but vary in the nature of the ligand coordinated to Zn^{II}. All the complexes are associated with pure Ising type ground anisotropy, approaching the pure $M_J = |\pm 15/2\rangle$ state. An electrostatic potential model attempted on the three complexes indicated that the anisotropy axis is prone to ligand donor atoms with greater electron densities and shorter Dy–O bonds and enforces Dy^{III}-oblate electron density to be perpendicular to them, mitigating the subsequent electrostatic repulsions. DFT calculations revealed larger negative charges on the μ_2-oxo bridging ligand than on the coordinated neutral donor ligand atoms. As the electronegativity of the ligands was found to decrease, the U_{cal} values also decreased.[183]

Modelling *g* tensors in Er^{III} based mononuclear complexes. Among several Er^{III} complexes, very few show SMM characteristics. However, the large blocking temperatures (T_B) associated with some of these complexes have drawn attention and have led to extensive theoretical analysis.[168,184] Moreover, as Dy^{III} and Er^{III} [$^4I_{15/2}$] have similar M_J values but vary in their types of 4f-electron density (oblate *vs.* prolate), unravelling the role of the ligand field, coordination number, and relaxation mechanism in prolate Er^{III}-based SIMs is extremely crucial. Firstly, it is worth noting that, among all the Ln^{III} ions, the effect of CASPT2 on *ab initio* calculations is pronounced only for Er^{III}-based compounds.[161]

Like the observation in Dy^{III}, here as well, peripheral ligand substitution, *i.e.* changes in the second coordination sphere, led to significant changes in the *g* tensor anisotropy and numerical U_{cal} estimates.[185] Calculations predicted an expected ground state of $M_J = |\pm 15/2\rangle$ correctly for $(NBu_4)^+[Er^{III}Pc_2]^-$ (**163**) complex, which was confirmed by spectroscopic evidence as well.[165] The unprecedented SIM characteristics of $[Er(COT)_2]^-$ complex (**164**) were noted, contrary to the lack of SIM behavior of the corresponding Dy^{III} analogue.[166] This directly correlates to the favourable strong equatorial ligand field created by COT''^{2-} and leads to the stabilization of the expected $M_J = |\pm 15/2\rangle$ ground state.[166] We have performed calculations on four Er^{III} complexes $[Er(thd)_3(bath)]$ (where thd = (2,2,6,6-tetramethyl-3,5-heptanedionate), bath = bathophenanthroline) (**165**), $[Er(COT)_2]^-$ (where COT = (cyclooctatetraenyl dianion)) (**166**), $[Er(COT'')_2]^-$ (where COT″ = (1,4-bis(trimethylsilyl) cyclooctatetraenyl dianion)) (**167**), $[Er(COT)Cp^*]^-$ (where Cp* = (pentamethylcyclopentadienide), COT = (cyclooctatetraenyl dianion)) (**168**). Among these structures, one is low-symmetric, while the remaining three are highly symmetric with some structural distortions. The numerical U_{cal} estimates were found to decrease proportionately with reduction of the ligand field symmetry. In this study, in addition to complying with experiments, we have predicted the largest barrier height for $[Er(OH)_4]^-$ (D_{4h} symmetry; U_{cal} = 735 cm^{-1}; see Fig. 25a) and $[Dy(OH)_2]^+$ (U_{cal} = 2109 cm^{-1}) through our model studies.[186] The correlation between the prolate-electron density and the perfect equatorial ligand field was again evidenced by our calculations on Er(III) complex $[Er^{III}(NSiMe_3)_3]$ (**169**). This ideal environment shows unprecedented relaxation *via* the 4th excited KD and outlines the barrier as 331 cm^{-1}. In contrast, the simple addition of two O-ligands at the axial position in the complex $[Er(NHPh^iPr_2)_3(THF)_2]$ (**170**) destroys the perfect

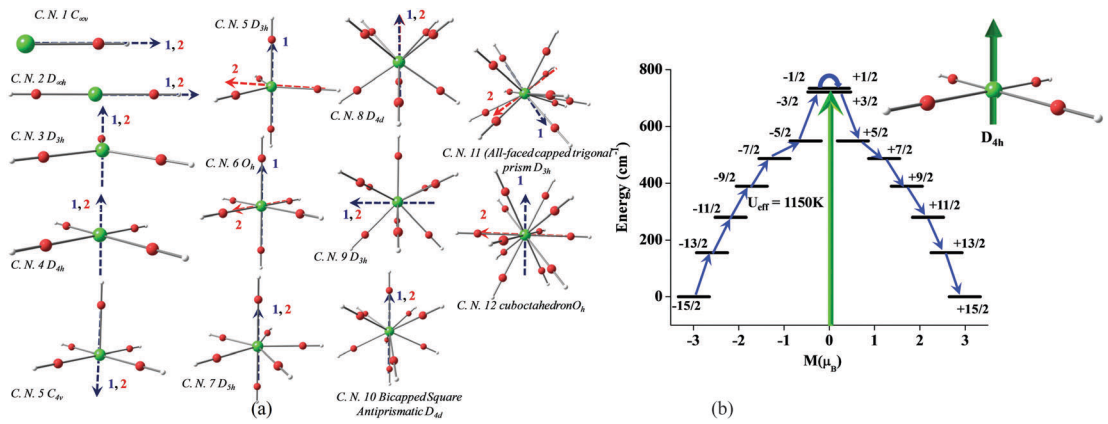

Fig. 25 (a) *Ab initio* computed principal magnetization axes of all the model complexes of Er^{III} along with –OH ligand with varying coordination numbers from 2 to 12. The dashed blue lines shown in the figures are the calculated main magnetic axis of the ground state KD, while the dashed red lines are the main magnetic axis of the first excited state KD. Reprinted with permission from ref. 186. Copyright 2014 American Chemical Society. (b) The energy barrier for magnetization reversal in the $[Er(OH)_4]^-$ model complex. The thick black line indicates the KDs as a function of the magnetic moment. The blue arrows show the path for the reorientation of magnetization. Reprinted with permission from ref. 186. Copyright 2014 American Chemical Society.

equatorial geometry, and this is also reflected in the significantly operative QTM ($0.11\mu_B$) and the field-induced SIM behaviour.[177] The reduction of ligand field symmetry and the number of donor atoms in the axial position was found to correlate to the enhancement of U_{cal} values, stressing the prominent role of a suitable ligand environment for prolate Er^{III} ions.[187] The vital role of the structural parameters instigated us to perform magneto-structural correlation, resulting in an unprecedented relaxation *via* the 7th excited KD ($U_{cal} > 750\ cm^{-1}$) for a planar structure (see Fig. 25b).

4. Conclusions and outlook

With the rapid progress in the development of theoretical methodology along with computing hardware, we have witnessed a tremendous utilization of computational tools in several areas of chemistry, including that of magnetic materials. Particularly in the area of MNMs, where controlling the spin Hamiltonian parameters is of crucial importance, theory has played a significant role both in rationalizing observed magnetic properties and also in making viable predictions. In this article, we have attempted to provide a holistic view of modelling the spin Hamiltonian parameters of molecular magnets. Depending on the system of interest, the nature of the parameter varies; therefore, we have covered pragmatic instances of computing the isotropic magnetic exchange interaction (J), anisotropic exchange interaction (J_x, J_y, J_z), double exchange interaction (B), zero-field splitting parameters (D, E), exchange anisotropy ($D_{MM'}$), and g-tensors (see Fig. 26). Over the years, our group has studied several systems in each of these categories, and we have seen much divergence based on the class of complexes studied. Perspectives drawn from our work and the work of other groups in this area are summarized below:

(a) For the estimation of isotropic magnetic coupling, regardless of the class of complexes (di- or polynuclear transition metals, 3d-Gd, Gd–Gd, Gd-2p, *etc.*), DFT calculations emerge as the superior choice, where the popular B3LYP functional in combination with a triple-ζ basis set offers good numerical estimates of J constants. For lanthanide complexes, however, incorporation of relativistic effects *via* ECP or through DKH/ZORA is important to obtain good numerical estimates.

(b) Revisiting the DFT calculations performed on several manganese clusters suggests that the J–T dihedral could be a useful tool for predicting the sign of J values. It is imperative to state here that DFT calculations should be a part of routine magnetic characterization for large clusters (transition metal or otherwise), as the conventional methodology of fitting the susceptibility data has several shortcomings (over-parameterization, aging of complexes, ambiguity in hydrogen positions, *etc.*).

(c) DFT and *ab initio* calculations established the role of the empty 5d orbitals of Gd^{III} ion in obtaining ferromagnetic coupling in {3d-Gd} clusters. Although antiferromagnetic coupling has been witnessed in some cases, the majority of the examples studied yield ferromagnetic coupling regardless of the nature of the 3d ion, bridging ligands and structural distortions. As {3d-Gd} interactions are looked upon as a viable way to quench the QTM effects in SMMs, there are some disappointments, as very large J values (on the order of hundreds of wave numbers) have not been found.

(d) {Gd–Gd} interactions are intrinsically weak, while {Gd-2p} interactions are very strong. This is essentially due to direct exchange, where the radical antibonding orbitals directly engage the 4f orbitals, leading to antiferromagnetic coupling. Although J values as high as $\sim 30\ cm^{-1}$ have been reached now, if an alternate class of molecules (endohedral fullerene) are adapted, very large J values are achievable.

(e) Unlike isotropic exchange coupling, double-exchange and anisotropic exchange have not been studied in detail. However, the preliminary examples studied demonstrate the potential of DFT calculations in estimating these intricate parameters.

(f) For the estimation of zfs parameters, *ab initio* calculations are found to be more trustworthy. This is due to the fact that in the majority of the cases studied, the zfs of mononuclear complexes or mononuclear fragments in the cluster framework been sought where very high-level calculations can still be performed. Among the complexes reviewed here, the CASSCF/NEVPT2 with (QDPT)/EHA approach has been found to yield good theoretical estimates of zfs parameters. In polynuclear clusters, the exchange anisotropy significantly reduces the overall cluster anisotropy. Despite its importance, very few experimental and theoretical efforts have been undertaken to probe this effect to date.

(g) For the estimation of magnetic anisotropy in lanthanide complexes, the *ab initio* CASSCF/RASSI-SO/SINGLE_ANISO methodology has been widely adapted. These calculations have made significant advancements in this area and are now considered to be an integral part of the characterization techniques for lanthanide SMMs. To exploit the full potential of this technique, apart from rationalizing the experimental observables, significant efforts should be undertaken to predict novel molecules possessing targeted magnetic properties.

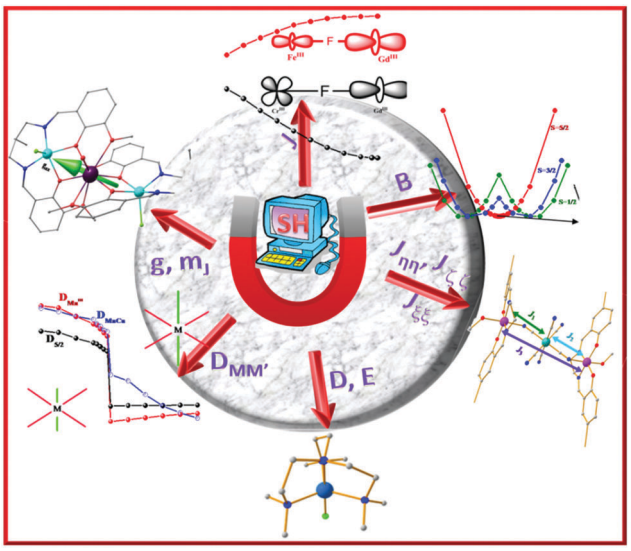

Fig. 26 Schematic illustrating how computational techniques can be employed to calculate several SH parameters in MNMs.

In summary, by choosing the right set of theoretical tools, it is now possible to acquire several experimental observations in the area of MNMs. If these tools are employed side-by-side with synthesis and magnetic and spectral characterizations, one can surpass serendipity and move towards logical ways to accomplish new generations of MNMs.

Acknowledgements

GR would like to acknowledge several collaborators over the years for offering their intriguing molecules for theoretical studies. Particularly, several Mn clusters reported here were originally made by Prof. E. K. Brechin, University of Edinburgh, and several {3d-Gd} clusters studied were synthesized by Prof. J. Bendix, University of Copenhagen. Some of the Co^{II} monomers and Dy^{III} SMMs studied were made by Prof. S. Maheshwaran, IIT Bombay while other Dy^{III} SMMs were made by Prof. R. Murugavel, IIT Bombay, Prof. J. P. Costes, Toulouse, France and Prof. E. Colocio, University of Granada, Spain. Some of the work listed here was published during the early academic career of GR; therefore, he would like to thank his hosts at the University of Manchester, UK (Profs Richard E. P. Winpenny and Eric J. L. McInnes), University of Florence, Italy (Profs Dante Gatteschi, Roberta Sessoli, Andrea Caneshi and the late Alessandro Bencini), University of Barcelona, Spain (Prof. Eliseo Ruiz) and University of Heidelberg, Germany (Prof. Peter Comba). GR acknowledges DST (EMR/2014/000247) for funding and TG thanks UGC for a SRF fellowship.

References

1 (*a*) A. Cornia, A. F. Costantino, L. Zobbi, A. Caneschi, D. Gatteschi, M. Mannini and R. Sessoli, in *Single-Molecule Magnets and Related Phenomena*, ed. R. Winpenny, Springer, Berlin, Heidelberg, 2006, pp. 133–161; (*b*) S. Gao, *Molecular Nanomagnets and Related Phenomena*, Springer, Berlin, Heidelberg, 2015; (*c*) R. S. D. Gatteschi and J. Villain, *Molecular Nanomagnets*, Oxford University Press, Oxford, 2006; (*d*) O. Kahn, *Molecular Magnetism*, VCH Publishers, INc., Orsay, France, 1993; (*e*) C. Benelli and D. Gatteschi, *Introduction to Molecular Magnetism*, Wiley-VCH Verlag GmbH & Co. KGaA, Weinheim, Germany, 2015, pp. I–VII, DOI: 10.1002/9783527690541.fmatter.

2 (*a*) V. M. M. A. K. Zvezdin, A. A. Mukhin and A. I. Popov, *Rare-earth ions in ordered magnetic crystals*, Nauka, Moscow, 1985, p. 296; (*b*) G. L. Abbati, L.-C. Brunel, H. Casalta, A. Cornia, A. C. Fabretti, D. Gatteschi, A. K. Hassan, A. G. M. Jansen, A. L. Maniero, L. Pardi, C. Paulsen and U. Segre, *Chem. – Eur. J.*, 2001, **7**, 1796–1807; (*c*) A. Abragam and B. Bleaney, *Electron Paramagnetic Resonance of Transition Ions*, Oxford University Press, Oxford, UK, 1970; (*d*) S. M. T. Abtab, M. Maity, K. Bhattacharya, E. C. Sañudo and M. Chaudhury, *Inorg. Chem.*, 2012, **51**, 10211–10221; (*e*) S. M. T. Abtab, M. C. Majee, M. Maity, J. Titiš, R. Boča and M. Chaudhury, *Inorg. Chem.*, 2014, **53**, 1295–1306.

3 R. E. P. Winpenny, *Angew. Chem., Int. Ed.*, 2008, **47**, 7992–7994.

4 (*a*) N. Ishikawa, M. Sugita, T. Ishikawa, S. Koshihara and Y. Kaizu, *J. Am. Chem. Soc.*, 2003, **125**, 8694–8695; (*b*) J. M. Clemente-Juan, E. Coronado and A. Gaita-Ariño, *Lanthanides and Actinides in Molecular Magnetism*, Wiley-VCH Verlag GmbH & Co. KGaA, 2015, pp. 27–60.

5 (*a*) L. K. Thompson and L. N. Dawe, *Coord. Chem. Rev.*, 2015, **289–290**, 13–31; (*b*) F. Neese and D. A. Pantazis, *Faraday Discuss.*, 2011, **148**, 229–238.

6 (*a*) L. Bogani, A. Vindigni, R. Sessoli and D. Gatteschi, *J. Mater. Chem.*, 2008, **18**, 4750–4758; (*b*) D. Gatteschi and A. Vindigni, *Molecular Magnets*, Springer, Berlin, Heidelberg, 2014, pp. 191–220.

7 F. K. Larsen, E. J. L. McInnes, H. El Mkami, J. Overgaard, S. Piligkos, G. Rajaraman, E. Rentschler, A. A. Smith, G. M. Smith, V. Boote, M. Jennings, G. A. Timco and R. E. P. Winpenny, *Angew. Chem., Int. Ed.*, 2003, **42**, 101–105.

8 R. Sessoli, D. Gatteschi, A. Caneschi and M. A. Novak, *Nature*, 1993, **365**, 141–143.

9 Y. Rechkemmer, J. E. Fischer, R. Marx, M. Dörfel, P. Neugebauer, S. Horvath, M. Gysler, T. Brock-Nannestad, W. Frey, M. F. Reid and J. van Slageren, *J. Am. Chem. Soc.*, 2015, **137**, 13114–13120.

10 E. Ruiz, A. Rodriguez-Fortea, J. Cano, S. Alvarez and P. Alemany, *J. Comput. Chem.*, 2003, **24**, 982–989.

11 (*a*) F. Neese and E. I. Solomon, *Inorg. Chem.*, 1998, **37**, 6568–6582; (*b*) J. Cirera, E. Ruiz, S. Alvarez, F. Neese and J. Kortus, *Chem. – Eur. J.*, 2009, **15**, 4078–4087; (*c*) S. Gómez-Coca, D. Aravena, R. Morales and E. Ruiz, *Coord. Chem. Rev.*, 2015, **289–290**, 379–392.

12 E. A. Suturina, D. Maganas, E. Bill, M. Atanasov and F. Neese, *Inorg. Chem.*, 2015, **54**, 9948–9961.

13 (*a*) B. Wang, S. Jiang, X. Wang and S. Gao, *Sci. China, Ser. B: Chem.*, 2009, **52**, 1739–1758; (*b*) S. T. Liddle and J. van Slageren, *Chem. Soc. Rev.*, 2015, **44**, 6655–6669; (*c*) L. Sorace, C. Benelli and D. Gatteschi, *Chem. Soc. Rev.*, 2011, **40**, 3092–3104.

14 (*a*) J. Tange and P. Zhang, *Lanthanide Single Molecule Magnets*, Springer(DE), Berlin, Germany, 2015; (*b*) D. N. Woodruff, R. E. P. Winpenny and R. A. Layfield, *Chem. Rev.*, 2013, **113**, 5110–5148.

15 (*a*) M. Evangelisti and E. K. Brechin, *Dalton Trans.*, 2010, **39**, 4672–4676; (*b*) M. Evangelisti, F. Luis, L. J. de Jongh and M. Affronte, *J. Mater. Chem.*, 2006, **16**, 2534–2549.

16 C. Rudowicz and M. Karbowiak, *Coord. Chem. Rev.*, 2015, **287**, 28–63.

17 J. Kortus, M. R. Pederson, T. Baruah, N. Bernstein and C. S. Hellberg, *Polyhedron*, 2003, **22**, 1871–1876.

18 E. Ruiz, in *Principles and Applications of Density Functional Theory in Inorganic Chemistry II*, ed. N. Kaltsoyannis and J. E. McGrady, Springer, Berlin, Heidelberg, 2004, pp. 71–102, DOI: 10.1007/b97942.

19 F. Neese, T. Petrenko, D. Ganyushin and G. Olbrich, *Coord. Chem. Rev.*, 2007, **251**, 288–327.

20 E. Ruiz, *Comprehensive Inorganic Chemistry II*, Elsevier, Amsterdam, 2nd edn, 2013, pp. 501–549.

21 O. Hanebaum and J. Schnack, *Phys. Rev. B: Condens. Matter Mater. Phys.*, 2015, **92**, 064424.

22 L. Noodleman and E. R. Davidson, *Chem. Phys.*, 1986, **109**, 131–143.

23 E. Ruiz, J. Cano, S. Alvarez and P. Alemany, *J. Comput. Chem.*, 1999, **20**, 1391–1400.

24 T. Soda, Y. Kitagawa, T. Onishi, Y. Takano, Y. Shigeta, H. Nagao, Y. Yoshioka and K. Yamaguchi, *Chem. Phys. Lett.*, 2000, **319**, 223–230.

25 (*a*) E. Ruiz, S. Alvarez, A. Rodríguez-Fortea, P. Alemany, Y. Pouillon and C. Massobrio, *Magnetism: Molecules to Materials*, Wiley-VCH Verlag GmbH & Co. KGaA, 2004, pp. 227–279, DOI: 10.1002/9783527620548.ch7a; (*b*) A. Bencini and F. Totti, *Int. J. Quantum Chem.*, 2005, **101**, 819–825.

26 C. Benelli and D. Gatteschi, *Chem. Rev.*, 2002, **102**, 2369–2387.

27 A. Caneschi, D. Gatteschi and F. Totti, *Coord. Chem. Rev.*, 2015, **289–290**, 357–378.

28 G. Aromí and E. K. Brechin, in *Single-Molecule Magnets and Related Phenomena*, ed. R. Winpenny, Springer, Berlin, Heidelberg, 2006, pp. 1–67, DOI: 10.1007/430_022.

29 N. Berg, T. Rajeshkumar, S. M. Taylor, E. K. Brechin, G. Rajaraman and L. F. Jones, *Chem. – Eur. J.*, 2012, **18**, 5906–5918.

30 W. P. Barros, R. Inglis, G. S. Nichol, T. Rajeshkumar, G. Rajaraman, S. Piligkos, H. O. Stumpf and E. K. Brechin, *Dalton Trans.*, 2013, **42**, 16510–16517.

31 P. Comar, T. Rajeshkumar, G. S. Nichol, M. B. Pitak, S. J. Coles, G. Rajaraman and E. K. Brechin, *Dalton Trans.*, 2015, **44**, 19805–19811.

32 J. E. McGrady and R. Stranger, *J. Am. Chem. Soc.*, 1997, **119**, 8512–8522.

33 R. Hotzelmann, K. Wieghardt, U. Floerke, H. J. Haupt, D. C. Weatherburn, J. Bonvoisin, G. Blondin and J. J. Girerd, *J. Am. Chem. Soc.*, 1992, **114**, 1681–1696.

34 X. G. Zhao, W. H. Richardson, J. L. Chen, J. Li, L. Noodleman, H. L. Tsai and D. N. Hendrickson, *Inorg. Chem.*, 1997, **36**, 1198–1217.

35 C. D. Delfs and R. Stranger, *Inorg. Chem.*, 2001, **40**, 3061–3076.

36 C. D. Delfs and R. Stranger, *Inorg. Chem.*, 2000, **39**, 491–495.

37 M. Corbella, R. Costa, J. Ribas, P. H. Fries, J.-M. Latour, L. Öhrström, X. Solans and V. Rodríguez, *Inorg. Chem.*, 1996, **35**, 1857–1865.

38 G. Rajaraman, E. C. Sañudo, M. Helliwell, S. Piligkos, W. Wernsdorfer, G. Christou and E. K. Brechin, *Polyhedron*, 2005, **24**, 2450–2454.

39 P. Christian, G. Rajaraman, A. Harrison, M. Helliwell, J. J. W. McDouall, J. Raftery and R. E. P. Winpenny, *Dalton Trans.*, 2004, 2550–2555.
40 L. F. Jones, G. Rajaraman, J. Brockman, M. Murugesu, E. C. Sañudo, J. Raftery, S. J. Teat, W. Wernsdorfer, G. Christou, E. K. Brechin and D. Collison, *Chem. – Eur. J.*, 2004, **10**, 5180–5194.
41 A. Prescimone, J. Wolowska, G. Rajaraman, S. Parsons, W. Wernsdorfer, M. Murugesu, G. Christou, S. Piligkos, E. J. L. McInnes and E. K. Brechin, *Dalton Trans.*, 2007, 5282–5289.
42 T. N. Mandal, S. Roy, S. Konar, A. Jana, K. Das, S. Ray, S. Gupta, R. Saha, M. S. El Fallah, J. Tercero, R. J. Butcher, S. Chatterjee and S. K. Kar, *Dalton Trans.*, 2012, **41**, 413–423.
43 G. Rajaraman, M. Murugesu, E. C. Sanudo, M. Soler, W. Wernsdorfer, M. Helliwell, C. Muryn, J. Raftery, S. J. Teat, G. Christou and E. K. Brechin, *J. Am. Chem. Soc.*, 2004, **126**, 15445–15457.
44 C. J. Milios, M. Manoli, G. Rajaraman, A. Mishra, L. E. Budd, F. White, S. Parsons, W. Wernsdorfer, G. Christou and E. K. Brechin, *Inorg. Chem.*, 2006, **45**, 6782–6793.
45 E. Cremades, J. Cano, E. Ruiz, G. Rajaraman, C. J. Milios and E. K. Brechin, *Inorg. Chem.*, 2009, **48**, 8012–8019.
46 C. J. Milios, A. Vinslava, P. A. Wood, S. Parsons, W. Wernsdorfer, G. Christou, S. P. Perlepes and E. K. Brechin, *J. Am. Chem. Soc.*, 2007, **129**, 8–9.
47 A.-R. Tomsa, J. Martinez-Lillo, Y. Li, L.-M. Chamoreau, K. Boubekeur, F. Farias, M. A. Novak, E. Cremades, E. Ruiz, A. Proust, M. Verdaguer and P. Gouzerh, *Chem. Commun.*, 2010, **46**, 5106–5108.
48 T. C. Stamatatos, D. Foguet-Albiol, K. M. Poole, W. Wernsdorfer, K. A. Abboud, T. A. O'Brien and G. Christou, *Inorg. Chem.*, 2009, **48**, 9831–9845.
49 S. K. Langley, N. F. Chilton, B. Moubaraki and K. S. Murray, *Dalton Trans.*, 2012, **41**, 9789–9796.
50 K. R. Vignesh, S. K. Langley, K. S. Murray and G. Rajaraman, *Chem. – Eur. J.*, 2015, **21**, 2881–2892.
51 E. C. Sañudo, T. Cauchy, E. Ruiz, R. H. Laye, O. Roubeau, S. J. Teat and G. Aromí, *Inorg. Chem.*, 2007, **46**, 9045–9047.
52 E. Ruiz, T. Cauchy, J. Cano, R. Costa, J. Tercero and S. Alvarez, *J. Am. Chem. Soc.*, 2008, **130**, 7420–7426.
53 J. Cano, R. Costa, S. Alvarez and E. Ruiz, *J. Chem. Theory Comput.*, 2007, **3**, 782–788.
54 Z. Zeng, D. Guenzburger and D. E. Ellis, *Phys. Rev. B: Condens. Matter Mater. Phys.*, 1999, **59**, 6927–6937.
55 V. V. Mazurenko, Y. O. Kvashnin, F. Jin, H. A. De Raedt, A. I. Lichtenstein and M. I. Katsnelson, *Phys. Rev. B: Condens. Matter Mater. Phys.*, 2014, **89**, 214422.
56 D. Foguet-Albiol, T. A. O'Brien, W. Wernsdorfer, B. Moulton, M. J. Zaworotko, K. A. Abboud and G. Christou, *Angew. Chem., Int. Ed.*, 2005, **44**, 897–901.
57 S. Sanz, J. M. Frost, T. Rajeshkumar, S. J. Dalgarno, G. Rajaraman, W. Wernsdorfer, J. Schnack, P. J. Lusby and E. K. Brechin, *Chem. – Eur. J.*, 2014, **20**, 3010–3013.
58 J. M. Frost, S. Sanz, T. Rajeshkumar, M. B. Pitak, S. J. Coles, G. Rajaraman, W. Wernsdorfer, J. Schnack, P. J. Lusby and E. K. Brechin, *Dalton Trans.*, 2014, **43**, 10690–10694.
59 (*a*) G. Rajaraman, J. Cano, E. K. Brechin and E. J. L. McInnes, *Chem. Commun.*, 2004, 1476–1477; (*b*) G. Rajaraman, E. Ruiz, J. Cano and S. Alvarez, *Chem. Phys. Lett.*, 2005, **415**, 6–9; (*c*) E. Ruiz, A. Rodríguez-Fortea, J. Cano and S. Alvarez, *J. Phys. Chem. Solids*, 2004, **65**, 799–803; (*d*) T. Cauchy, E. Ruiz and S. Alvarez, *J. Am. Chem. Soc.*, 2006, **128**, 15722–15727; (*e*) E. Ruiz, A. Rodríguez-Fortea, J. Tercero, T. Cauchy and C. Massobrio, *J. Chem. Phys.*, 2005, **123**, 074102; (*f*) S. Sasmal, S. Hazra, P. Kundu, S. Dutta, G. Rajaraman, E. C. Sañudo and S. Mohanta, *Inorg. Chem.*, 2011, **50**, 7257–7267.
60 H. L. C. Feltham and S. Brooker, *Coord. Chem. Rev.*, 2014, **276**, 1–33.
61 M. J. Frisch, G. W. Trucks, H. B. Schlegel, G. E. Scuseria, M. A. Robb, J. R. Cheeseman, G. Scalmani, V. Barone, B. Mennucci, G. A. Petersson, H. Nakatsuji, M. Caricato, X. Li, H. P. Hratchian, A. F. Izmaylov, J. Bloino, G. Zheng, J. L. Sonnenberg, M. Hada, M. Ehara, K. Toyota, R. Fukuda, J. Hasegawa, M. Ishida, T. Nakajima, Y. Honda, O. Kitao, H. Nakai, T. Vreven, J. A. Montgomery, Jr., J. E. Peralta, F. Ogliaro, M. Bearpark, J. J. Heyd, E. Brothers, K. N. Kudin, V. N. Staroverov, R. Kobayashi, J. Normand, K. Raghavachari, A. Rendell, J. C. Burant, S. S. Iyengar, J. Tomasi, M. Cossi, N. Rega, J. M. Millam, M. Klene, J. E. Knox, J. B. Cross, V. Bakken, C. Adamo, J. Jaramillo, R. Gomperts, R. E. Stratmann, O. Yazyev, A. J. Austin, R. Cammi, C. Pomelli, J. W. Ochterski, R. L. Martin, K. Morokuma, V. G. Zakrzewski, G. A. Voth, P. Salvador, J. J. Dannenberg, S. Dapprich, A. D. Daniels, Ö. Farkas, J. B. Foresman, J. V. Ortiz, J. Cioslowski and D. J. Fox, *R. D. Gaussian 09*, Gaussian, Inc., Wallingford, CT, 2009.
62 I. Rudra, C. Raghu and S. Ramasesha, *Phys. Rev. B: Condens. Matter Mater. Phys.*, 2002, **65**, 22411–22419.
63 J. Paulovic, F. Cimpoesu, M. Ferbinteanu and K. Hirao, *J. Am. Chem. Soc.*, 2004, **126**, 3321–3331and references therein.
64 J.-P. Costes, F. Dahan and A. Dupuis, *Inorg. Chem.*, 2000, **39**, 5994–6000.
65 (*a*) L. Rosado Piquer and E. C. Sanudo, *Dalton Trans.*, 2015, **44**, 8771–8780; (*b*) C. Benelli, A. Caneschi, D. Gatteschi, O. Guillou and L. Pardi, *Inorg. Chem.*, 1990, **29**, 1750–1755; (*c*) J. B. Goodenough, *Magnetism and the Chemical Bond*, Interscience-Wiley, New York, 1963.
66 J. Cirera and E. Ruiz, *C. R. Chim.*, 2008, **11**, 1227–1234and references therein.
67 G. Rajaraman, F. Totti, A. Bencini, A. Caneschi, R. Sessoli and D. Gatteschi, *Dalton Trans.*, 2009, 3153–3161, and references therein.
68 E. Cremades, S. Gomez-Coca, D. Aravena, S. Alvarez and E. Ruiz, *J. Am. Chem. Soc.*, 2012, **134**, 10532–10542, and references therein.
69 P. De Loth, P. Cassoux, J. P. Daudey and J. P. Malrieu, *J. Am. Chem. Soc.*, 1981, **103**, 4007–4016.
70 S. K. Singh, T. Rajeshkumar, V. Chandrasekhar and G. Rajaraman, *Polyhedron*, 2013, **66**, 81–86, and references therein.
71 S. K. Singh, N. K. Tibrewal and G. Rajaraman, *Dalton Trans.*, 2011, **40**, 10897–10906, and references therein.
72 S. K. Singh and G. Rajaraman, *Dalton Trans.*, 2013, **42**, 3623–3630, and references therein.
73 S. K. Singh, K. S. Pedersen, M. Sigrist, C. A. Thuesen, M. Schau-Magnussen, H. Mutka, S. Piligkos, H. Weihe, G. Rajaraman and J. Bendix, *Chem. Commun.*, 2013, **49**, 5583–5585, and references therein.
74 K. S. Pedersen, G. Lorusso, J. J. Morales, T. Weyhermüller, S. Piligkos, S. K. Singh, D. Larsen, M. Schau-Magnussen, G. Rajaraman, M. Evangelisti and J. Bendix, *Angew. Chem., Int. Ed.*, 2014, **53**, 2394–2397.
75 J.-L. Liu, W.-Q. Lin, Y.-C. Chen, S. Gómez-Coca, D. Aravena, E. Ruiz, J.-D. Leng and M.-L. Tong, *Chem. – Eur. J.*, 2013, **19**, 17567–17577, and references therein.
76 E. Colacio, J. Ruiz, A. J. Mota, M. A. Palacios, E. Cremades, E. Ruiz, F. J. White and E. K. Brechin, *Inorg. Chem.*, 2012, **51**, 5857–5868, and references therein.
77 J.-P. Costes, F. Dahan, C. Duhayon and A. J. Mota, *Polyhedron*, 2015, **96**, 51–56, and references therein.
78 S. K. Singh, M. F. Beg and G. Rajaraman, *Chem. – Eur. J.*, 2016, **22**, 672–680.
79 J.-P. Costes, M. Auchel, F. o. Dahan, V. Peyrou, S. Shova and W. Wernsdorfer, *Inorg. Chem.*, 2006, **45**, 1924–1934.
80 (*a*) R. Gheorghe, P. Cucos, M. Andruh, J.-P. Costes, B. Donnadieu and S. Shova, *Chem. – Eur. J.*, 2006, **12**, 187–203; (*b*) H.-Z. Kou, B. C. Zhou and R.-J. Wang, *Inorg. Chem.*, 2003, **42**, 7658–7665.
81 A. Hosoi, Y. Yukawa, S. Igarashi, S. J. Teat, O. Roubeau, M. Evangelisti, E. Cremades, E. Ruiz, L. A. Barrios and G. Aromí, *Chem. – Eur. J.*, 2011, **17**, 8264–8268.
82 T. Rajeshkumar, H. V. Annadata, M. Evangelisti, S. K. Langley, N. F. Chilton, K. S. Murray and G. Rajaraman, *Inorg. Chem.*, 2015, **54**, 1661–1670.
83 S. K. Gupta, A. A. Dar, T. Rajeshkumar, S. Kuppuswamy, S. K. Langley, K. S. Murray, G. Rajaraman and R. Murugavel, *Dalton Trans.*, 2015, **44**, 5961–5965.
84 T. Rajeshkumar, S. K. Singh and G. Rajaraman, *Polyhedron*, 2013, **52**, 1299–1305.
85 L. E. Roy and T. Hughbanks, *J. Am. Chem. Soc.*, 2006, **128**, 568–575.
86 L. E. Sweet, L. E. Roy, F. Meng and T. Hughbanks, *J. Am. Chem. Soc.*, 2006, **128**, 10193–10201.
87 (*a*) J. D. Rinehart, M. Fang, W. J. Evans and J. R. Long, *J. Am. Chem. Soc.*, 2011, **133**, 14236–14239; (*b*) J. D. Rinehart, M. Fang, W. J. Evans and J. R. Long, *Nat. Chem.*, 2011, **3**, 538–542.
88 J. Ren, B. Wang and Z. Chen, *Sci. China, Ser. B: Chem.*, 2009, **52**, 1961–1968.
89 T. Rajeshkumar and G. Rajaraman, *Chem. Commun.*, 2012, **48**, 7856–7858.

90 K. R. Meihaus, J. F. Corbey, M. Fang, J. W. Ziller, J. R. Long and W. J. Evans, *Inorg. Chem.*, 2014, **53**, 3099–3107.
91 C. Benelli, A. Caneschi, D. Gatteschi and R. Sessoli, *Inorg. Chem.*, 1993, **32**, 4797–4801.
92 T. Gupta, T. Rajeshkumar and G. Rajaraman, *Phys. Chem. Chem. Phys.*, 2014, **16**, 14568–14577.
93 M. K. Singh, N. Yadav and G. Rajaraman, *Chem. Commun.*, 2015, **51**, 17732–17735.
94 B. Bechlars, D. M. D'Alessandro, D. M. Jenkins, A. T. Iavarone, S. D. Glover, C. P. Kubiak and J. R. Long, *Nat. Chem.*, 2010, **2**, 362–368.
95 (*a*) V. Barone, A. Bencini, I. Ciofini, C. A. Daul and F. Totti, *J. Am. Chem. Soc.*, 1998, **120**, 8357–8365; (*b*) V. Barone, A. Bencini, D. Gatteschi and F. Totti, *Chem. – Eur. J.*, 2002, **8**, 5019–5027.
96 A. Bencini, D. Gatteschi, M. Mattesini, F. Totti and I. Ciofini, *Mol. Cryst. Liq. Cryst. Sci. Technol., Sect. A*, 1999, **335**, 665–674.
97 C. Bosch-Serrano, J. M. Clemente-Juan, E. Coronado, A. Gaita-Ariño, A. Palii and B. Tsukerblat, *Phys. Rev. B: Condens. Matter Mater. Phys.*, 2012, **86**, 024432.
98 S. Ghosh, S. K. Singh, S. Tewary and G. Rajaraman, *Dalton Trans.*, 2013, **42**, 16490–16493.
99 C. Bosch-Serrano, J. M. Clemente-Juan, E. Coronado, A. Gaita-Ariño, A. Palii and B. Tsukerblat, *ChemPhysChem*, 2012, **13**, 2662–2665.
100 S. Sharma, K. Sivalingam, F. Neese and K.-L. ChanGarnet, *Nat. Chem.*, 2014, **6**, 927–933.
101 S. Piligkos, E. Bill, D. Collison, E. J. L. McInnes, G. A. Timco, H. Weihe, R. E. P. Winpenny and F. Neese, *J. Am. Chem. Soc.*, 2007, **129**, 760–761.
102 A. Palii, B. Tsukerblat, J. M. Clemente-Juan and E. Coronado, *Int. Rev. Phys. Chem.*, 2010, **29**, 135–230.
103 A. E. Berkowitz and K. Takano, *J. Magn. Magn. Mater.*, 1999, **200**, 552–570.
104 V. S. Mironov, L. F. Chibotaru and A. Ceulemans, *J. Am. Chem. Soc.*, 2003, **125**, 9750–9760.
105 M. Atanasov, P. Comba and C. A. Daul, *J. Phys. Chem. A*, 2006, **110**, 13332–13340.
106 (*a*) P. W. Anderson, *Phys. Rev.*, 1959, **115**, 2–13; (*b*) T. Moriya, *Phys. Rev.*, 1960, **120**, 91–98.
107 (*a*) V. S. Mironov, *Inorg. Chem.*, 2015, **54**, 11339–11355; (*b*) V. S. Mironov, L. F. Chibotaru and A. Ceulemans, *Phys. Rev. B: Condens. Matter Mater. Phys.*, 2003, **67**, 014424.
108 M. Atanasov, P. Comba and C. A. Daul, *Inorg. Chem.*, 2008, **47**, 2449–2463.
109 S. K. Singh and G. Rajaraman, *Chem. – Eur. J.*, 2014, **20**, 113–123.
110 J. Dreiser, K. S. Pedersen, A. Schnegg, K. Holldack, J. Nehrkorn, M. Sigrist, P. Tregenna-Piggott, H. Mutka, H. Weihe, V. S. Mironov, J. Bendix and O. Waldmann, *Chem. – Eur. J.*, 2013, **19**, 3693–3701.
111 K. S. Pedersen, M. Schau-Magnussen, J. Bendix, H. Weihe, A. V. Palii, S. I. Klokishner, S. Ostrovsky, O. S. Reu, H. Mutka and P. L. W. Tregenna-Piggott, *Chem. – Eur. J.*, 2010, **16**, 13458–13464.
112 U. J. Williams, B. D. Mahoney, P. T. DeGregorio, P. J. Carroll, E. Nakamaru-Ogiso, J. M. Kikkawa and E. J. Schelter, *Chem. Commun.*, 2012, **48**, 5593–5595.
113 E. Ruiz, J. Cirera, J. Cano, S. Alvarez, C. Loose and J. Kortus, *Chem. Commun.*, 2008, 52–54.
114 (*a*) F. Neese, in *In the Quantum Chemical Calculation of NMR and EPR Properties*, ed. M. B. M. Kaupp and V. Malkin, Wiley-VCH, Heidelberg, 2004, p. 541; (*b*) J. E. Harriman, *Theoretical Foundations of Electron Spin Resonance*, Academic Press, New York, 1978; (*c*) F. Neese, *J. Am. Chem. Soc.*, 2006, **128**, 10213–10222.
115 R. McWeeny and Y. Mizuno, *Proc. R. Soc. London, Ser. A*, 1961, **259**, 554–577.
116 J. S. Griffith, *Cambridge University Press*, Cambridge, 1964.
117 A. J. Schweiger and G. Jeschke, *Principle of Pulse Electron Paramagnetic Resonance*, Oxford University Press, Oxford, UK, 2001, p. 32.
118 S. Gomez-Coca, E. Cremades, N. Aliaga-Alcalde and E. Ruiz, *J. Am. Chem. Soc.*, 2013, **135**, 7010–7018.
119 F. Neese, *J. Inorg. Biochem.*, 2006, **100**, 716–726.
120 S. Zein, C. Duboc, W. Lubitz and F. Neese, *Inorg. Chem.*, 2008, **47**, 134–142.
121 (*a*) F. Neese, *Wiley Interdiscip. Rev.: Comput. Mol. Sci.*, 2012, **2**, 73–78; (*b*) D. A. Pantazis and F. Neese, *J. Chem. Theory Comput.*, 2009, **5**, 2229–2238.
122 F. Neese, *Coord. Chem. Rev.*, 2009, **253**, 526–563.
123 (*a*) K. E. R. Marriott, L. Bhaskaran, C. Wilson, M. Medarde, S. T. Ochsenbein, S. Hill and M. Murrie, *Chem. Sci.*, 2015, **6**, 6823–6828; (*b*) S. Gómez-Coca, E. Cremades, N. Aliaga-Alcalde and E. Ruiz, *Inorg. Chem.*, 2014, **53**, 676–678.
124 R. Ruamps, R. Maurice, L. Batchelor, M. Boggio-Pasqua, R. Guillot, A. L. Barra, J. Liu, E.-E. Bendeif, S. Pillet, S. Hill, T. Mallah and N. Guihéry, *J. Am. Chem. Soc.*, 2013, **135**, 3017–3026.
125 G. Rogez, J.-N. Rebilly, A.-L. Barra, L. Sorace, G. Blondin, N. Kirchner, M. Duran, J. van Slageren, S. Parsons, L. Ricard, A. Marvilliers and T. Mallah, *Angew. Chem., Int. Ed.*, 2005, **44**, 1876–1879.
126 R. Ruamps, L. J. Batchelor, R. Maurice, N. Gogoi, P. Jiménez-Lozano, N. Guihéry, C. de Graaf, A.-L. Barra, J.-P. Sutter and T. Mallah, *Chem. – Eur. J.*, 2013, **19**, 950–956.
127 M. Gruden-Pavlovic, M. Peric, M. Zlatar and P. Garcia-Fernandez, *Chem. Sci.*, 2014, **5**, 1453–1462.
128 S. K. Singh, T. Gupta, P. Badkur and G. Rajaraman, *Chem. – Eur. J.*, 2014, **20**, 10305–10313.
129 R. Maurice, R. Bastardis, C. d. Graaf, N. Suaud, T. Mallah and N. Guihéry, *J. Chem. Theory Comput.*, 2009, **5**, 2977–2984.
130 S. F. Ye and F. Neese, *J. Chem. Theory Comput.*, 2012, **8**, 2344–2351.
131 J.-P. Costes, R. Maurice and L. Vendier, *Chem. – Eur. J.*, 2012, **18**, 4031–4040.
132 D. Schweinfurth, J. Krzystek, I. Schapiro, S. Demeshko, J. Klein, J. Telser, A. Ozarowski, C.-Y. Su, F. Meyer, M. Atanasov, F. Neese and B. Sarkar, *Inorg. Chem.*, 2013, **52**, 6880–6892.
133 A. Kubica, J. Kowalewski, D. Kruk and M. Odelius, *J. Chem. Phys.*, 2013, **138**, 064304.
134 R. Ruamps, R. Maurice, C. de Graaf and N. Guihéry, *Inorg. Chem.*, 2014, **53**, 4508–4516.
135 I. Nemec, R. Herchel, I. Svoboda, R. Boca and Z. Travnicek, *Dalton Trans.*, 2015, **44**, 9551–9560.
136 S.-D. Jiang, D. Maganas, N. Levesanos, E. Ferentinos, S. Haas, K. Thirunavukkuarasu, J. Krzystek, M. Dressel, L. Bogani, F. Neese and P. Kyritsis, *J. Am. Chem. Soc.*, 2015, **137**, 12923–12928.
137 M. Murrie, *Chem. Soc. Rev.*, 2010, **39**, 1986–1995.
138 J. Krzystek, A. Ozarowski, S. A. Zvyagin and J. Telser, *Inorg. Chem.*, 2012, **51**, 4954–4964.
139 (*a*) R. Herchel, L. Váhovská, I. Potočňák and Z. Trávníček, *Inorg. Chem.*, 2014, **53**, 5896–5898; (*b*) M. Sundararajan, D. Ganyushin, S. Ye and F. Neese, *Dalton Trans.*, 2009, 6021–6036.
140 A. Buchholz, A. O. Eseola and W. Plass, *C. R. Chim.*, 2012, **15**, 929–936.
141 M. A. García-Monforte, I. Ara, A. Martín, B. Menjón, M. Tomás, P. J. Alonso, A. B. Arauzo, J. I. Martínez and C. Rillo, *Inorg. Chem.*, 2014, **53**, 12384–12395.
142 (*a*) P. J. Van der Put and A. A. Schilperoord, *Inorg. Chem.*, 1974, **13**, 2476–2481; (*b*) P. J. M. W. L. Birker, J. J. Bour and J. J. Steggerda, *Inorg. Chem.*, 1973, **12**, 1254–1259; (*c*) C.-H. Cho, T.-Y. Chien, J.-H. Chen, S.-S. Wang and J.-Y. Tung, *Dalton Trans.*, 2010, **39**, 2609–2614.
143 M. Idešicová, J. Titiš, J. Krzystek and R. Boča, *Inorg. Chem.*, 2013, **52**, 9409–9417.
144 D. Maganas, S. Sottini, P. Kyritsis, E. J. J. Groenen and F. Neese, *Inorg. Chem.*, 2011, **50**, 8741–8754.
145 D. Brazzolotto, M. Gennari, S. Yu, J. Pécaut, M. Rouzières, R. Clérac, M. Orio and C. Duboc, *Chem. – Eur. J.*, 2016, **22**, 925–933.
146 S. Vaidya, A. Upadhyay, S. K. Singh, T. Gupta, S. Tewary, S. K. Langley, J. P. S. Walsh, K. S. Murray, G. Rajaraman and M. Shanmugam, *Chem. Commun.*, 2015, **51**, 3739–3742.
147 S. K. Singh and G. Rajaraman, *Chem. – Eur. J.*, 2014, **20**, 5214–5218.
148 L. Chibotaru, A. Ceulemans and H. Bolvin, *Phys. Rev. Lett.*, 2008, **101**, 033003.
149 J. Luzon and R. Sessoli, *Dalton Trans.*, 2012, **41**, 13556–13567.
150 A.-L. Barra, A. Caneschi, A. Cornia, D. Gatteschi, L. Gorini, L.-P. Heiniger, R. Sessoli and L. Sorace, *J. Am. Chem. Soc.*, 2007, **129**, 10754–10762.
151 L. Ungur and L. F. Chibotaru, *Lanthanides and Actinides in Molecular Magnetism*, Wiley-VCH Verlag GmbH & Co. KGaA, 2015, ch. 6, pp. 153–184.
152 N. Ishikawa, *Polyhedron*, 2007, **26**, 2147–2153.
153 S. S.-D. Jiang, B.-W. Wang and S. Gao, *Advances in Lanthanide Single-Ion Magnets*, Springer-Verlag, Berlin, Heidelberg, 2014, ch. 153, pp. 1–31, DOI: 10.1007/430_2014_153.

154 J. J. Baldoví, S. Cardona-Serra, J. M. Clemente-Juan, E. Coronado, A. Gaita-Ariño and A. Palii, *Inorg. Chem.*, 2012, **51**, 12565–12574.
155 J. D. Rinehart and J. R. Long, *Chem. Sci.*, 2011, **2**, 2078–2085.
156 (*a*) P. Zhang, Y. N. Guo and J. K. Tang, *Coord. Chem. Rev.*, 2013, **257**, 1728–1763; (*b*) Y. N. Guo, G. F. Xu, Y. Guo and J. K. Tang, *Dalton Trans.*, 2011, **40**, 9953–9963.
157 D. Aravena and E. Ruiz, *Inorg. Chem.*, 2013, **52**, 13770–13778.
158 N. F. Chilton, D. Collison, E. J. L. McInnes, R. E. P. Winpenny and A. Soncini, *Nat. Commun.*, 2013, **4**, 2551.
159 G. Cucinotta, M. Perfetti, J. Luzon, M. Etienne, P. E. Car, A. Caneschi, G. Calvez, K. Bernot and R. Sessoli, *Angew. Chem., Int. Ed.*, 2012, **51**, 1606–1610.
160 L. Ungur and L. F. Chibotaru, *Phys. Chem. Chem. Phys.*, 2011, **13**, 20086–20090.
161 M. E. Boulon, G. Cucinotta, J. Luzon, C. Degl'Innocenti, M. Perfetti, K. Bernot, G. Calvez, A. Caneschi and R. Sessoli, *Angew. Chem., Int. Ed.*, 2013, **52**, 350–354.
162 S. N. Konig, N. F. Chilton, C. Maichle-Mossmer, E. M. Pineda, T. Pugh, R. Anwander and R. A. Layfield, *Dalton Trans.*, 2014, **43**, 3035–3038.
163 F. Habib, G. Brunet, V. Vieru, I. Korobkov, L. F. Chibotaru and M. Murugesu, *J. Am. Chem. Soc.*, 2013, **135**, 13242–13245.
164 J. Ruiz, A. J. Mota, A. Rodriguez-Dieguez, S. Titos, J. M. Herrera, E. Ruiz, E. Cremades, J. P. Costes and E. Colacio, *Chem. Commun.*, 2012, **48**, 7916–7918.
165 R. Marx, F. Moro, M. Dorfel, L. Ungur, M. Waters, S. D. Jiang, M. Orlita, J. Taylor, W. Frey, L. F. Chibotaru and J. van Slageren, *Chem. Sci.*, 2014, **5**, 3287–3293.
166 L. Ungur, J. J. Le Roy, I. Korobkov, M. Murugesu and L. F. Chibotaru, *Angew. Chem., Int. Ed.*, 2014, **53**, 4413–4417.
167 J. J. Le Roy, M. Jeletic, S. I. Gorelsky, I. Korobkov, L. Ungur, L. F. Chibotaru and M. Murugesu, *J. Am. Chem. Soc.*, 2013, **135**, 3502–3510.
168 E. Lucaccini, L. Sorace, M. Perfetti, J.-P. Costes and R. Sessoli, *Chem. Commun.*, 2014, **50**, 1648–1651.
169 P. A. Malmqvist, B. O. Roos and B. Schimmelpfennig, *Chem. Phys. Lett.*, 2002, **357**, 230–240.
170 N. F. Chilton, C. A. P. Goodwin, D. P. Mills and R. E. P. Winpenny, *Chem. Commun.*, 2015, **51**, 101–103.
171 (*a*) D. A. Garanin and E. M. Chudnovsky, *Phys. Rev. B: Condens. Matter Mater. Phys.*, 1997, **56**, 11102–11118; (*b*) M. N. Leuenberger and D. Loss, *Phys. Rev. B: Condens. Matter Mater. Phys.*, 2000, **61**, 1286–1302.
172 V. E. Campbell, H. Bolvin, E. Rivière, R. Guillot, W. Wernsdorfer and T. Mallah, *Inorg. Chem.*, 2014, **53**, 2598–2605.
173 T. Pugh, F. Tuna, L. Ungur, D. Collison, E. J. L. McInnes, L. F. Chibotaru and R. A. Layfield, *Nat. Commun.*, 2015, **6**, 7492.
174 E. L. Gavey, M. Al Hareri, J. Regier, L. D. Carlos, R. A. S. Ferreira, F. S. Razavi, J. M. Rawson and M. Pilkington, *J. Mater. Chem. C*, 2015, **3**, 7738–7747.
175 M. Gregson, N. F. Chilton, A.-M. Ariciu, F. Tuna, I. F. Crowe, W. Lewis, A. J. Blake, D. Collison, E. J. L. McInnes, R. E. P. Winpenny and S. T. Liddle, *Chem. Sci.*, 2016, **7**, 155–165.
176 T. Gupta and G. Rajaraman, *J. Chem. Sci.*, 2014, **126**, 1569–1579.
177 G. Rajaraman, S. K. Singh, T. Gupta and M. Shanmugam, *Chem. Commun.*, 2014, **50**, 15513–15516.
178 K. Qian, J. J. Baldovi, S.-D. Jiang, A. Gaita-Arino, Y.-Q. Zhang, J. Overgaard, B.-W. Wang, E. Coronado and S. Gao, *Chem. Sci.*, 2015, **6**, 4587–4593.
179 A. Upadhyay, S. K. Singh, C. Das, R. Mondol, S. K. Langley, K. S. Murray, G. Rajaraman and M. Shanmugam, *Chem. Commun.*, 2014, **50**, 8838–8841.
180 I. Oyarzabal, J. Ruiz, J. M. Seco, M. Evangelisti, A. Camón, E. Ruiz, D. Aravena and E. Colacio, *Chem. – Eur. J.*, 2014, **20**, 14262–14269.
181 S. Das, K. S. Bejoymohandas, A. Dey, S. Biswas, M. L. P. Reddy, R. Morales, E. Ruiz, S. Titos-Padilla, E. Colacio and V. Chandrasekhar, *Chem. – Eur. J.*, 2015, **21**, 6449–6464.
182 I. Oyarzabal, J. Ruiz, E. Ruiz, D. Aravena, J. M. Seco and E. Colacio, *Chem. Commun.*, 2015, **51**, 12353–12356.
183 J. P. Costes, S. Titos-Padilla, I. Oyarzabal, T. Gupta, C. Duhayon, G. Rajaraman and E. Colacio, *Chem. – Eur. J.*, 2015, **21**, 15785–15796.
184 N. F. Chilton, S. K. Langley, B. Moubaraki, A. Soncini, S. R. Batten and K. S. Murray, *Chem. Sci.*, 2013, **4**, 1719–1730.
185 K. S. Pedersen, L. Ungur, M. Sigrist, A. Sundt, M. Schau-Magnussen, V. Vieru, H. Mutka, S. Rols, H. Weihe, O. Waldmann, L. F. Chibotaru, J. Bendix and J. Dreiser, *Chem. Sci.*, 2014, **5**, 1650–1660.
186 S. K. Singh, T. Gupta and G. Rajaraman, *Inorg. Chem.*, 2014, **53**, 10835–10845.
187 C. Das, A. Upadhyay, S. Vaidya, S. K. Singh, G. Rajaraman and M. Shanmugam, *Chem. Commun.*, 2015, **51**, 6137–6140.
188 D. Maganas, J. Krzystek, E. Ferentinos, A. M. Whyte, N. Robertson, V. Psycharis, A. Terzis, F. Neese and P. Kyritsis, *Inorg. Chem.*, 2012, **51**, 7218–7231.
189 M. Idešicová, J. Titiš, J. Krzystek and R. Boča, *Inorg. Chem.*, 2013, **52**, 9409–9417.
190 M. Atanasov, P. Comba, S. Helmle, D. Muller and F. Neese, *Inorg. Chem.*, 2012, **51**, 12324–12335.
191 (*a*) J. M. Ricart, R. Dovesi, C. Roetti and V. R. Saunders, *Phys. Rev. B: Condens. Matter Mater. Phys.*, 1995, **52**, 2381–2389; (*b*) I. de P. R. Moreira and F. Illas, *Phys. Rev. B: Condens. Matter Mater. Phys.*, 1997, **55**, 4129–4137; (*c*) I. de P. R. Moreira, R. Dovesi, C. Roetti, V. R. Saunders and R. Orlando, *Phys. Rev. B: Condens. Matter Mater. Phys.*, 2000, **62**, 7816–7823; (*d*) I. d. P. R. Moreira and F. Illas, *Phys. Chem. Chem. Phys.*, 2006, **8**, 1645–1659; (*e*) M.-H. Whangbo, H.-J. Koo and D. Dai, *J. Solid State Chem.*, 2003, **176**, 417–481.
192 (*a*) R. Boča, *Coord. Chem. Rev.*, 2004, **248**, 757–815; (*b*) R. Maurice, C. de Graaf and N. Guihéry, *Phys. Rev. B: Condens. Matter Mater. Phys.*, 2010, **81**, 214427.
193 (*a*) M. Verdaguer and L. Jean-Pierre, *Electrons in Molecules: from Basic Principles to Molecular Electronics*, Oxford University Press, 2013; (*b*) M. Julve, M. Verdaguer, A. Gleizes, M. Philoche-Levisalles and O. Kahn, *Inorg. Chem.*, 1984, **23**, 3808–3818.
194 (*a*) D. I. Khomskii, *Basic Aspects of the Quantum Theory of Soilds (Order and eelmentary Excitations)*, Cambridge University Press, The Edinburgh Building, Cambridge, UK, 2010; (*b*) D. I. Khomskii and M. V. Mostovoy, *J. Phys. A: Math. Gen.*, 2003, **36**, 9197–9207; (*c*) W. Geertsma and D. Khomskii, *Phys. Rev. B: Condens. Matter Mater. Phys.*, 1996, **54**, 3011–3014.
195 (*a*) J. B. Goodenough, *Phys. Rev.*, 1955, **100**, 564–573; (*b*) J. B. Goodenough, in *Magnetism and Chemical Bond*, ed. F. A. Cotton, Cambridge, Massachusetts, Interscience Publishers a division of John Wiley & Sons, New York -London, New York, 1963; (*c*) J. Kanamori, *J. Phys. Chem. Solids*, 1959, **10**, 87–98; (*d*) P. W. Anderson, *Phys. Rev.*, 1950, **79**, 350–356; (*e*) P. W. Anderson, *Phys. Rev.*, 1959, **115**, 2–13.
196 (*a*) V. Papaefthymiou, J.-J. Girerd, I. Moura, J. J. G. Moura and E. Münck, *J. Am. Chem. Soc.*, 1987, **109**, 4703–4710; (*b*) G. Blondin and J.-J. Girerd, *Chem. Rev.*, 1990, **90**, 1359–1376; (*c*) E. L. Bominaar, Z. Hu, E. Münck, J.-J. Girerd and S. A. Borshch, *J. Am. Chem. Soc.*, 1995, **117**, 6976–6989; (*d*) J.-J. Girerd, V. Papaefthymiou, K. K. Surerus and E. Münck, *Pure Appl. Chem.*, 1989, **61**, 805–816; (*e*) E. Münck, V. Papaefthymiou, K. K. Surerus and J.-J. Girerd, Metal Clusters in Proteins, ed. L. Que, 1988, ACS Symposium Series No. 372.
197 C. Zener, *Phys. Rev.*, 1951, **82**, 403–405.
198 (*a*) N. Guihéry and J. P. Malrieu, *J. Chem. Phys.*, 2003, **119**, 8956–8965; (*b*) D. Taratiel and N. Guihéry, *J. Chem. Phys.*, 2004, **121**, 7127–7135.
199 (*a*) C. Boilleau, N. Suaud, R. Bastardis, N. Guihéry and J. P. Malrieu, *Theor. Chem. Acc.*, 2009, **126**, 231–241; (*b*) J. P. Malrieu, R. Caballol, C. J. Calzado, C. de Graaf and N. Guihéry, *Chem. Rev.*, 2014, **114**, 429–492.
200 (*a*) X. Wang and A. J. Freeman, *J. Magn. Magn. Mater.*, 1997, **171**, 103–105; (*b*) H. Yi, N. H. Hur and J. Yu, *Phys. Rev. B: Condens. Matter Mater. Phys.*, 2000, **61**, 9501–9505; (*c*) N. F. Mott, *Metal-Insulator Transitions*, Taylor & Francis, London, 1990.
201 (*a*) S. B. Piepho, E. R. Krausz and P. N. Schatz, *J. Am. Chem. Soc.*, 1978, **100**, 2996–3005; (*b*) I. B. Bersuker, S. A. Borshch and L. F. Chibotaru, *Chem. Phys.*, 1989, **136**, 379–384; (*c*) A. Palii, B. Tsukerblat, J. M. Clemente-Juan and S. M. Aldoshin, *J. Phys. Chem. A*, 2015, **119**, 9844–9856, and references therein.
202 R. C. Powell, *Physics of Solid-State Laser Materials*, Springer -Verlag New York, Inc., Tucson, USA, 1998, p. 170.
203 (*a*) Y. Rechkemmer, F. D. Breitgoff, M. van der Meer, M. Atanasov, M. Hakl, M. Orlita, P. Neugebauer, F. Neese, B. Sarkar and J. van Slageren, *Nat. Commun.*, 2016, **7**, 10467; (*b*) M. R. Saber and K. R. Dunbar, *Chem. Commun.*, 2014, **50**, 12266–12269.
204 D. Pinkowicz, H. I. Southerland, C. Avendaño, A. Prosvirin, C. Sanders, W. Wernsdorfer, K. S. Pedersen, J. Dreiser, R. Clérac, J. Nehrkorn, G. G. Simeoni, A. Schnegg, K. Holldack and K. R. Dunbar, *J. Am. Chem. Soc.*, 2015, **137**, 14406–14422.

205 L. F. Chibotaru and L. Ungur, *J. Chem. Phys.*, 2012, **137**, 064112.
206 (*a*) K. W. H. Stevens, *Proc. Phys. Soc., London, Sect. A*, 1952, **65**, 209; (*b*) J. J. Baldovi, J. J. Borras-Almenar, J. M. Clemente-Juan, E. Coronado and A. Gaita-Arino, *Dalton Trans.*, 2012, **41**, 13705–13710; (*c*) J. J. Baldoví, S. Cardona-Serra, J. M. Clemente-Juan, E. Coronado, A. Gaita-Ariño and A. Palii, *J. Comput. Chem.*, 2013, **34**, 1961–1967.
207 J.-P. Costes, C. Duhayon, S. Mallet-Ladeira, S. Shova and L. Vendier, *Chem. – Eur. J.*, 2016, **22**, 2171–2180.
208 (*a*) E. Colacio, J. Ruiz, E. Ruiz, E. Cremades, J. Krzystek, S. Carretta, J. Cano, T. Guidi, W. Wernsdorfer and E. K. Brechin, *Angew. Chem., Int. Ed.*, 2013, **52**, 9130–9134; (*b*) S. Gómez-Coca, A. Urtizberea, E. Cremades, P. J. Alonso, A. Camón, E. Ruiz and F. Luis, *Nat. Commun.*, 2014, **5**, 4300.
209 (*a*) V. S. Mironov, *Inorg. Chem.*, 2015, **54**, 11339–11355; (*b*) L. Rosado Piquer and E. C. Sanudo, *Dalton Trans.*, 2015, **44**, 8771–8780.
210 (*a*) J.-P. Costes, F. Dahan, A. Dupuis and J.-P. Laurent, *Inorg. Chem.*, 1996, **35**, 2400–2402; (*b*) O. Margeat, P. G. Lacroix, J. P. Costes, B. Donnadieu, C. Lepetit and K. Nakatani, *Inorg. Chem.*, 2004, **43**, 4743–4750; (*c*) S. Gao, O. Borgmeier and H. Lueken, *Acta Phys. Polym.*, 1990, **A90**, 393–398; (*d*) M. Sasaki, H. Horiuchi, M. Kumagai, M. Sakamoto, H. Sakiyama, Y. Nishida, Y. Sadaoka, M. Ohba and H. Okawa, *Chem. Lett.*, 1998, 911–912; (*e*) J.-P. Costes, F. Dahan and A. Dupuis, *Inorg. Chem.*, 2000, **39**, 165–168; (*f*) J.-P. Costes, F. Dahan, A. Dupuis and J. P. Laurent, *Inorg. Chem.*, 1997, **36**, 4284–4286; (*g*) T. Yamaguchi, Y. Sunatsuki, M. Kojima, H. Akashi, M. Tsuchimoto, N. Re, S. Osa and N. Matsumoto, *Chem. Commun.*, 2004, 1048–1049; (*h*) J.-P. Costes, T. Yamaguchi, M. Kojima and L. Vendier, *Inorg. Chem.*, 2009, **48**, 5555–5561; (*i*) J.-P. Costes, F. Dahan, B. Donnadieu, J. Garcia-Tojal and J.-P. Laurent, *Eur. J. Inorg. Chem.*, 2001, 363–365; (*j*) J.-P. Costes, S. Shova, J. Modesto, C. Juan and N. Suet, *Dalton Trans.*, 2005, 2830–2832.
211 (*a*) S. K. Gupta, T. Rajeshkumar, G. Rajaraman and R. Murugavel, *Chem. Sci.*, 2016, DOI: 10.1039/C6SC00279J; (*b*) S. D. Jiang, B. W. Wang, H. L. Sun, Z. M. Wang and S. Gao, *J. Am. Chem. Soc.*, 2011, **133**, 4730–4733; (*c*) J. J. Le Roy, I. Korobkov and M. Murugesu, *Chem. Commun.*, 2014, **50**, 1602–1604; (*d*) P. Zhang, L. Zhang, C. Wang, S. Xue, S.-Y. Lin and J. Tang, *J. Am. Chem. Soc.*, 2014, **136**, 4484–4487; (*e*) K. R. Meihaus and J. R. Long, *J. Am. Chem. Soc.*, 2013, **135**, 17952–17957; (*f*) A. J. Brown, D. Pinkowicz, M. R. Saber and K. R. Dunbar, *Angew. Chem., Int. Ed.*, 2015, **54**, 5864–5868; (*g*) F. Branzoli, P. Carretta, M. Filibian, G. Zoppellaro, M. J. Graf, J. R. Galan-Mascaros, O. Fuhr, S. Brink and M. Ruben, *J. Am. Chem. Soc.*, 2009, **131**, 4387–4396; (*h*) M. Gonidec, D. B. Amabilino and J. Veciana, *Dalton Trans.*, 2012, **41**, 13632–13639; (*i*) N. Ishikawa, M. Sugita, N. Tanaka, T. Ishikawa, S.-y. Koshihara and Y. Kaizu, *Inorg. Chem.*, 2004, **43**, 5498–5500; (*j*) S. Takamatsu, T. Ishikawa, S. Y. Koshihara and N. Ishikawa, *Inorg. Chem.*, 2007, **46**, 7250–7252; (*k*) M. Gonidec, F. Luis, A. Vilchez, J. Esquena, D. B. Amabilino and J. Veciana, *Angew. Chem., Int. Ed.*, 2010, **49**, 1623–1626; (*l*) C. R. Ganivet, B. Ballesteros, G. de la Torre, J. M. Clemente-Juan, E. Coronado and T. Torres, *Chem. – Eur. J.*, 2013, **19**, 1457–1465; (*m*) R. J. Blagg, L. Ungur, F. Tuna, J. Speak, P. Comar, D. Collison, W. Wernsdorfer, E. J. L. McInnes, L. F. Chibotaru and R. E. P. Winpenny, *Nat. Chem.*, 2013, **5**, 673–678; (*n*) R. J. Blagg, C. A. Muryn, E. J. L. McInnes, F. Tuna and R. E. P. Winpenny, *Angew. Chem., Int. Ed.*, 2011, **50**, 6530–6533; (*o*) S. Demir, J. M. Zadrozny, M. Nippe and J. R. Long, *J. Am. Chem. Soc.*, 2012, **134**, 18546–18549; (*p*) X. Yi, K. Bernot, F. Pointillart, G. Poneti, G. Calvez, C. Daiguebonne, O. Guillou and R. Sessoli, *Chem. – Eur. J.*, 2012, **18**, 11379–11387; (*q*) F. Tuna, C. A. Smith, M. Bodensteiner, L. Ungur, L. F. Chibotaru, E. J. L. McInnes, R. E. P. Winpenny, D. Collison and R. A. Layfield, *Angew. Chem., Int. Ed.*, 2012, **51**, 6976–6980; (*r*) J. J. Le Roy, L. Ungur, I. Korobkov, L. F. Chibotaru and M. Murugesu, *J. Am. Chem. Soc.*, 2014, **136**, 8003–8010; (*s*) W.-B. Sun, P.-F. Yan, S.-D. Jiang, B.-W. Wang, Y.-Q. Zhang, H.-F. Li, P. Chen, Z.-M. Wang and S. Gao, *Chem. Sci.*, 2016, **7**, 684–691; (*t*) J.-L. Liu, J.-Y. Wu, Y.-C. Chen, V. Mereacre, A. K. Powell, L. Ungur, L. F. Chibotaru, X.-M. Chen and M.-L. Tong, *Angew. Chem., Int. Ed.*, 2014, **53**, 12966–12970; (*u*) J.-L. Liu, Y.-C. Chen, Y.-Z. Zheng, W.-Q. Lin, L. Ungur, W. Wernsdorfer, L. F. Chibotaru and M.-L. Tong, *Chem. Sci.*, 2013, **4**, 3310–3316; (*v*) J.-L. Liu, J.-Y. Wu, G.-Z. Huang, Y.-C. Chen, J.-H. Jia, L. Ungur, L. F. Chibotaru, X.-M. Chen and M.-L. Tong, *Sci. Rep.*, 2015, **5**, 16621–16629; (*w*) Y.-C. Chen, J.-L. Liu, L. Ungur, J. Liu, Q.-W. Li, L.-F. Wang, Z.-P. Ni, L. F. Chibotaru, X.-M. Chen and M.-L. Tong, *J. Am. Chem. Soc.*, 2016, **138**, 2829–2837; (*x*) J. Liu, Y.-C. Chen, J.-L. Liu, V. Vieru, L. Ungur, J.-H. Jia, L. F. Chibotaru, Y. Lan, W. Wernsdorfer, S. Gao, X.-M. Chen and M.-L. Tong, *J. Am. Chem. Soc.*, 2016, **138**, 5441–5450.
212 N. Iwahara and L. F. Chibotaru, *Sci. Rep.*, 2016, **6**, 24743.
213 G. V. Chilkuri, N. Suaud and N. Guihéry, *Crystals*, 2016, **6**, 39–53.
214 P. ter Heerdt, M. Stefan, E. Goovaerts, A. Caneschi and A. Cornia, *J. Magn. Reson.*, 2006, **179**, 29–37.
215 S. K. Gupta, T. Rajeshkumar, G. Rajaraman and R. Murugavel, *Chem. Commun.*, 2016, **52**, 7168–7171.
216 M. Retegan, M.-N. Collomb, F. Neese and C. Duboc, *Phys. Chem. Chem. Phys.*, 2013, **15**, 223–234.

